INFORMATION TO USERS

This manuscript has been reproduced from the microfilm master. UMI films the text directly from the original or copy submitted. Thus, some thesis and dissertation copies are in typewriter face, while others may be from any type of computer printer.

The quality of this reproduction is dependent upon the quality of the copy submitted. Broken or indistinct print, colored or poor quality illustrations and photographs, print bleedthrough, substandard margins, and improper alignment can adversely affect reproduction.

In the unlikely event that the author did not send UMI a complete manuscript and there are missing pages, these will be noted. Also, if unauthorized copyright material had to be removed, a note will indicate the deletion.

Oversize materials (e.g., maps, drawings, charts) are reproduced by sectioning the original, beginning at the upper left-hand corner and continuing from left to right in equal sections with small overlaps. Each original is also photographed in one exposure and is included in reduced form at the back of the book.

Photographs included in the original manuscript have been reproduced xerographically in this copy. Higher quality 6" x 9" black and white photographic prints are available for any photographs or illustrations appearing in this copy for an additional charge. Contact UMI directly to order.

UMI

A Bell & Howell Information Company
300 North Zeeb Road, Ann Arbor MI 48106-1346 USA
313/761-4700 800/521-0600

Construction and Calibration of Detectors for High-Resolution Metabolic Breast Cancer Imaging

James L. Robar

Medical Physics Unit
McGill University, Montreal

August, 1996

A thesis submitted to the Faculty of Graduate Studies and Research in partial fulfilment of the requirements of the degree of Master of Science

---

Abstract

Each of two detectors used in our Positron Emission Mammography (PEM) system consists of four 36mm x 36mm x 20mm bismuth germanate (BGO) detector blocks coupled to a crossed-wire anode photomultiplier tube (PMT). To achieve a high spatial resolution, the crystal blocks have been finely pixelated using a diamond saw. In each detector, 36x36 1.9mm x 1.9mm crystal elements are coupled directly to the PMT window and, on the opposite face of the blocks, 35x35 elements are offset by 0.9mm along both the x- and y-axes of the PMT. Techniques developed for the successful machining and surface-preparation of the detector blocks are described. Results indicating the detector block performance in terms of spatial and energy resolution are presented.

As part of a system calibration routine, a novel method for crystal element identification has been developed. This robust and reproducible algorithm succeeds in identifying 59 x 49 crystal elements on each detector face. The results are used to generate a Look-Up-Table (LUT) that is accessed during data acquisition for the effective correction of spatial distortion inherent in the detectors. Crystal identification also facilitates an improvement of the capability for accurate energy discrimination, since the detector gain and energy resolution are considered on an element-by-element basis by accessing an energy LUT. Employing a third LUT, which contains the relative efficiencies of individual crystal elements results in a significant improvement in detector uniformity.

Resumé

Les deux détecteurs de notre système de Mammographie par Émission de Positons sont composés de quatre blocs de germanite de bismuth (BGO) de 36 mm x 36 mm x 20 mm, couplés à un tube photo-multiplicateur (TPM) à multiples anodes. Pour obtenir une excellente résolution spatiale, des sillons perpendiculaires ont été tracés sur les deux faces carrées des blocs à l'aide d'une scie à diamant afin de former des matrices de fins parallélépipèdes droits (appelés cristaux) de 1.9 mm x 1.9 mm. Les sillons d'une des faces sont décalés de 0.9 mm de sorte que chaque détecteur est composé d'une matrice de 36x36 cristaux couplés directement au TPM et d'une matrice de 35x35 cristaux de l'autre côté des blocs de BGO. Les techniques qui ont été développées pour la fabrication et la préparation de la surface des blocs de BGO sont décrites. Les résultats indiquant la performance de ces blocs sont présentés sous forme de résolution spatiale et de résolution de l'énergie.

Une nouvelle méthode faisant maintenant partie de la routine de mise au point pour l'identification des cristaux a aussi été développée. Cet algorithme identifie correctement 59 x 49 cristaux par détecteur de façon robuste et reproductible. Les résultats permettent de générer une table de valeurs qui est utilisée lors de l'acquisition de données pour corriger la distorsion spatiale inhérente aux TPM. L'identification des cristaux facilite aussi la capacité de déterminer l'énergie avec plus d'acuité puisque le gain et la résolution de l'énergie sont assignés à un cristal précis en accédant à une table de valeurs pour l'énergie. De plus, l'emploi d'une troisième table de valeurs qui contient l'efficacité relative de chaque cristal améliore nettement l'uniformité des détecteurs..

Acknowledgements

I would like acknowledge the contributions of my friends and colleagues at the Research Computing Laboratory of the Montreal Neurological Institute (MNI). Kavita Murthy endured the initial learning curve of crystal-cutting and shared her valuable experiences. Alanah Bergman has been active in designing the mechanical structure of the Positron Emission Mammography scanner, and her insight has been valuable. The engineering skills of Ray Clancy have been essential in the domain of detector electronics and data acquisition. Finally, the computing and translation expertise of Yani Picard was also greatly appreciated. In addition, I am very grateful to my supervisor, Prof. C. J.Thompson, for his encouragement, patience, and guidance over the course of this very exciting project.

Many thanks go to Dean Jolly, Don Porter and Shadreck Mzengeza at the MNI radiochemistry lab for their assistance in developing a technique for crystal surface preparation and for reliably providing ^{18}F for phantom studies.

Generous financial support was provided by a scholarship from Fonds pour la Formation de Chercheurs et l'Aide a la Recherche (FCAR). Continued funding for this project is graciously supplied by the Canadian Breast Cancer Research Initiative of the National Cancer Institute of Canada (NCIC).

I would like to thank my girlfriend, Fiona Macintosh, who is a constant source of understanding, inspiration, and diversion.

This thesis is dedicated to my Mum and Dad, for their unwavering encouragement and perspective.

Table of Contents

Acronyms Used

ADC	Analog to Digital Converter
APD	Avalanche Photodiode
BGO	bismuth germanate
CAMAC	Computer Automatic Measurement And Control
CCD	Charge Coupled Device
CFD	Constant Fraction Discriminator
DOI	Depth Of Interaction
FDG	^{18}F-deoxyglucose
FOV	Field Of View
FWHM	Full-Width-Half-Maximum
FWTM	Full-Width-Tenth-Maximum
HV	High Voltage
LOR	Line Of Response
LUT	Look-Up-Table
NEA	Negative Electron Affinity
NIM	Nuclear Instrumentation Module
PEM	Positron Emission Mammography
PET	Positron Emission Tomography
PMT	Photomultiplier Tube
PS-PMT	Position-Sensitive Photomultiplier Tube
PSF	Point Spread Function
PVR	Peak to Valley Ratio
QA	Quality Assurance
SPECT	Single Positron Emission Tomography
TIR	Total Internal Reflection
UFOV	Useful Field Of View

List of Figures

List of Tables

1. Principles of Positron Emission Tomography

1.1. Positron Emission Tomography

Positron Emission Tomography (PET) is a medical imaging modality that measures the spatial distribution of substances labelled with positron emitters in living systems. The potential for using positron emitters for imaging has been recognized since the 1950s when Brownell and Sweet localized brain tumours using the first practical positron camera[1]. Since that time, PET has been used to visualize a host of physiological processes, including blood flow, substrate metabolism, and the binding of minute concentrations of various agents to receptor sites. PET has been used extensively in medical research, providing new insight into disorders including Parkinson's disease, epilepsy, schizophrenia, Alzheimer's disease, and depression. A better understanding of cardiac disorders and stroke has been obtained using PET. Applications in neuropsychological studies are elucidating the response of the brain to various stimuli in terms of blood flow, blood volume or glucose metabolism. In addition, using animal subjects, new pharmaceuticals can be evaluated and screened *in vivo*. Finally, PET has been used successfully to monitor the metabolism and treatment of various cancers.

Positron-emitters and labelled compounds used in PET

The positron-emitters used in PET are isotopes of some of the most prevalent elements found in living systems (carbon, oxygen, and nitrogen). For this reason they can be used to synthesize various compounds that mimic the function of substances found physiologically. The most common radioisotopes used in PET, their half-lives ($t_{1/2}$), and some of the useful labelled compounds produced are listed in Table 1.1. These radioisotopes are typically produced in medical cyclotrons by bombarding stable isotopes with positively charged particles (positrons or deuterons). The nuclear reactions employed for each isotope are also listed in Table 1.1.

Table 1.1. Summary of some of the positron emitters and labelled compounds used in PET.

Isotope	$t_{1/2}$ (minutes)	Nuclear Reactions used	Labelled Compounds	Application in PET imaging
^{11}C	20	$^{10}B(d, n)^{11}C$ $^{10}N(d, \alpha)^{11}C$	^{11}CO	cerebral blood volume
			^{11}C-N-methylspiperone	dopamine D_2 receptor
			^{11}C-Ro15-1788	benzodiazepine receptor
^{13}N	10	$^{12}C(d, n)^{13}N$ $^{16}O(p,\alpha)^{13}N$	^{13}N-amino acids	amino acid metabolism
			$^{13}NH_3$	cerebral blood flow
^{15}O	2	$^{14}N(d, n)^{15}O$ $^{15}N(p, n)^{15}O$	$H_2\ ^{15}O$, $C\ ^{15}O$	cerebral blood flow
			$^{15}O_2$	oxygen consumption
			$C\ ^{15}O_2$	cerebral blood volume
^{18}F	110	$^{18}O(p, n)^{18}F$ $^{20}N(d, \alpha)^{18}F$	^{18}F-fluorodeoxyglucose	glucose metabolism

The labelled compound is administered by injection or inhalation and enters the bloodstream of the subject. The subsequent distribution of the substance throughout the body then closely imitates that of its naturally-occurring analogue.

Basic Principles of PET

Conventional PET scanners consist of one or more rings of detectors surrounding the subject as shown in Figure 1.1. Each detector is composed of an arrangement of dense, high effective- atomic-number (Z) scintillation crystals optically coupled to photomultiplier tubes

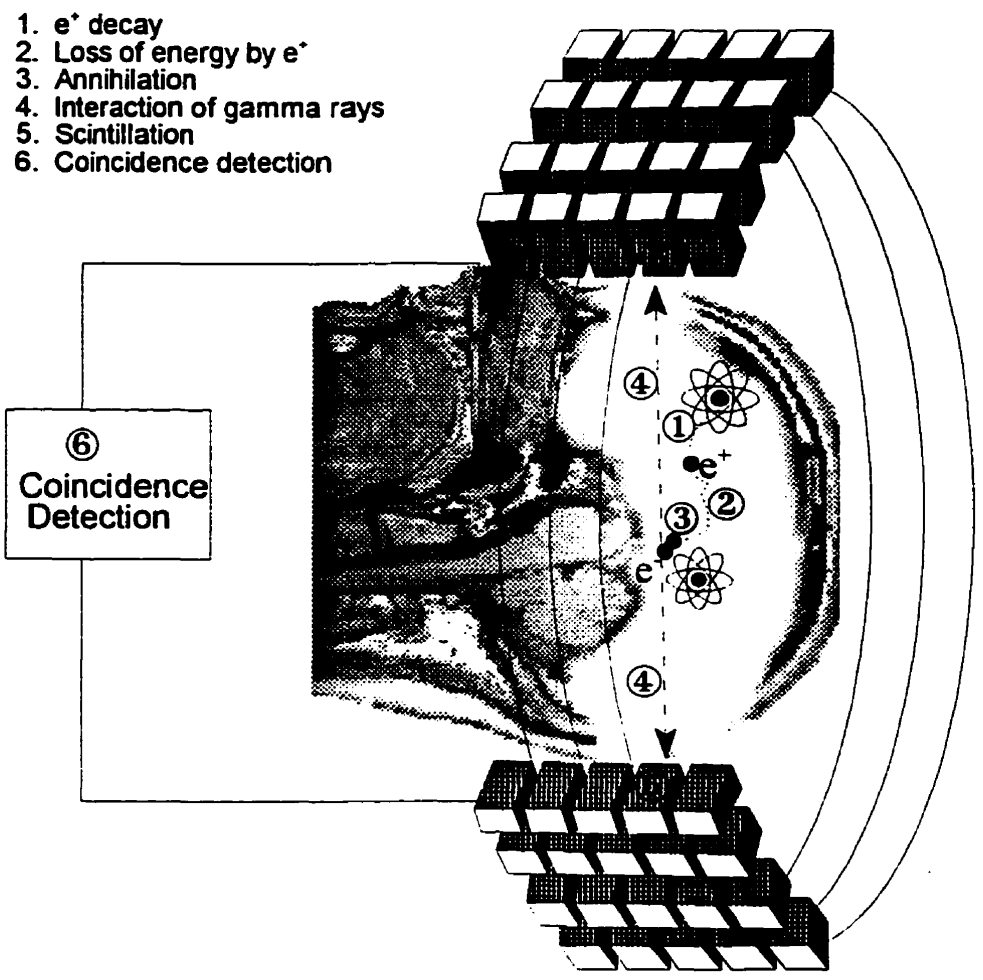

Figure 1.1. Principles of the detection of coincident annihilation gamma rays.

(PMTs). After an amount of the administered positron-emitter has been distributed through the region of the body which is to be imaged, a number of physical processes occur before the location of this activity is detected. These are illustrated and numbered in order in the figure above. Below, the underlying principles of PET are summarized by following these events in order, from the decay of the nucleus to the detection of coincident annihilation gamma rays.

① Positron Decay

The common feature shared between the radioisotopes listed in Table 1.1 is a surplus of nuclear positive charge, making the nuclei unstable. The nucleus decays to a lower energy state by emitting the net positive charge in the form of a positron. This process also results in the conversion of a proton to a neutron, and the emission of a neutrino[2]:

$$p^+ \rightarrow n + e^+ \nu + energy \qquad (1.1)$$

Both charge and lepton number are conserved in this process. The energy released is shared between the positron and the neutrino. The proportion of the total energy imparted to the positron as kinetic energy is a stochastic quantity, but it is described in terms of a maximal value, $E_{\beta max}$, and a probability distribution which depends on the parent nuclide. The value of $E_{\beta max}$ depends on the positron emitter used, as indicated in Table 1.2. The average value of kinetic energy received by the positron is approximately[3] equal to 1/3 $E_{\beta max}$.

Table 1.2. Maximum energy imparted to the positron following the decay of its parent nucleus.

Radioisotope	Maximum Positron Energy ($E_{\beta max}$)
^{11}C	0.97 MeV
^{13}N	1.19 MeV
^{15}O	1.70 MeV
^{18}F	0.64 MeV

② Loss of energy by the positron

Positrons are emitted isotropically from the parent nucleus and travel several millimetres in the medium while continually losing energy through excitation and ionization interactions. A small amount of energy (~1%) is also lost in the form of bremsstrahlung radiation. The distance over which the positron travels is dependent upon the initial kinetic energy and the density of the medium into which it is emitted. The probability for in-flight annihilation of positrons is very low. After a duration[4] of approximately 10^{-9} s, the positron slows down to thermal energies and annihilates with an electron.

③ Positron Annihilation

In positron annihilation, the slow positron combines with a loosely-bound electron located in

one of the shells of an atom in the medium. The combined mass of the two particles (two times 511.1 MeV/c^2) is entirely converted into energy, and two annihilation gamma rays are emitted (three gamma rays may also be created, but the probability of this occurring is very low). The gamma rays emerge from the site of annihilation in approximately opposite directions. This process must conserve both energy and momentum. It is unlikely, however, that the net momentum of the e^+- e^- system is zero just before the annihilation occurs, since the typical energy of the positron at this time[5] is 10 eV, and the electron is orbiting in an atomic shell. In order to conserve momentum, the annihilation gamma rays are slightly acollinear. The deviation of the angular separation of the gamma rays is described[6,7] by a Gaussian distribution in water-equivalent materials, with a full-width-half-maximum (FWHM) of approximately 0.5°.

④ Interaction of the gamma rays

The 511 keV gamma rays will interact with the matter through which they pass. This matter includes both the surrounding material of the subject (i.e. tissue, fat and bone) and, if the photon is not absorbed inside this volume, the dense scintillation crystal in the PET detector. At an energy of 511 keV the probability for coherent (Rayleigh) scattering is negligible, and the energy is insufficient for pair or triplet production to occur. Hence, the dominant interactions of the annihilation gamma rays are Compton (incoherent) scattering and photoelectric absorption.

Compton Scattering

Compton scattering is an interaction that occurs between an incident photon of energy hν and an electron in the medium. Energy is transferred to the electron, and it recoils along an angle ϕ from the initial trajectory of the photon with energy E'. The photon scatters through an angle of θ and emerges with a reduced energy, hν' according to:

$$h\nu' = \frac{h\nu}{1+\alpha(1-\cos\theta)}$$
$$\text{where} \qquad \alpha = \frac{h\nu}{m_e c^2} \qquad (1.2)\ ,$$

where c is the speed of light and m_e is the electron mass. The Compton attenuation coefficient (σ) is nearly independent of the atomic number of the medium in which the photon interacts[8], but increases with electron density. For photons in the energy range of interest in PET, this is the most predominant interaction in tissue. For a 511 keV photon in tissue, the relative probability for Compton scattering (given by σ/μ x 100%, where μ is the total attenuation coefficient) is approximately[9] 99.7%. If a gamma ray is scattered and subsequently detected in coincidence with its mate, this is considered a *scattered coincidence*, as discussed below.

Photoelectric Absorption

In photoelectric absorption, the entire energy of the incident photon is transferred to an electron ejected from the K, L, M or N shell of an atom and to either characteristic radiation photons or Auger electrons. The energy of the ejected photoelectron is $h\nu - E_{bind}$, where E_{bind} is the binding energy of the shell in which it originated. The photoelectric cross section varies with photon energy according to, approximately, $1/(h\nu)^3$, and with atomic number roughly according to Z^3 or $Z^{3.8}$ for low-Z materials[8].

⑤ Scintillation

If a gamma ray escapes the volume of the patient and is incident upon a PET detector, it may deposit energy within the dense, high-Z scintillating crystal through the interactions outlined above. In BGO the relative probability of photoelectric absorption of a 511 keV photon (τ/μx100%, where τ is the photoelectric attenuation coefficient) is approximately 45%, while the relative probability for Compton scattering is approximately 55%. The absorption of

energy by the crystal is followed by scintillation, or the emission of light. This light is detected by the photomultiplier tube to which the crystal is coupled, and is converted into an electrical signal which is detected. The process of scintillation and its detection are discussed in some detail later in this chapter.

⑥ Coincidence detection

As explained below in the discussion of PET detectors, the scintillation light produced is detected by the PMT, and converted into an electrical signal. Two gamma rays are considered to be coincident if the detected signals arrive within a specified time interval, determined by the coincidence resolving time of the system (typically between 3-20 ns). Annihilation coincidence detection is one of the principal features that differentiates PET from SPECT; PET uses "electronic collimation" of the gamma rays to localize the point of the annihilation along a line between the detectors from which the signals were obtained.

The possibility of Compton scatter of the gamma ray was discussed earlier. Because one or both gamma rays may have undergone scattering before coincidence detection, these events degrade the image quality and reduce the accuracy of quantitative measurements[10]. In addition, accidental coincidences occur, corresponding to the coincident detection of two gamma rays originating from separate annihilations. Thus, the total count rate (R) is the sum of the true (R_t), scatter (R_s) and accidental rates (R_a):

$$R = R_t + R_s + R_a \qquad (1.3)$$

The true coincidence rate, R_t, is equal[12] to the product of the positron emission-rate of the nuclide ($R_{positrons}$), the efficiencies of the detectors (ϵ_A and ϵ_B), the geometric efficiency of a detector (g) and a factor accounting for attenuation of gamma rays through a thickness L of matter with an attenuation coefficient μ:

$$R_t = R_{positrons}\ \epsilon_A\ \epsilon_B\ g\ e^{-\mu L} \qquad (1.4)$$

The detector efficiency (ϵ) refers to the fraction of incident gamma rays that deposit a sufficient amount of energy so that they are detected. The geometric efficiency (g) is the ratio of the surface area of the detectors divided the area of a sphere of radius *r* equal to one-half of the detector separation. The accidental coincidence count rate for a given detector pair is determined by the coincidence resolving time of the detectors (τ) and the singles count rates for the detectors ($R_{A\ sing}$ and $R_{B\ sing}$):

$$R_a = 2\tau\ R_{A\ sing}\ R_{B\ sing} \qquad (1.5)$$

The scatter count rate is the rate of detecting both gamma rays from the same annihilation in coincidence, where at least one gamma ray undergoes Compton scatter before detection. Unlike the accidental rate, the scatter count rate cannot be reduced by shortening the detector coincidence resolving time. Quantification of this rate is highly dependent on the scanner used, but for a source located near the midpoint of two detectors, it is:

$$R_s = K\ R_{positrons}\ \epsilon_A\ \epsilon_B\ g^2 \qquad (1.6)$$

The factor *K* is derived empirically and accounts for various geometrical and scanner design parameters. Scatter events are reduced by using energy discrimination, whereby only events with energies located within specified range around the energy spectrum photopeak are accepted. If the spatial distribution of scattered events is quite flat, corrections can be made by fitting a curve to the event distribution obtained at the periphery of the field of view (where no activity is present) and subtracting this distribution from the recorded profiles.

1.2. Spatial resolution in PET

Physical limits on spatial resolution

Two events which occur in the course of positron decay and annihilation introduce physical limits on the achievable spatial resolution of PET. The first is the finite range of the positron before annihilation. The coincident detection of the annihilation gamma rays localizes the *annihilation event*, not the location of the parent nucleus, since the trajectory of the positron is undetermined. This introduces a blurring into the image, reducing the spatial resolution. On average, however, the error in estimating the location of the parent nucleus based on the annihilation location is less than the positron range, since some component of the positron trajectory likely will be along the line of response (LOR) between the two detectors (i.e. there is no error if the positron annihilates at a point along the LOR). Dorenzo et al[11]. have studied the point spread function (PSF) due to positron range. This distribution is expressed by the sum of two exponentials, one accounting for small peak at a very short range where a small number of annihilations occur, and a second which introduces broad tails corresponding to the range of the *majority* of positrons. Because of the presence of these broad tails, the PSF is characterized by a full-width-tenth-maximum (FWTM). For ^{18}F, which produces a comparatively low-energy positron, the resolution broadening due to positron range[12] is 0.22 mm full-width-half-maximum (FWHM) and 1.09 mm FWTM. It has been suggested that confining the positron using a magnetic field would result in improved spatial resolution, but the magnitude of the field required is very high (on the order of 5 Tesla[13]).

The second limit on spatial resolution is introduced by the acollinearity of the annihilation gamma rays. Because the angular deviation of the gamma rays from 180° cannot be determined on an event-by-event basis, localizing the site of annihilation involves an assumption that the gamma rays were emitted in exactly opposite directions. The magnitude of the blurring introduced by this effect increases linearly with detector separation. In typical PET systems, the distance between opposite detectors, D, is typically 50 - 100 cm. For a ring of diameter D=50 cm, for example, since the probability distribution of angular deviation is

Gaussian with a FWHM of 0.5°, this acollinearity of gamma rays originating in the centre of the ring results in a blurring of (±250 mm x tan (0.25°)), or ±1.1 mm. In comparison, for the arrangement of the high-resolution detectors described in this work, a typical detector separation is 50 mm, and the magnitude of the error is ±0.1 mm accordingly.

Intrinsic detector resolution

While the two effects described above impose theoretical physical limits on resolution, the intrinsic detector resolution is a factor that can be controlled to some extent in the design of the imaging system. Most modern PET systems employ either individual scintillators or modular crystal detector blocks from which a number of discrete elements are cut. The width and separation of these elements determine the frequency at which gamma rays are sampled, and therefore largely determines the modulation transfer function of the detector. According to the Nyquist theorem, in order to detect a distribution of activity with spatial frequency of f at a particular location in the FOV of the scanner, the lines of response must pass though that location at a frequency of at least $2f$ in order to avoid aliasing artefacts in the image. Unfortunately, the crystal element dimensions are not the only intrinsic factor determining the frequency response. In addition, if modular detector blocks are used there is some uncertainty in determining in which element in the block the event has occurred. This ambiguity may result from several factors, including limited scintillation photon statistics or imprecision of the readout used to provide positioning signals.

An empirical study by Moses and Derenzo[14] summarizes the various factors affecting spatial resolution discussed above. According to this work, the components add in quadrature, resulting in a spatial resolution of Γ:

$$\Gamma = 1.25 \sqrt{\left(\frac{d}{2}\right)^2 + (0.0022\ D)^2 + s^2 + b^2} \qquad (1.7)$$

Here, d is the crystal element width in mm, D is the detector separation in mm, s accounts for

the positron range and b accounts for the uncertainty in determining of the location of the event within a block detector with multiple crystal elements. If crystal elements are coupled to PMTs in a 1:1 ratio, b equals zero. The factor 1.25 accounts for a degradation of resolution resulting from the image reconstruction process.

1.3. Detectors used in PET

Scintillator Materials

There are several important criteria to consider in selecting a scintillator to be used in a PET detector. First, in comparison to detectors for other nuclear medicine procedures (such as gamma cameras, which employ NaI(Tl) crystals), PET detectors must be able to detect higher-energy gamma rays. Scintillators with very high effective atomic numbers and densities present large cross sections for Compton and photoelectric interactions, and therefore offer high linear attenuation coefficients for 511 keV gamma rays. A second requirement is the production of a detectable number of scintillation photons, at a wavelength to which the PMT is sensitive, following the deposition of energy by a gamma ray. The time scale of this emission is also crucial, since it largely determines the coincidence resolving time, and in turn, the accidental coincidence rate defined in Equation 1.5. Finally, several issues related to bulk properties of the scintillator are important, including whether the material is hygroscopic, and whether it can be easily grown and machined for the construction of PET detector blocks. Table 1.3 summarizes the physical properties of some of the scintillators commonly used in nuclear medicine.

Table 1.3. Physical characteristics of some commonly used inorganic scintillators.

Property	BGO	LSO	GSO	BaF_2	CsF	NaI(Tl)
density (g/cm^3)	7.13	7.4	6.71	4.89	4.61	3.67
effective Z	74	66	59	54	53	50
linear attenuation coefficient, μ (cm^{-2})	0.903	0.870	0.6	0.438	0.42	0.328
avg. number of photons per keV absorbed	4.8	24	6.4	2.0	2.5	40
relative light yield (/100)	15	75	27	5* (fast) 30 (slow)	5	100
scintillation decay time (ns)	300	40	60	0.8 (fast) 620 (slow)	2.5	230
peak wavelength of emission (nm)	480	420	430	225 (fast) 310 (slow)	390	415
refractive index	2.15	1.82	1.85	1.56	1.48	1.85
hygroscopic ?	no	no	no	slightly	very	yes

* BaF_2 has two scintillation components.

The mechanism of scintillation is understood in terms of the energy levels of the crystal lattice[15]. Individual molecules do not scintillate-- this behaviour is a property seen only in the crystal as a whole. Some of the scintillators used for PET do not scintillate in their pure state, and require the introduction of impurities (e.g. Tl is introduced into NaI to facilitate

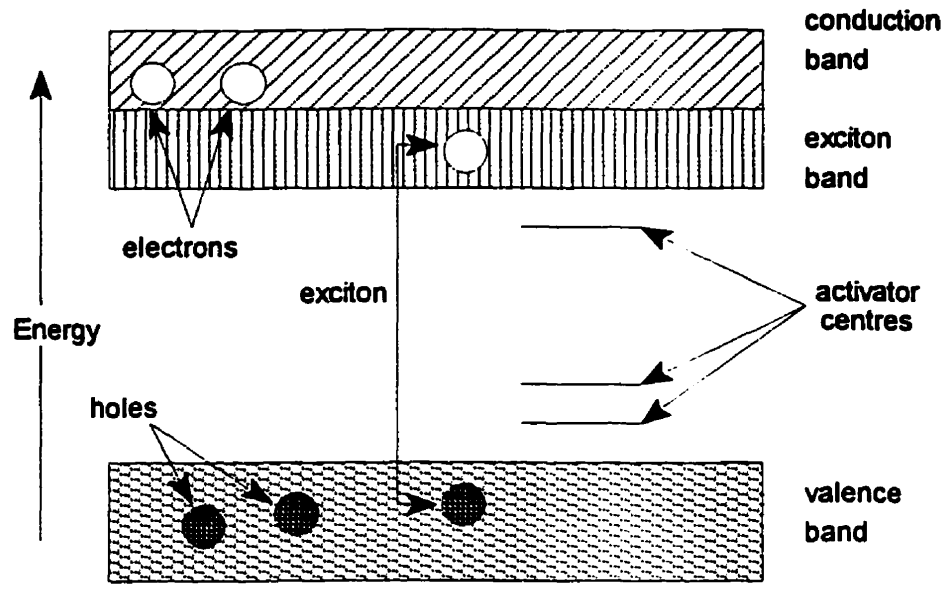

Figure 1.2. A schematic representation of the energy levels of a scintillation crystal.

scintillation at more practical temperatures). This produces *activator centres* between the valence and conduction bands of the lattice which trap excited electrons (see Figure 1.2).

These activator sites are responsible for the light-emitting effect when energy is absorbed. This energy is provided by either the photoelectron or the recoil electron as it slows down in the crystal. When a valence electron absorbs energy, it may be excited to the conduction band, leaving a hole in the valence band. Subsequently, the electron may be trapped in an activator centre before returning to the lower energy state. Three different types of activator centres exist within scintillators: i) *quenching centres*, from which electrons return to the valence band by emitting heat, but not light. This transition is of no use for the detection of gamma rays in PET; ii) *phosphorescence centres* in which electrons may be trapped until they absorb an additional amount of energy, then return to the valence band with the emission of a photon. Although light is produced during this transition, it occurs over a long time scale, and results in an "after-glow" which is a undesirable characteristic in PET scintillators; iii) *fluorescence centres*, from which the electron returns to the ground state very rapidly with the emission of a photon. Because of the useful short time scale of this transition (scintillators commonly used have decay times of 0.8 ns to 300 ns, depending on the crystal), growers of

scintillation crystals aim to increase the number of this particular type of activator centre. Also important in the mechanism of scintillation is the presence of *excitons*, which consist of hole-electron pairs that remain bound (although the electron remains in an excited state). As a neutral association, an exciton moves through the crystal lattice until it is trapped by an activator centre.

Photomultiplier tubes (PMTs)

A photomultiplier tube is an electronic device that is able to generate an electric current in response to even very few incident photons of infrared, visible or ultraviolet light. Figure 1.3 shows a simplified drawing of a PMT. When scintillation photons impinge upon the photocathode, photoelectrons are emitted into the vacuum of the tube and, under the force of an electric field often established by a focusing grid, are directed to the first dynode. The dynode is a metal plate composed of a material that produces secondary emission; for every electron incident, more than one secondary electrons are ejected. As shown in the figure, the photocathode is grounded, and a high voltage (HV) of over 1000 V exists between it and the anode. The potential decreases from the anode to the photocathode according to the value of the resistance between successive dynodes. The electrons are accelerated from one to the next, with multiplication occurring at each stage. The multiplication achieved by this process produces a gain G of

$$G = \xi^n \qquad (1.8)$$

where ξ is the gain per dynode stage and n is the number of stages. Typically, there are 9-16 stages in a PMT.

The secondary emitter material used for the dynode is typically a p-type semiconductor which has been treated to alter its electron affinity (the energy required to liberate an electron from the conduction band to the vacuum level). The characteristic thus introduced into the dynode

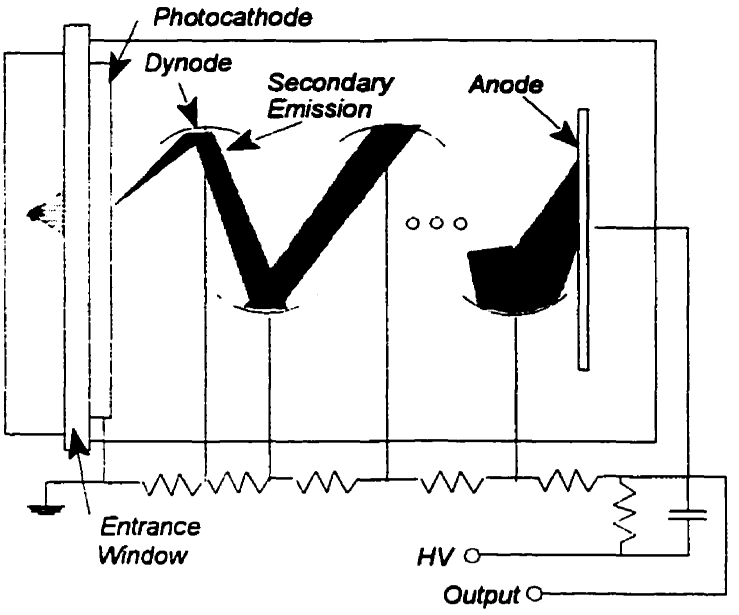

Figure 1.3. Schematic drawing of a photomultiplier tube.

material is called Negative Electron Affinity (NEA), and alters the shape of the energy bands at the surface of the metal. This property causes an electron in the dynode, after excitation to the conduction band, to be *repelled* into the vacuum of the tube. NEA materials increase the depth from which excited electrons can be ejected during secondary emission. Typical NEA materials used include Cs_3Sb, MgO(Cs), and BeO(Cs). Secondary emission gains as high as 130 have been observed in GaP(Cs)[16], but a typical gain[12] per stage (ξ) is 3 to 6.

Cs_3Sb is also used as a photoemissive material in the photocathode, but a large number of possible bialkali materials are available. The photocathode material used must be matched to the wavelength of the scintillation light (e.g. K_2CsSb is used for NaI(Tl) crystals because of its high sensitivity to wavelengths in the blue region of the spectrum). The dark current produced is also a criterion in photocathode selection, and Na_2KSb is a particular candidate that has a very low thermal emission. One characteristic of the photocathode that is particularly important to this work is its *quantum efficiency*, referring to the average number of electrons emitted per incident photon of a given wavelength. The quantum efficiency is determined by three processes affecting the energy of the photoelectron: i) the energy transferred to the photoelectron during the photoelectric interaction; ii) its subsequent loss

of energy as it moves towards the photocathode/vacuum interface; and iii) the escape of the electron over the potential barrier at this interface. The best quantum efficiency reported for photosurfaces is one electron for three incident quanta of light[15]. Typically[12], however, 10 to 30 photoelectrons are produced per 100 incident scintillation photons in the visible spectrum. The number of electrons collected from the photocathode also depends on how efficiently they are routed to the first dynode. These factors can also be responsible for a nonuniformity of quantum efficiency over the photocathode area. As described in subsequent chapters, this nonuniformity may play an important role in the calibration of high-resolution PET detectors.

The photocathode, the dynode chain and the anode are housed within an evacuated glass tube that is often covered with a mu-metal shield in order to prevent the perturbation of the electrons' trajectories by external magnetic fields. Pins at the base of the tube facilitate the application of high voltage and the measurement of the current at the anode.

It should be emphasized that only a single signal is obtained from the type of PMT described above. While the amplitude of this signal is proportional to the number of scintillation photons incident interacting within the photocathode, it does not indicate the position of the scintillation event within the crystal (although, as discussed in chapter 3, multiple PMTs and modular detector blocks are used in conventional PET scanners to decode crystal element positions). A fairly recent approach is the use of a position-sensitive photomultiplier tube (PS-PMT), which differs from its conventional predecessor in the design of the dynodes and the anode. In this device, unlike the arragement illustrated in Figure 1.3, mesh dynodes are used to ensure that there is a spatial correspondence between the centroid of the charge collected at the anode and the location of scintillation photons incident upon the photocathode. The anode of a PS-PMT is a multi-channel structure, consisting of an array of discrete conducting pads or a grid of crossed wires. The positioning signals indicate the location of the charge in two dimensions. Anode wires can be read out independently, or can be coupled together in a resistor voltage-divider chain in order to reduce the number of

channels required. Since the inception of the crossed-wire PS-PMT[17], it has become clear that, when coupled to very small scintillators, this device facilitates PET imaging with very high spatial resolution[18] (on the order of 2 mm).

2. Overview of the PEM system

2.1. Motivation for the development of PEM

Introduction

Breast cancer is the second most common malignancy among women with worldwide annual incidence and mortality of approximately 180,000 and 45,000, respectively[19]. One in ten women is affected by the disease within a lifetime[20], and since 1980, the occurrence of this disease has been increasing at a rate of approximately 3% per year[19]. Because of the prevalence and the morbidity associated with breast cancer, a broad array of novel approaches for its identification and management have been investigated[21]. While effective control of the disease requires the accurate localization of tumours, reliable determination of their stage, and the capability to monitor the response to treatment, no single imaging modality currently provides all of this information. To date, the most commonly-used technique has been x-ray mammography, which provides very high-resolution projection images of the radiodensity of the breast, but does not convey information pertaining to tumour metabolism. We have been developing[22,23,24] a Positron Emission Mammography (PEM) system, which, by employing the principles of PET, works in conjunction with x-ray imaging to provide the "missing" metabolic information. The exact role of PEM in imaging breast cancer is clearly defined by considering both the limitations of conventional mammography and some of the promising results of studies involving the application of PET to breast cancer imaging.

Limitations of X-ray mammography

X-ray mammography is an anatomical imaging modality. While prognoses are sometimes obtained from mammographic results, they are based primarily on the size of the tumour in the image and the fact that the probability for metastasis increases with tumour volume[25]. In order to obtain histologic information concerning metabolism, however, a biopsy of any suspicious lesion is normally performed. Even core needle biopsies are traumatic, expensive,

and cause scarring which limits the accuracy of subsequent imaging of the tumour (i.e. during follow-up monitoring). Furthermore, 53% to 91% of biopsies reveal that the procedure has been performed on a benign tumour[26,27,28]. Clearly, an improved non-invasive means of screening breast cancer must be superior in terms specificity.

Another marginal characteristic of conventional mammography is its sensitivity. Mammograms fail in the detection of up to approximately one-third of primary breast cancers[29]. The sensitivity to detect cancer foci is decreased in the cases of radiodense breasts, multiple microcalcifications, or breasts which have undergone previous surgery[30]. For these reasons, a more sensitive imaging technique is required. A complete and spatially-accurate detection of suspicious tumours would both reduce the occurrence of false-negative results and would provide a more useful description of the tumour for surgery guidance.

PET applications in breast cancer imaging

The strengths of whole-body PET when applied to breast cancer imaging are, in a sense, the opposite of those offered by x-ray mammography; while mammography produces images with excellent spatial resolution but without functional information, PET is capable of providing accurate quantitative metabolic information but has inadequate spatial resolution for the early detection of tumours. The outcome of a number of PET studies conducted to evaluate its role in breast cancer imaging have largely motivated the development of PEM. The most common tracer used in these studies has been ^{18}F-fluorodeoxyglucose (FDG), which accumulates in the tissue following the phosphorylation phase of glucose metabolism. The prospect of differentiating between benign and malignant tumours is based on the preferential metabolism of FDG by the former. This overconsumption may be consistent with an increased expression of the GLUT-1 glucose transport molecule observed on breast cancers[31].

Both the sensitivity and the specificity of PET for the detection of breast cancer are encouraging. Analysis of PET data is performed by using "hot spot" imaging or by using tumour/background quantitation. It has been observed[32] that, compared to normal tissue,

breast tumours take up FDG preferentially by a factor of 8. This contrast is especially large in older women (who are at higher risk for breast cancer) since in such patients there is an increase in the percentage of fatty tissue in the breast, which is not a substrate for glucose metabolism. Based on the overconsumption of glucose by malignant masses, PET has been used[19] to differentiate between malignant and benign lesions with an accuracy of 90%. In these studies, as in most of the investigations conducted to date, there was a prior knowledge of the presence of fairly large tumours (1.0 cm in diameter). Because of the limitations of the achievable spatial resolution of whole-body PET scanners, the accuracy of PET in localizing and characterizing smaller lesions is currently undefined[19].

The assessment of the response of breast cancer to therapy has been explored also. Generally, tumours that have undergone some form of treatment show a decreased uptake of FDG. In one promising study[33], the use of a chemohormonal treatment regimen, when successful in controlling the cancer, resulted in a significant decrease of FDG uptake just 8 days following its administration. Further declines were observed up to 63 days. It was noted also that the metabolic changes preceded changes in tumour size. Moreover, the metabolic changes, as gauged using PET imaging, were *not* seen in non-responding patients.

While these investigations emphasize the utility of PET for breast cancer imaging, the use of a whole-body scanner is unfeasible for several reasons. First, the capital cost of such a system is significant, making it unaccessible for most breast clinics. Second, the spatial resolution is insufficient for metabolic imaging of tumours at an early stage. Even for the most modern commercial scanners (e.g. the ECAT HR Plus), the resolution ranges between 4.5 to 5.5 mm.

The role of the PEM system

The PEM scanner described in the remainder of this chapter will facilitate metabolic breast cancer imaging with a sensitivity and specificity similar to that revealed by the PET studies described above. The device offers several additional advantages over conventional PET

systems, however, including:

- excellent accessibility in terms of cost;
- very high spatial resolution in comparison to that achieved by whole-body PET(~2.0 mm) in order to detect tumours at an earlier stage;
- high detector efficiency, achieved by using a favourable breast/detector geometry, and by employing BGO scintillators of sufficient thickness; and
- the capability to acquire metabolic images with a live display, immediately following mammography, in order to provide immediate guidance for surgery or biopsy. Furthermore, with the ability to classify the metabolic state of tumours, the number of biopsies performed on benign lesions will be reduced.

2.2. Mechanical design and operation of the PEM scanner

While the specific focus of this thesis is the construction and calibration of the PEM detectors, the PEM imaging system includes additional hardware including the assembly for the installation of the detectors, instrumentation for data acquisition, and a computer for image formation and display. This remainder of this chapter provides a brief description of this context in which the detectors are used.

The PEM scanner has been designed to be adaptable to a standard mammography unit, self-contained and transportable. The system components, including an ALPHA workstation and display, optical and hard disk storage media, Nuclear Instrument Modules (NIM) and Computer Automatic Measurement and Control (CAMAC) electronics for data acquisition, are installed on a mobile cart. A video camera will be mounted to this unit for the digitization of mammography films on site. Additional space is available on the cart to transport the detectors and their associated housing.

The PEM detectors have been integrated into a standard mammography x-ray unit by attaching them to a mammographic magnification platform (donated by Philips, Inc.) as

shown in Figure 2.1. The platform and detector assembly lock into place below the x-ray target of the mammography unit. As shown, the upper and lower PEM detectors face each other and are located above and below the top surface of the magnification platform, respectively. As in conventional mammography, the patient's breast is positioned on the platform surface within a region corresponding to the x-ray field, and is compressed by adjusting the vertical position of a plastic compression paddle attached to the mammography unit (not shown in this photograph). The upper detector which is located above this compression plate can be moved vertically to accommodate a range of compression thicknesses. Linear bearings allow the detector pair to move horizontally in tandem, parallel to the chest wall, so that the detectors can be positioned over the breast, panned along one dimension, or retracted completely.

This arrangement facilitates the consecutive acquisition of x-ray mammographic images and PEM images. The protocol is as follows. First, the patient is injected with approximately 2 mCi of FDG (this activity has been found to be appropriate using Monte Carlo simulation[34]). The patient is encouraged to void, to reduce the amount of activity in the bladder during the scan. At the breast imaging clinic, the patient's breast is positioned on the magnification platform with the detectors fully retracted. The x-ray film (located in a tray at the base of the magnification table) is exposed and processed immediately. Next, the PEM detectors are positioned over the breast, and a PEM image is acquired over the course of several minutes.

While the x-ray film provides a projection image of the variation of atomic number in the

breast (since photoelectric absorbtion predominates) with excellent spatial resolution[35] (20 line pairs/mm), the PEM image provides information concerning the metabolism of the suspected cancer. When the detectors are retracted during the x-ray mammography, a Lucite co-registration tool (shown attached to the upper detector in Figure 2.1) produces an outline on

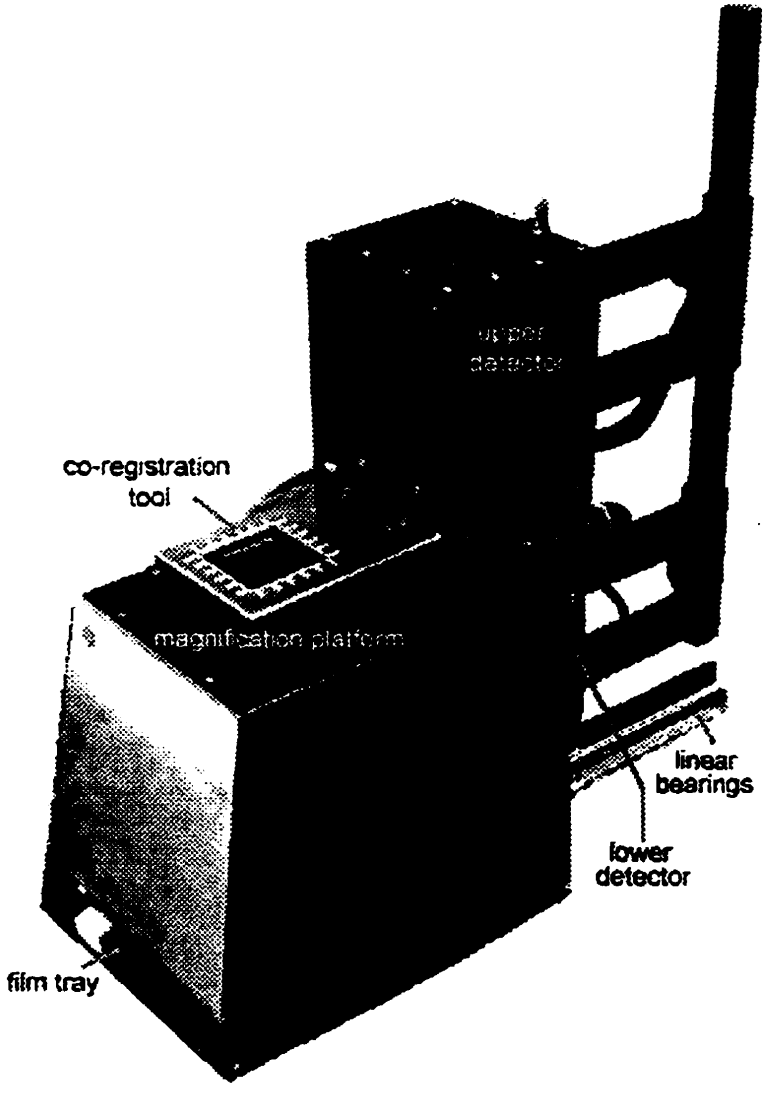

Figure 2.1. The PEM detector assembly.

the x-ray film indicating the position of the field-of-view of the PEM scanner. This facilitates the co-registration of the PEM image and the digitized mammograhic (x-ray) image. The x-ray information is shown in gray scale in this image, while the overlaid PEM image is shown using a colour scale to indicate the distribution of FDG in the breast.

The design of the detector housing, the mechanical structure of the detector / magnification platform assembly and the co-registration tool has been developed by Alanah Bergman. Details of these aspects of the project will be available in her M.Sc thesis.

2.3. The PEM detectors

Because the detectors are the specific focus of this work, their design, construction, and performance characteristics are described in detail in subsequent chapters. Briefly, each detector consists of a Hamamatsu R3941-05 PS-PMT (position sensitive photomultiplier tube) optically coupled to four 36 mm x 36 mm x 20 mm high-resolution BGO detector blocks. Cuts have been made part way through the block thickness from each of the 36 mm x 36 mm faces, so that the block is segmented into small elements, each with a cross-sectional area of 1.9 mm x 1.9 mm. This facilitates the channelling of light from the location of a scintillation event to the borosilicate window of the PS-PMT. These scintillation photons then impinge upon the PS-PMT photocathode.

The electrons produced by the absorption of scintillation photons in the PS-PMT photocathode are amplified by a factor of approximately 10^6 by 16 stages of dynodes across a potential of 1280 V. Both the 5th and 7th dynodes have been split into three segments used to control the gain at the periphery of the field of view. The charge is sensed at a crossed-wire anode plane. There are 18 anode wires across the x-dimension (which is parallel to the patient's chest wall) at a pitch of 3.75 mm and 16 wires across the y-dimension at a pitch of 3.7 mm. The anode wire readout is an Anger-type[36] voltage divider circuit. Another member of our group, Ray Clancy, has increased the resistance values from those set by the manufacturer between the wires closest to the edges of the anode from 1kΩ to 15 kΩ in order to increase the relative weight of signals originating in this area. This modification has increased the area of the Useful-Field-Of-View (UFOV) by approximately[37] 20%. The readout provides four signals (X+, X-, Y+ and Y-) indicating the position of the centroid of the charge distribution, as well as a measure of the event energy (equal to the sum of these

four positioning signals). Preamplifiers with adjustable gain and offset are mounted on the back of the PS-PMT. An event timing signal is taken from the last dynode of the PS-PMT. The specifications of the Hamamatsu R3941-02 PS-PMT used are summarized in Table 2.1.

Table 2.1. Specifications for the Hamamatsu R3941-05 PS-PMT.

Specification	
Entrance window area	73±1 mm x 73±1 mm
Entrance window material	boroscilicate glass
Window refractive index (n)	1.49, 1% dispersion for the BGO emission spectrum[38]
Number of mesh dynode stages	16
High Voltage used	1280 V
Anode Type	crossed-wire 18 wires (in x-dimension) x 16 wires (in y-dimension)
Wire pitch	3.75 mm (x-dimension) 3.70 mm (y-dimension)
Readout	Modified Anger-type resistive chain

Each detector is positioned and secured inside aluminum housing, so that when the boxes are attached to the magnification assembly, the crystal faces are aligned. Lead shielding has been installed around the sides of the box to reduce the detection of gamma rays originating outside of the breast.

2.4. Data acquisition instrumentation

The data acquisition setup used in the PEM system is summarized schematically in Figure 2.2 (the schematic is shown here for one detector only, but is identical for both). The preamplified signals (X+, X-) and (Y+, Y-) are sent to summing operational amplifiers to form the net positioning (X and Y) signals, and an energy (E) signal. These signals are

digitized by an Aurora-14 ADC (Jorway Corp., Westbury, NY). This device has six channels with 128k 12-bit memories and a 1.0μs encoding time. The trigger for this digitization is formed by processing the signal from the last dynodes of both detectors. This preamplified timing signal (t) has a shaping time of 1μs. After a second amplification stage, it is fed to one channel of an Ortec 934 quad Constant Fraction Discriminator (CFD). The logical CFD output and the corresponding signal from detector B form the input to the coincidence module (built at the MNI). A coincidence resolving window of 1 to 10 ns can be set in this module. The output of the coincidence module triggers the ADC. The coincidence module can also be set to produce a trigger pulse for singles events from either detector. (This mode is used in acquiring data for the detector calibration). The memories of the ADC are read out

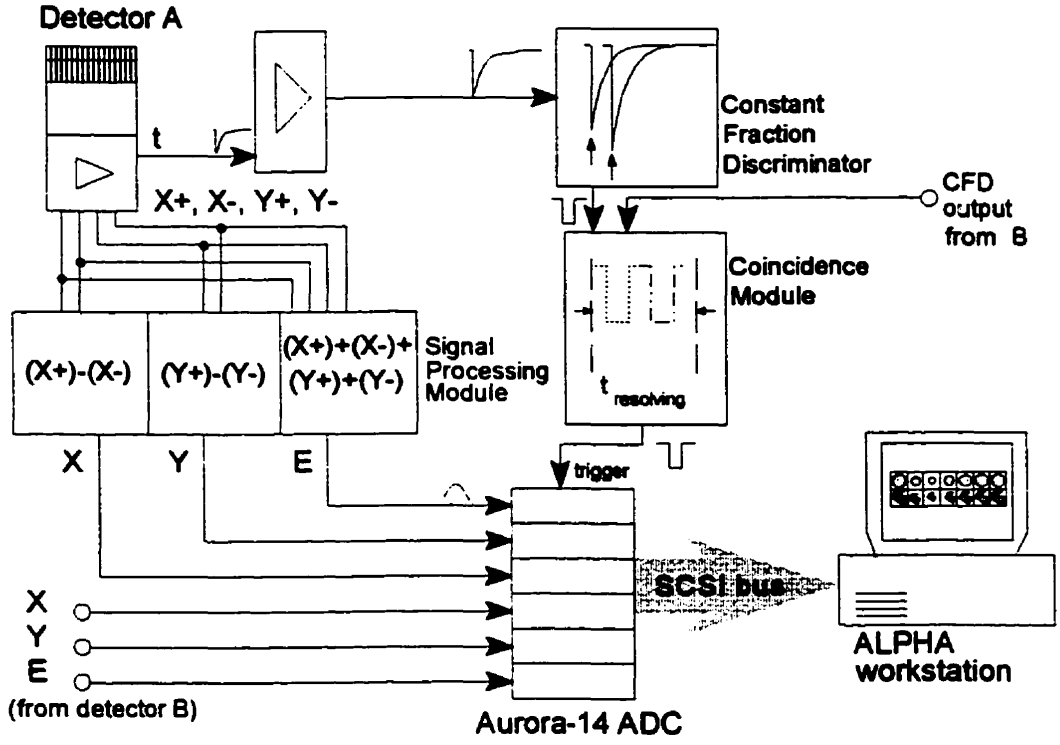

Figure 2.2 The PEM data acquisition system.

periodically for image display and data is relayed to the workstation via a SCSI-2 interface (Jorway Corp., Westbury, NY). All of this instrumentation is contained on the mobile PEM unit; the ADC and the SCSI interface are CAMAC devices, while the remainder of the modules are connected in a NIM crate. Data is stored in list file format on a 4 Gbyte hard

disk. The system also includes a 1 Gbyte disk on which the data acquisition and display software is installed, and an optical disk for the archiving of scan data. At the breast clinic, the workstation runs as a standalone device, but during its development it is connected to a local area network via Ethernet as part of a VMS cluster.

2.5. Image formation and display

In the majority of conventional PET systems, an entire data set called a *sinogram* must be completed before generating an image. A sinogram is a matrix in which the values of the integrals of activity along various Lines Of Response (LORs) are stored as a function their angular orientation and radial distance from the centre of the detector ring. When a PET scan has finished, this data is then filtered and backprojected in order to form an image. In constrast, the PEM system updates the image during the acquisition of the data. We anticipate that this live display will be very useful during a scan in positioning the detectors' FOV and in determining the length of scan required to acquire a clinically-useful image.

When a coincident events occur, the locations on both detectors of the energy transfer from the two annihilation gamma rays are determined. As discussed in Chapter 4, these locations are corrected for the spatial distortion of the detectors, and are specified in terms of the coordinates of crystal elements in the detector block. These coordinates define a Line Of Response (LOR) passing though the thickness of the breast between the two detectors. As shown in Figure 2.4, the intersection points of the LOR with seven equally-spaced planes through the breast thickness are determined. Seven corresponding images are formed by incrementing the elements of 72 x 72 matrices corresponding to the locations of these intersections. The value by which a matrix element is incremented, I, is weighted by several factors according to

$$I = K \times \frac{e^{\mu l}}{S(x,y,z)\ \epsilon_A\ \epsilon_B} \qquad (2.1)\ ,$$

where ϵ_A and ϵ_B are the efficiencies of the crystal elements of detectors A and B respectively, in which the gamma rays were absorbed. S is a correction called the *solid angle function* that accounts for the dependence of the probability of the detection of an annihilation pair on the (x, y, z) location of the annihilation. An example of this function (for a single plane) is shown in Figure 2.3. μ is the linear attenuation coefficient of the breast tissue (the compression plate material is approximately tissue-equivalent), and l is the path length along the LOR through

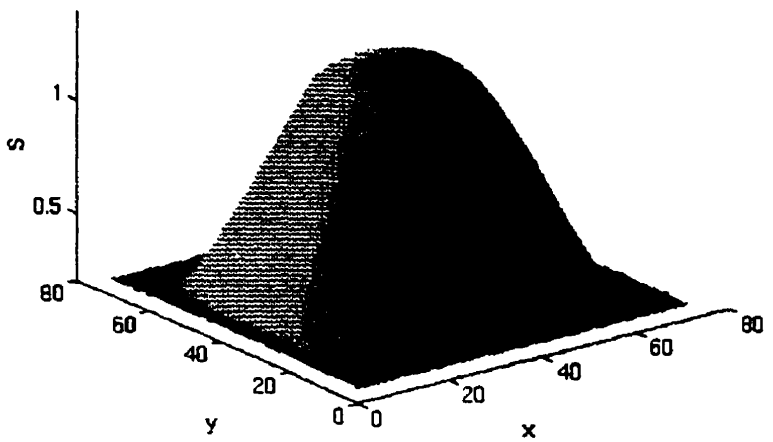

Figure 2.3. The solid angle function (S) corresponding to a single plane through a compression thickness of 50 mm.

the breast and the compression plate. Finally, K is a factor required to scale this value so that it is in the appropriate range (0 to 100) to update an integer image matrix.

Although this is a limited-angle reconstruction, Figure 2.4 illustrates the concept by which depth information is obtained by the focusing of the activity distribution onto the seven planes. The distribution is best focused in the image corresponding to the plane closest its actual location in the z-dimension of the breast volume. As the LORs spread and intersect with planes further away from the activity distribution, the images produced become increasingly blurred.

As the data is acquired, the memories of the ADC are read periodically and all seven images are updated. The colour map and window level and width are adjustable on-line, as the image is formed. After the scan, images can be zoomed, filtered, and co-registered.

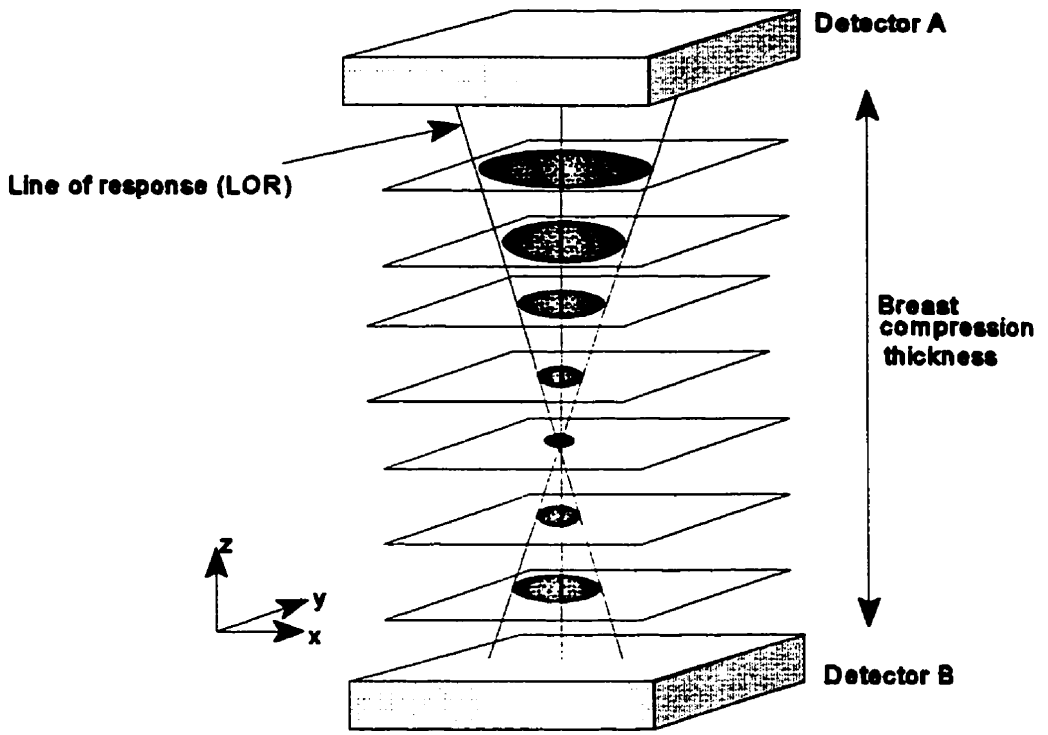

Figure 2.4. Seven images are formed by backprojecting through seven planes through the compression thickness. The activity distribution is best focused in the plane closest to its location in the z-dimension.

3. Construction of the PEM detectors

3.1. Introduction

Although the effects of annihilation gamma-ray non-collinearity and the positron range limit the achievable spatial resolution of PET, it is also determined by the detector resolution (i.e. the spatial frequency at which incident gamma rays are sampled by the detector blocks.) Particularly for systems such as mammographic or animal scanners, in which the detector separation is comparatively small, the detector resolution must be improved over that commonly found in PET before the ultimate limits on resolution are met. Since the inception of PET, various novel ideas for detector construction have been employed to improve the spatial resolution. Several of these approaches involve the use of hardware in addition to the scintillator / photomultiplier combination. Moses et. al.[39,40,41] have optically coupled one end of small crystal scintillators to PIN photodiodes which provide the positioning information and a measure of Depth Of Interaction (DOI). In this arrangement, PMTs are coupled to the other in order to provide a sufficiently fast timing signal. Lecomte et al.[42] have achieved a similar one-to-one scintillator/detector coupling with BGO/Avalanche Photodiode Detector (APD) modules. Worstell et. al[43]. are developing a detector that determines the location of interactions occurring in thin slabs (several millimetres in depth) of unsegmented scintillators using ribbons of waveshifting fibres coupled to multi-anode PMTs.

Similar to the approach taken in constructing the PEM detectors, other techniques of improving detector spatial resolution have focused on refining the scintillator/PMT design without employing additional types of detector hardware. The general trend in this domain has been a reduction in the length and width of the scintillator elements, while scintillator depth has been maintained in order to preserve detector efficiency. While the collection faces of scintillator elements have become smaller, the active areas of individual photomultipliers have not diminished in size accordingly. This has led to the challenge of coupling an increasing number of scintillators to a single PMT and using decoding schemes to locate the

scintillator of probable interaction. Several of the PMT/BGO detector block combinations used recently are summarized in Table 3.1. These examples can be categorized into two main groups: i) those employing single-channel PMTs, and ii) those employing multi-channel or multi-anode position sensitive PMTs. As indicated in the table, there is a significant increase in the number of crystal elements per unit area in the latter category, made possible by the comparatively precise position-sensitivity of the PMTs used.

As the density of individual crystal elements increases however, the problem of "radial-blurring" becomes more important, caused by the penetration of oblique gamma rays through adjacent crystal elements in the detector block. With small crystal elements, such a gamma ray can travel through several elements before interacting and depositing a sufficient amount of energy so that it is detected[44]. This mis-positioning has been reduced by determining the depth-of-interaction of the gamma ray using a variety of detectors offering some precision of crystal depth-resolution. For example, one-bit of depth information has been obtained by using two layers of different scintillators with different characteristic decay times[45]. Recently, two forms of lutetium orthosilicate (LSO) exhibiting different decay constants have been identified, and each is characterized by a different decay time[46]. Another approach involves maintaining a temperature gradient across the depth of a BGO scintillator. In this case, depth information is also determined by measuring the decay time, since it increases as the temperature decreases[47] (at ~5 ns/°C). The PIN photodiode/BGO/PMT detector developed by Derenzo and Moses[48] promises depth resolution of < 5mm FWHM to eliminate this positioning ambiguity. As suggested by Rogers et al., a simpler technique of partially filling the EXACT HR PLUS block with a black material causes the light collection, and thus the energy signal amplitude to depend on the DOI. This work is quite similar to that of Thompson[49,50], Bartzakos[51,52] and Murthy[44], who also used a lossy scintillator, in the form of a black-band scintillator cladding, to introduce this dependence.

Table 3.1. Several recent BGO crystal detector block / photomultiplier schemes used for PET. (+ indicates that the element depth varies within the block.)

Investigators	Crystal matrix dimensions (# elements)	Element dimensions (mm^3)	Detector PMT / Block arrangement
Thompson et al.[53], 1995	36 x 36 comb-slit matrix	2 x 2 x 6.5, and 2 x 2 x 11.5	One Hamamatsu R-3941 PSPMT / four blocks
Y. Shao et al.[54], 1995	8 x 8	2 x 2 x 10	One 64-channel Philips XP1702, or XP1722 multi-channel PMT / block
S. Cherry et al.[55], 1995	8 x 7 (EXACT HR)	2.9 x 5.9+	Two rectangular dual PMTs / block
	8 x 8 (EXACT HR+)	4.39 x 4.05+	Four circular PMTs / block
J. Rogers [56], 1994	12 x 12	~4 x ~4 x 30	Four PMTs / block
	16 x 16	~3 x ~3 x 30	Four PMTs / block
Tornai et al[57]., 1994	6 x 6 (GE Advance)	4 x 8.4 x 30	Two Hamamatsu R1548 dual PMTs / block
M. Watanabe et al.[58], 1992	1 x 33	1.7 x 10 x 17	One Hamamatsu R3941 PSPMT / four arrays
T. Yamashita et al.[59], 1990	1 x 34 comb-slit array	3.5 x 10 x 17	One Hamamatsu R3941 PSPMT / array
T. Yamashita et al.[60], 1990	-	5 x 12 x 30	One 4-segment Hamamatsu R3309 PMT / Four discrete elements
W. M. Digby et al.[61], 1990	6 x 8	3.5 x 6.25+	Two dual Hamamatsu R1548 PMTs / block
M. Dahlbom et al.[62], 1988	4 x 8	6 x 12+	Four square Hamamatsu R2497 PMTs / block
H. B. Min et al.[63], 1987	4 x 4	4.4 x 8.5 x 55	Two dual Hamamatsu R2404 PMTs / block
L. Eriksson et al.[64], 1987	4 x 4	4.5 x 9.5 x 25	i) Two dual PMTs / block; or ii) One round Philips XP4702 PSPMT / block
H. Uchida, et al.[65], 1986	5 x 5	5 x 5 x 20	One round PSPMT / block
	9 x 9	3 x 3 x 15	
M.E. Casey, R. Nutt[66], 1986	4 x 8	5.6 x 13.5 x 30	Four square PMTs / four blocks

A machined PEM detector block is shown in Figure 3.1. The dimensions of the block are 36 mm x 36 mm x 20 mm, such that four blocks are coupled in a 2 x 2 array to the window of the Hamamatsu R-3941 PS-PMT. In this arrangement, there are 5184 separate elements on each of the two detectors. The double-layer comb-slit design of the PEM detector block was used in order to meet three objectives:

- the capability for very high spatial resolution, made possible by the high spatial sampling frequency (1.4 mm spacing between crystal element centres);
- reasonable detector efficiency; and
- the provision for one-bit depth-of-interaction information.

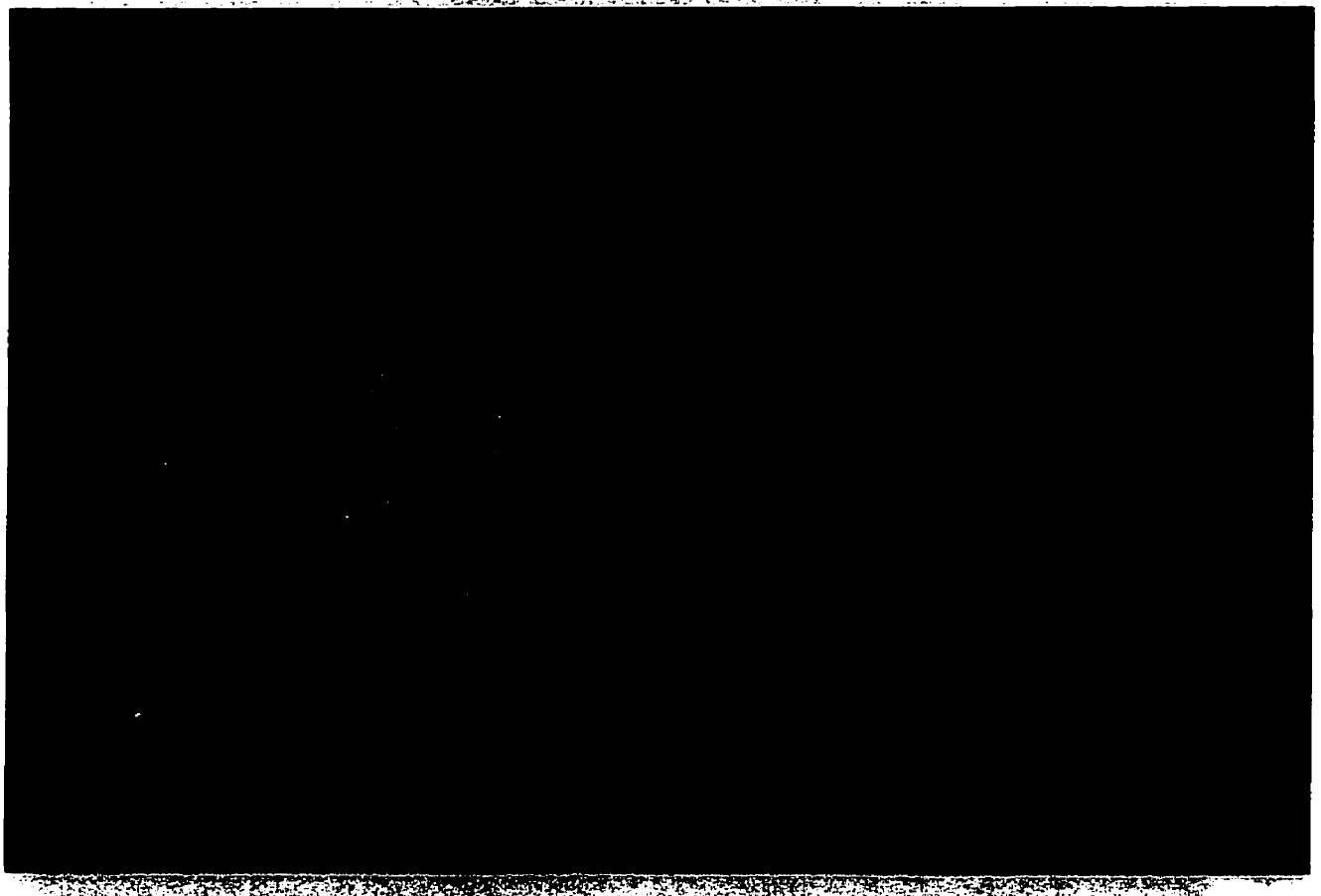

Figure 3.1. A PEM detector block. Separate elements are cut partially through the 20 mm block thickness from both faces, and remain attached to a 2 mm - thick solid region.

The first criterion is achieved by using closely-spaced crystal elements that are small in their length and width dimensions. Initially, the prospect of purchasing commercially-available individual polished BGO pillars was attractive in that it would eliminate the need for machining a solid block. The price quotation[67] for the required 72 x 72 x 2 pillars of dimensions 2 mm x 2 mm x 15 mm was approximately of US$ 90,000. This option was immediately abandoned due to its unfeasible cost. In comparison, the eight BGO solid blocks required for a complete PEM were purchased for US$ 2,400, but a major investment in terms of time and materials was required in order to determine a feasible technique of manufacturing the blocks.

The crystal elements are cut partially through the block thickness from each of the 36 mm x 36 mm faces. The crystal elements coupled directly to the PS-PMT, (referred to here as "proximal elements") are 11.5 mm long, while the "distal elements" on the other side are 6.5 mm in length. As determined using Monte Carlo simulation[68], these depths ensure an equal probability for interaction in both layers. The crystal elements are 1.9 mm x 1.9 mm in cross-section, except for those around the edge of the block face distal to the PMT, which have dimensions 0.9 mm x 1.9 mm. The offset shifts the elements on one face from those on the other by one-half of the crystal element width in both the x- and y-dimensions. Figure 3.2a) illustrates this offset, which produces a crystal centre-to-centre separation of 1.4 mm on the diagonal of the block. In this arrangement, by accepting coincident events between any pair of crystal elements, there are approximately 30×10^6 possible lines of response.

Figure 3.2b) illustrates the principle behind the detection of scintillation light from the PEM block. While scintillation light originating in a proximal element is capable of reaching the PS-PMT photocathode directly, photons produced in an element on the other side of the block travel through the four elements below it. In this case, although the light incident upon the photocathode emerges from four separate elements, the detected centroid of charge at the multi-wire anode corresponds in location to crystal element in which the scintillation light originated.

Two main design considerations aim to facilitate the second criterion of reasonable detector efficiency. First, the loss of crystal mass during the cutting and etching steps of the manufacturing procedure has been minimized as much as possible. Second, while the element length and width are very small, the block thickness is 20 mm, which is comparable to many of the blocks employed by conventional PET scanners listed in Table 3.1 . This large depth-to-width ratio of the crystal elements, however, necessitates the third criterion. Without the provision of some DOI information, the mis-positioning of oblique gamma rays would become critical in terms of the degradation of spatial resolution. The determination of DOI in the block is not continuous, however; by using a crystal-identification technique, discussed in subsequent chapters, one bit of depth information is ascertained to indicate whether the event occurred in the proximal or distal layer of elements.

In terms of both the large number and the small length and width dimensions of its crystal elements, the PEM block represents a significant departure beyond the others summarized in Table 3.1. As the resolving capability of PS-PMTs continues to improve, one of the emerging challenges associated with using densely-packed arrays of scintillators is their successful manufacture. While BGO remains an attractive scintillator because of its comparatively high linear attenuation coefficient, its hardness and fragility become very important characteristics when it is to be cut and polished. Furthermore, the loss of mass and the degradation of the surface finish produced by machining a BGO into small elements threatens to degrade both the overall detector efficiency and the detector energy resolution. In developing the PEM system, we have completed the machining of some 16 detector blocks. The remainder of this chapter describes, in some detail, the methods of cutting, surface preparation and optical coupling that were used. These methods have proven to produce blocks in a reasonable amount of time, at an affordable cost (~ US $400 / block, including the cost of saw blades), with a low failure-rate.

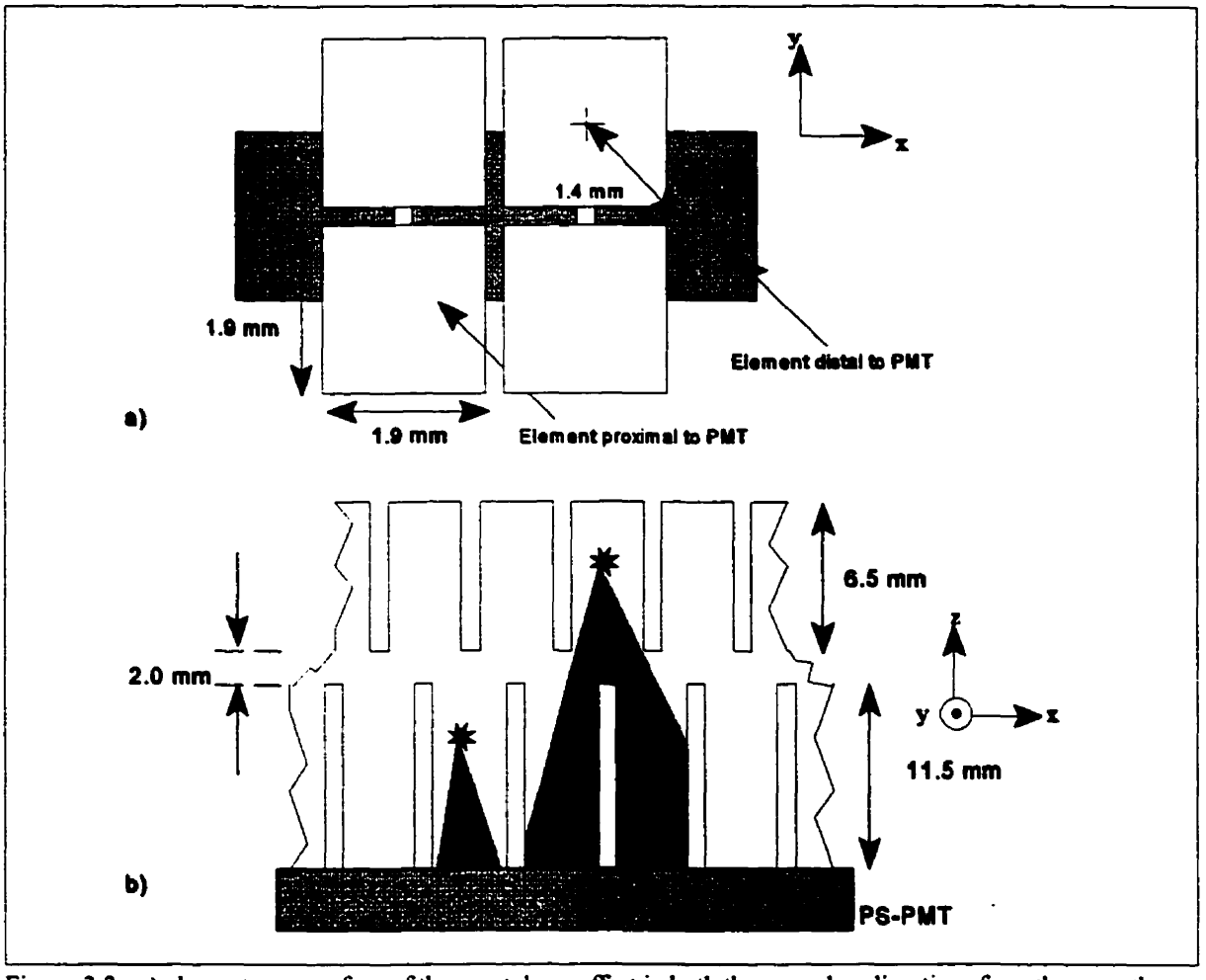

Figure 3.2. a) elements on one face of the crystal are offset in both the x- and y- directions from those on the opposite face. This results in a crystal separation of 1.4 mm on the diagonal. b)Scintillation photons from a distal element reach the PS-PMT through the four proximal elements below it.

3.2. Machining the PEM Bismuth Germanate block detectors

The solid BGO crystals were ordered (from Alpha Spectra, Inc., CO, USA) cut to the desired dimensions and polished to a mirror- finish (Figure 3.3). The dimensions of the crystals deviated from the nominal values by, maximally, 0.1 mm, a tolerance equal to that which was achievable using our saw for crystal cutting. The cost of each crystal, at the time of purchase (1994) was ~US$300. The mass of each uncut crystal was recorded in order to determine

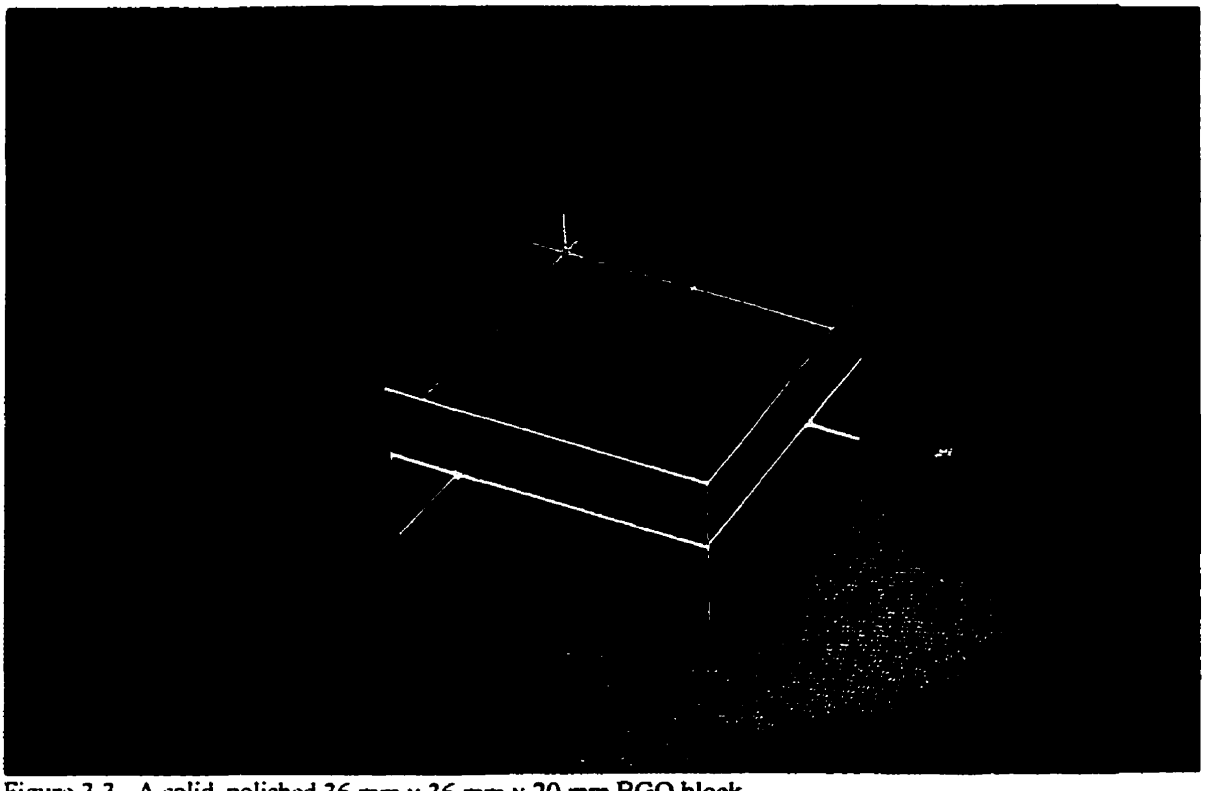

Figure 3.3. A solid, polished 36 mm x 36 mm x 20 mm BGO block.

the percentage mass lost as a result of cutting and surface preparation.

The crystal cutting was done using an Ultra-Tek 8840/60 saw, modified by mounting a dedicated vice to the surface plate of the translation stage. In order to achieve very narrow cuts into the BGO, very thin (0.15 mm and 0.25 mm) circular blades were used (model DWH3102, South Bay Technology Inc., CA, USA). These blades are 7.6 cm in diameter, with a diamond surface around the outer ~1 cm. The motor of the saw is fixed to the saw chassis, while the saw translation stage offers two degrees of freedom. In order to position the crystal relative to the blade, the translation stage was moved in the direction perpendicular to the blade face, by turning a manual precision screw. A tolerance of approximately 0.1 mm can be achieved in this positioning. One 20 mm x 36 mm crystal face was used as an origin for locating the cut positions. This origin was located accurately by using an ohmmeter connected between metal surface of the blade and the aluminum surface of the vice making contact with the crystal. The translation stage also moves parallel to the blade face. As the blades cut through the crystal, the rate of this travel is slow but continuous, and is controlled

by a motorized drive.

Figure 3.4 illustrates the cutting procedure, with a crystal held in the vice below the motor shaft and the diamond blades. Multiple blades may be mounted on the shaft, and are separated by 1.85 mm-thick steel flanges. This facilitates multiple cuts to be made in a single pass of the block and reduces the opportunity for the mispositioning of cuts, since the element thickness is controlled by the thickness of the flanges. Although, as shown in the figure, normally only three blades were used, six blades can be mounted on the shaft at once. Now that we have gained confidence in the reliability of the cutting technique, we intend to use the full six blades simultaneously to reduce the time required for cutting by a factor of two.

Another parameter to be determined was the blade rotation speed, which was adjustable up to 6000 rpm. After experimenting with this value, a value of 1500 rpm produced satisfactory results.

Because of the hardness and fragility of the BGO, a *very slow* feed-speed was required, and the gearing-ratio of the auto-feed motor was modified to achieve a minimal value of 0.05 mm/s. Although a single pass of the crystal requires roughly 18 minutes at this setting, various speeds were tested, and using this lowest speed clearly reduced the occurrence of defects during the cutting. A steady stream of coolant (water mixed with rust-inhibitor) was positioned over the blade and crystal at all times to prevent the heating and expansion of the blade or the crystal, and to remove BGO dust trapped in the narrow cuts. After completing all of the cuts in one direction, the block was rotated through 90° and the cutting of the block face was completed. Including the time required to realign the crystal between cuts, it was possible to complete a single block during one 8-hour day. After the cutting of a block had been completed, it was extremely important to clean and lubricate the all moving parts thoroughly, particularly the translation stage rails and screw. The mixture of BGO sawdust and coolant is very effective in seizing the moving parts of the saw if left to dry overnight.

Since the cuts in the PEM block extend almost through the entire block thickness, the jaws of a standard vice would crush the fragile crystal elements, particularly those at the edge of the block. For this reason, a dedicated vice, illustrated in Figure 3.5, was designed so that only 2 mm - wide surfaces on the inside of either jaw make contact with the uncut section of

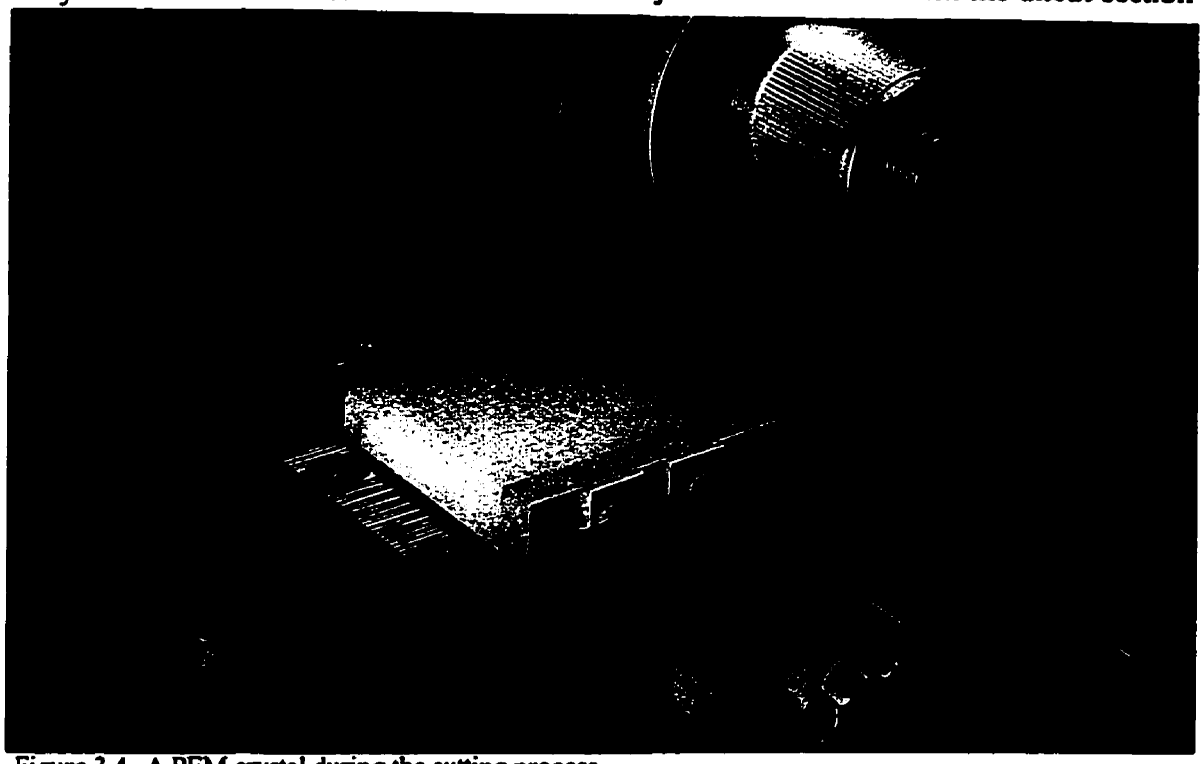

Figure 3.4. A PEM crystal during the cutting process.

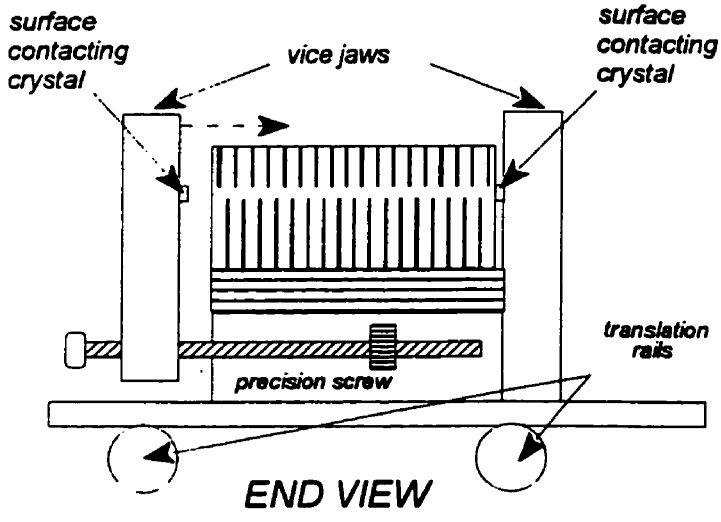

Figure 3.5. The vice designed to hold PEM block without the application of force on cut crystal elements.

the crystal. With this fixture, the block could be clamped securely without the concern of breakage. Spacers bolted below the block control the depth of the cuts.

During the machining of the first few of the 16 PEM blocks cut to date, a discouraging amount of breakage occurred. Since that time, a number of important details of the procedure have been refined and several difficulties have been overcome. While cutting the last 8 blocks, the success was consistent and promising, with approximately 99% of the elements cut from a single block remaining intact. Having gained some valuable experience, we anticipate repeating this procedure to manufacture additional blocks for other scanners. The most crucial problems encountered and subsequently solved during the crystal cutting therefore merit documentation. In decreasing order of severity, these problems were:

i) *The incorrect alignment of the translation stage relative to the saw blade.* When the "precision" saw was received by the supplier, the alignment of the automatic-feed motion was not exactly parallel to the blade face. During the cutting of the first crystal, this resulted in misaligned cuts and a discouraging amount of breakage. To solve this problem, a surface face-plate was mounted to the motor shaft, and a dial indicator was used to align the saw to a precision of $\sim\pm 0.025$ mm. Based on this achievable precision, the approximate error in the angle between the direction of travel of the crystal and the blade face is 0.03° .

ii) *The intermittent travel of the automatic feed.* This problem was identified by observing the motion of the screw that moves the crystal along the long axis of the saw; instead of turning continuously and smoothly, the blades were accelerated in discrete jumps into the BGO. This very likely caused the blades to grab, resulting in the cracking of crystal elements. After aligning and lubricating the translation stage liberally, this problem was eliminated completely.

iii) *The use of an inappropriate feed speed.* Moving the translation too quickly increased the occurrence of crystal breakage. The feed speed was lowered progressively from one crystal

to the next. The value of 0.05 mm/s seems to strike a balance between completing the cutting in a reasonable amount of time and minimizing the number of elements lost.

iv) *Continuing cutting after the blades had become worn.* On average, one blade was exhausted per detector block. The symptom of a worn blade was a deviation of the crystal cut from the normal to the block surface. Unfortunately, even after gaining the experience of cutting many blocks, it remains difficult to anticipate this problem solely by observing signs of wear on the blade cutting surface. After each pass of the crystal, the straightness of the cuts was scrutinized. If a cut appeared to be deviating from the normal, the blade responsible was replaced at a cost of US$150.

v) *The use of blades that were too thin.* Initially, we were intent upon making the cuts as narrow as possible to minimize the loss of BGO and thus detector efficiency. Use of the 0.15 mm - thick blades, however, resulted in some crystal breakage, but more commonly, in cuts deviating from the perpendicular to the crystal face. Increasing the blade thickness to 0.25 mm improved the quality of the cuts significantly.

vi) *Inadequate preparation of the blade surface.* In order to prepare the surface of the diamond blades, both before their initial use and after the completion of some amount cutting, it was necessary to cut several millimetres into an abrasive solid provided by the supplier. This "sharpening" of the blades was repeated before the cutting of each new crystal face, and clearly improved the straightness of the cuts, reduced crystal loss, and increased the longevity of the blades.

After resolving these problems, the results of cutting were satisfactory and consistent. The masses of all crystals were again determined after cutting. The amount of BGO lost by cutting was, on average, 31%±3% of the original mass of the block.

3.3. Surface preparation of the block detectors

By observing the side faces of several crystal elements lost during the cutting procedure, it became apparent that the diamond blades produced a very rough surface finish. As described later in this chapter, this results in a degradation of the light collection and, in effect, of the energy resolution as well. Other investigators have tried several methods of polishing the surface of scintillation crystals, including using abrasive papers, abrasive powders[69] such as Ce_2O_3, and acid etching.

In order to improve the surface finish of the PEM block, the 0.25 mm separation of adjacent

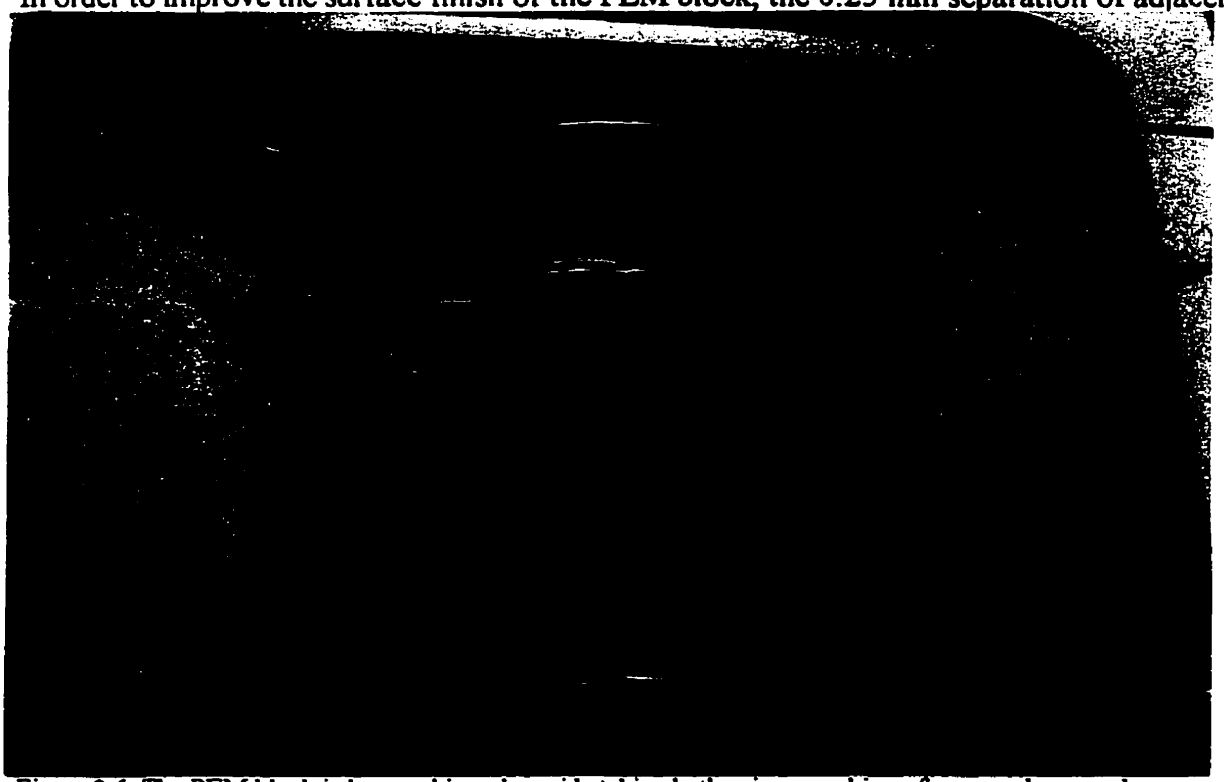

Figure 3.6. The PEM block is lowered into the acid etching bath using a cushion of coarse glass wool.

elements limits the variety of possible methods to those not requiring the application of abrasives such as papers or powders. Moreover, following cutting, the crystals are extremely fragile, and it was important to minimize the amount of handling required. For these reasons, acid etching was chosen as the method of surface preparation.

Several fragments lost during the cutting process were available for experimentation with various acid solutions and etching durations. Etching using a 30% HCl / 70% HNO_3 solution for five minutes produced the best results in terms of the light collection achieved[70], and also resulted in an acceptably low quantity of lost BGO. Figure 3.6 shows a PEM detector block during the etching process. In order to eliminate the need for handling the block excessively and to prevent exposure to the caustic acid, the crystal was placed on a ~5 cm x ~20 cm band of coarse glass wool, and by holding the ends of the wool, was lowered into a 500 ml beaker containing acid solution. The wool also supports the crystal above the floor of the beaker, and because it is course, permits the acid to flow through the bottom-most cuts. The beaker was then set in an ultrasonic bath (without heat) for the 5 minute duration. The block was removed from the acid immediately, and excess acid was allowed to drain from the crystal cuts. The block was rinsed several times under a narrow stream of water. Finally, ethanol was used for a second rinse. This evaporated rapidly, leaving a dry, polished crystal.

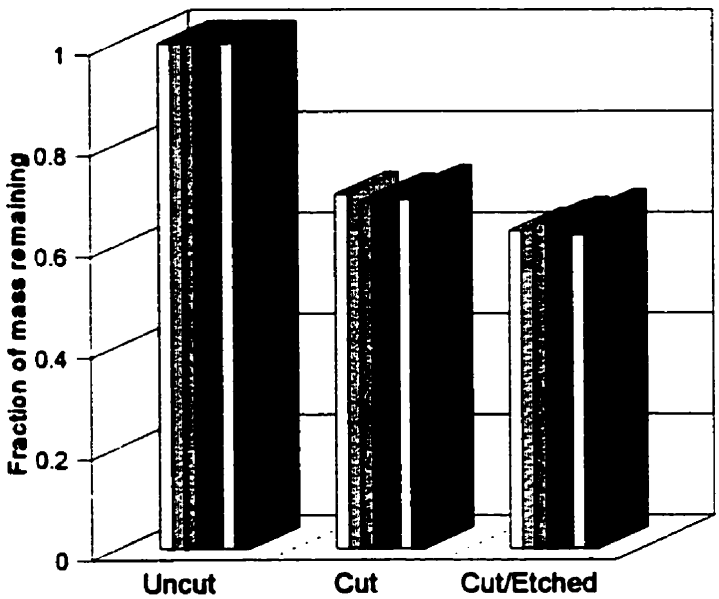

Figure 3.7. Crystal mass lost during stages of manufacture.

The crystals were weighed once again at this point, in order to determine the amount of BGO lost during the etching process. The average additional mass lost was 6%±1% (of the original

mass of the uncut block). Figure 3.7 summarizes the mass of the BGO lost during each stage of manufacture.

As for the crystal cutting procedure, there were several details of the acid etching technique requiring refinement before satisfactory results were achieved. So that the process may be repeated without encountering these pitfalls once again, the main problems are summarized below:

i) *Subjecting the crystal to too much vibration in the ultrasonic bath during the etching process.* The initial experiments conducted to determine the appropriate acid solution and etching duration to use were performed using single *fragments* of BGO, not full blocks composed of multiple elements. Although 5 minutes of vibration in the ultrasonic bath appeared to be optimal for a small fragment, it resulted in considerable crystal element loss (up to ~10 elements) when used for a full PEM detector block. It is likely that this duration of vibration simply weakened the attachment of the crystal elements to the solid region of the block, or caused the crystal elements to break at points at which stresses were introduced during the cutting. This loss was reduced considerably by maintaining the five-minute etching duration, but decreasing the duration during which the crystal was vibrated in the ultrasonic bath to two minutes. It was found that the surface preparation did not suffer (as measured in terms of light output) as a result of this modification to the original technique.

ii) *Total immersion of the crystal in water following etching.* Some means of removing all of the acid from the block was required after the etching duration had finished. During the first attempt at etching, the crystal suffered an additional loss of elements simply because it was immersed in a water bath for rinsing. The excess acid in the cracks of the crystal reacted vigorously with the water, producing a fairly violent bubbling. A number of fragments were broken off as a result of this reaction. Spraying a narrow stream of water over the entire block eliminates this unnecessary risk of breakage.

iii) *The use of a magnetic stirrer to circulate the acid bath.* In order to obtain a uniform etching of the surfaces of all of the crystal elements, we tested two techniques to ensure the constant circulation of the acid through the saw cuts. The first technique of using the ultrasonic bath seemed to produce acceptable results. A second technique was also tested, whereby the crystal was supported on a glass platform above the floor of the beaker containing the acid. A magnetic stirrer was placed below it, and spun slowly throughout the etching duration. This method resulted in a very poor, "scratched" surface finish, and was therefore abandoned.

3.4. Optical isolation of adjacent crystal elements: crystal potting

PET detector blocks are normally finished by applying some kind of reflector to the surfaces of the individual scintillator elements. For the PEM block, the purpose of adding a reflecting material is two-fold. First, if scintillation photons are incident at the side-walls of the crystal element at an angle less than the critical angle for Total Internal Reflection (TIR), some fraction will be transmitted outside of the crystal volume (according to the Fresnel laws of reflection and transmission). In order to recover this light, it is desirable to reflect these photons back inside the scintillator. Second, if scintillation photons escape from the volume of a crystal element, it is possible that they may enter an adjacent element. This effect would undermine the original motivation behind cutting the crystal; optimally the light should be channelled directly to the photocathode of the PS-PMT. By covering individual elements with a reflector that is opaque to the scintillation light, adjacent elements are optically isolated.

Various reflecting materials have been suggested, used in simulations, and in some cases used experimentally, including aluminum foil[71], MgO[72], $BaSO_4$ attached using an organic binder[73], white paint[74], and TiO_2[75]. As for the case the etching process, it is the 0.25 mm width of the cuts which limit the possible options; any material requiring mechanical packing between the

crystal elements was rejected, since this additional handling would introduce further opportunity for calamitous damage. The material settled upon, based on suggestions by Andrew Truman (Dept. Physics, University of Southampton), was a two-part pourable epoxy (model EPO-TEK 301-2, Epoxy Technology Inc., MA, USA), to which a white, opaque, reflective pigment was added (pigment REN DW0131, Ceiba Geigy, MI, USA). Several characteristics made this mixture an attractive candidate. The epoxy has a very low viscosity (260 cps), so that it is easily distributed through the narrow saw cuts without trapping large bubbles of air. It also offers a long pot life (8-hours), low thermal expansion (62 $x10^{-6}$ cm/cm/°C), and does not produce exothermic heat while curing.

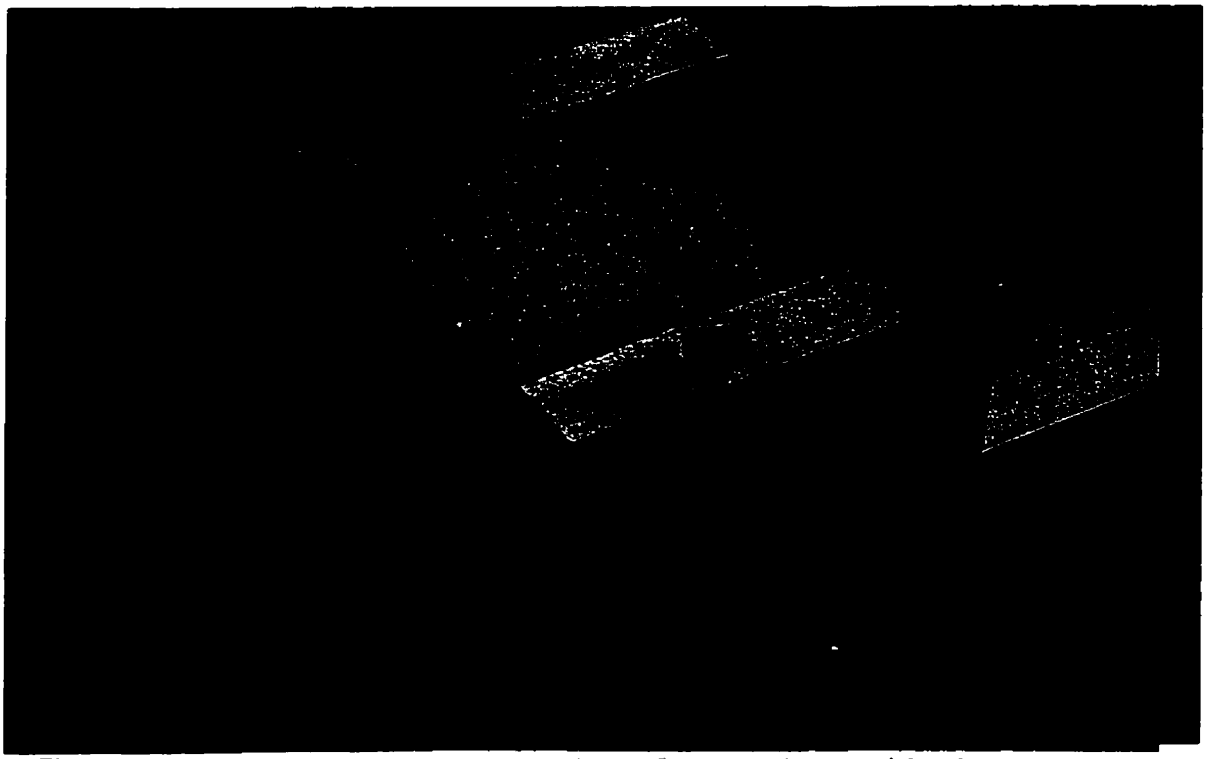

Figure 3.8. An aluminum mould was constructed to confine the potting material to the empty space between crystal elements.

Because of the low viscosity of this potting material, if it is poured into the saw cuts of the block, it simply drains out under the force of gravity before curing. For this reason, an aluminum mould was designed, as shown in Figure 3.8. The walls of this mould are secured with bolts after the crystal is positioned, and the mould is tightened around the crystal block. The inner dimensions of the mould were machined very carefully to 36.10 mm x 36.10 mm,

with a tolerance of ~0.07 mm. These dimensions ensure that the mould accommodates all of the crystals supplied, and that the crystal elements at the edge of the block are not crushed. The height of the mould walls are 21 mm. The inner walls and the surface plate were polished in order to facilitate the release of the crystal once the curing had completed. Several compounds were tested as mould-releases, including household oil, silicone lubricant, and white grease, but the most effective by far was a cooking spray containing silicone (i.e. Mazola™).

Each of the two cut faces was potted separately; the longer (11.5 mm) crystal elements were potted first, since they were most prone to breakage. For these elements the pigmented epoxy was poured so that its final level was just below the top surface of the crystal to allow this face to be optically coupled to the PS-PMT. For the opposite face of the crystal, the epoxy was poured so that it was flush with the top surface of the mould, 1 mm above the crystal face. Approximately 30 hours after pouring the epoxy, before it had hardened completely, the crystal was removed from the mould. Any excess epoxy could be cleaned from the coupling-surface of the crystal with methylene chloride (CH_2Cl_2).

3.5. Optically coupling the detector blocks to the PS-PMT

After four crystals had been cut, etched and potted, two layers of Teflon tape were wrapped around the 20 mm x 36 mm faces. This tape serves two functions; it is used to reflect light escaping from either the outermost elements of the blocks or from the 2 mm - deep uncut region in the block, and it also provides optical isolation between neighbouring crystal elements at the interface of the four blocks. Four blocks were placed in a 2 x 2 array, and approximately five layers of Teflon tape were wrapped around the sides of this full crystal arrangement. Finally, white plastic tape was wrapped over the Teflon to increase mechanical support holding the four detector blocks together.

Several different optical coupling materials have been used in by other investigators[71,73], such

as silica oil and optical grease. In addition to very high transmittance at the wavelength of the scintillation light (480 nm), we were concerned with the following characteristics when choosing a coupling material:

- It was necessary to apply a very thin, uniform layer between the crystals and the PS-PMT window. A thicker layer would result in increased spreading of light due to refraction as the light was transmitted from the crystal through the coupling material. This is especially important if the indices of refraction of the coupling material and the BGO differ significantly.
- It is important to have the option, if necessary, of releasing the crystals from the PS-PMT window without the use of heat or strong solvents. This property would become critical in the case of a malfunction of the PMT or the breakage of one or more crystals. If the detector blocks were attached permanently, an irreparable problem involving either the PMT or the crystals would render the whole assembly useless.
- Sufficient mechanical strength is required in order to allow the PS-PMT/crystal assembly to be rotated and inverted without the loss of coupling.
- The coupling compound should not shrink or produce heat during its curing.

The criteria were met by using a silicone elastomer called SYLGARD 186 encapsulating resin (Dow Corning, MI, USA). This is a two-component polymer in a pourable form. While the transmittance of this substance is not provided by the manufacturer, it has produced satisfactory results when used previously[76] for the coupling of BGO to photomultiplier tube windows. Moreover, a comparison between an energy spectrum obtained when using optical grease (with 99% transmittance for 310 nm $<\lambda<2500$ nm) with that obtained using the same block and the silicone elastomer indicated no degradation of light output.

After mixing one part of the curing agent with 10 parts base resin, a considerable amount of air was trapped in the mixture. The degassing of the elastomer for ~30 minutes in a vacuum chamber was therefore required. The vacuum was released several times to break small

bubbles which formed at the surface. After degassing, the elastomer was allowed to stand for about 10 minutes to allow tiny unreleased bubbles of gas to dissolve into the solution.

A very thin layer of the elastomer was painted onto both the PS-PMT window and the crystal face. The PS-PMTs were supported, windows upwards, and the block arrangement was aligned carefully. The curing proceeded with the crystals pressed against the window under the force of gravity. After 48 hours, the thin layer of elastomer was not completely dry, so black plastic tape was used to secure the crystals to the PS-PMT. Even after five days, although the crystals were securely coupled, the elastomer remained tacky to the touch. The considerable amount of time required for the curing of thin layers of Sylgard 186 is an inconvenience; this is acknowledged in the product specifications[77]. When completely cured, the elastomer assumes a rubber-like consistency.

3.6. Characteristics of PEM block detectors at various stages of manufacture

Because of the considerable cost of BGO and the labour required to complete a PEM detector block, it was not possible to test a wide array of etching techniques and surface preparations on the full size crystal. In order to determine whether the methods should be modified in the future, and to characterize some system parameters, both the light collection efficiency and the spatial resolution were monitored for all of the crystals produced, at each stage of manufacture.

Energy Characteristics

The energy characteristics of a scintillator are commonly described in terms of the energy resolution, defined as

$$Energy\ Resolution = \frac{\Delta E_{FWHM_{pe}}}{E_{pe}} \times 100\% \qquad (3.1)\ ,$$

where $\Delta E_{FWHM\ pe}$ is the full-width-half-maximum (i.e. in ADC channels) of the spectrum photopeak, and E_{pe} is the ADC channel of the centre of the photopeak. Minimizing the energy resolution is important to permit the discrimination between true photopeak events and those resulting from scattered radiation or pulse-pileup. A second description of the energy characteristics is *the light collection efficiency*, which refers to the number of scintillation photons, per keV of energy deposited in the crystal, which reach the PMT photocathode and are detected. Maximizing this quantity is very important for a number of reasons. First, the light output of BGO is comparatively low to begin with (12-15% of that for NaI(Tl)). Second, the accuracy of determining of the location of the gamma-ray interaction is often limited by the poor statistics of collected photons. Third, the light output is the principal factor determining the timing resolution of the system[75].

Factors affecting light collection efficiency

As shown by Ishibashi[73], the light collected from a rectangular BGO scintillator is a linear function of the energy of the gamma-ray absorbed in the crystal. If both the attenuation and reflection of scintillation light in the crystal could be eliminated, the collection efficiency of a scintillator would be proportional to the solid angle from the origin of the scintillation event subtended by the collection face. There are several additional factors, however, which determine the light collection efficiency. Many of these may be controlled in the design of the detector.

Scintillator Geometry

The loss of scintillation photons as they travel through the scintillator medium has been described[73] previously in terms of two main components. First, if the initial irradiance (ie. the energy per unit time per unit area) of the light is I_o, it will be attenuated in the medium

according to

$$I_{atten} = I_o e^{-\mu d} \qquad (3.2)$$

where I_{atten} is the intensity after the light has traversed a path of length d thorough a medium of linear attenuation coefficient μ. Second, if in addition to traversing a path length d, the light reflects n times at the walls of the scintillator before reaching the collection face, the irradiance at the scintillator / PMT interface will be

$$\begin{aligned} I' &= I_{atten} R^n \\ I' &= I_o e^{-\mu d} R^n \end{aligned} \qquad (3.3)$$

where R is the reflectance at the crystal face. For polished crystals, the light will undergo Fresnel reflection, and R will vary accordingly with the angle of incidence. Now, in order to make an estimate of the effects of varying the geometry of the crystal, consider Figure 3.9, showing a crystal of width w in which the origin of the light occurs at a distance l from the collection face, and a distance $w/2$ from the side wall.

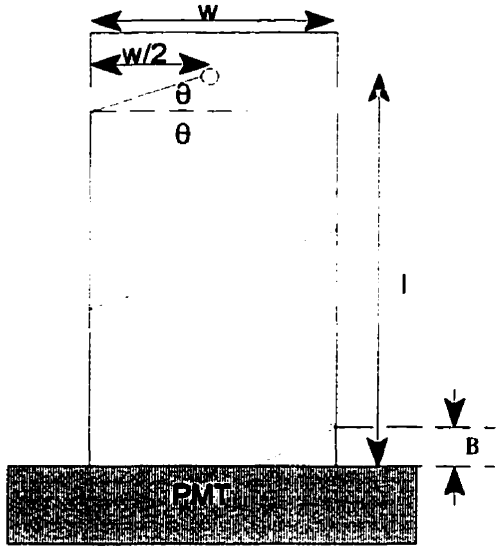

Figure 3.9. Scintillation within a polished crystal with parallel sides. A scintillation event occurs a distance l from the PMT, mid-way across the crystal width, w.

In this arrangement, the total path length is

$$d = \frac{w}{2\cos\theta} + \frac{nw}{\cos\theta} + \frac{B}{\sin\theta} \qquad (3.4)$$

where the first term is the initial distance to the side wall, the second term accounts for the lengths travelled between n reflections, and the third accounts for the final segment from the wall to the collection face. Now, B may be expressed as

$$B = l - w \tan\theta \left(n + \frac{1}{2}\right) \qquad (3.5) \ ,$$

and the total path length simplifies to

$$d = \frac{l}{\sin\theta} \qquad (3.6) \ .$$

The number of reflections, n can be stated in terms of w, l, and θ:

$$n = round\left(\frac{l}{w \tan\theta}\right) \qquad (3.7) \ ,$$

where the fraction inside the parentheses is rounded down to the nearest integer. Finally, using these definitions of d and l, the irradiance at the crystal face is

$$I' = I_o \, e^{\frac{-\mu l}{\sin\theta}} \, R^{round\left(\frac{l \tan\theta}{w}\right)} \qquad (3.8) \ .$$

Although this is a two-dimensional simplification of a three-dimensional problem, the dependences of light output on geometry and surface finish are apparent in this expression. As a result of an increased number of reflections and a longer total path length, the light output decreases for longer and narrower crystal elements. Figure 3.10 shows the irradiance at the collection face calculated using this model as a function of l, for reflectances ranging from 1.00 to 0.50, for θ=45°.

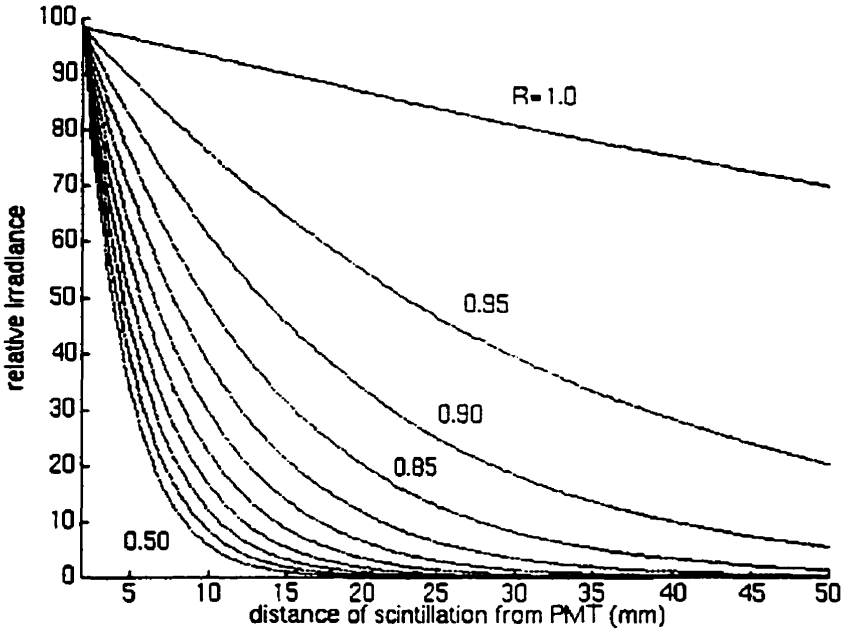

Figure 3.10. The relative irradiance of at the crystal collection face as a function of the distance of the scintillation origin from the PMT, for reflectance values ranging from 0.50 to 1.00 in increments of 0.05.

Scintillator Surface Preparation

Figure 3.10 emphasizes the importance of achieving a high reflectance at the walls of the scintillator. A number of differing approaches have been used in the past to increase the surface reflectivity of scintillators. In some cases, the sides of scintillators have been polished in efforts to ensure Fresnel reflection. In this condition, TIR is possible for light incident at angles greater than the critical angle $\theta_c = \sin^{-1}(n_{crystal} / n_{surround})$, where $n_{crystal}$ and $n_{surround}$ are the indices of refraction of the crystal and its surrounding medium, respectively. For BGO/air interface (for BGO, n=2.15), TIR is especially prevalent with $\theta_c = 27.7°$. For more acute angles, a proportion of the incident photons will escape the crystal. For this reason scintillators are coated with a reflective material which serves to redirect the photons back inside the crystal volume. These reflectors are commonly *diffuse*, and the distribution of reflected light is greatest along the normal to the reflector surface, as predicted by Lambert's law[78].

For mirror-polished scintillators with a high degree of symmetry, however, the problem of *light trapping* occurs, whereby the scintillation photons are repeatedly totally internally reflected at all faces and are unable to exit through the collection face over an acceptably short time scale. For a rectangular parallelepiped BGO crystal coupled to a PMT with optical grease (with n=1.55), up to 46% of light can remain confined within the crystal[79]. It has been demonstrated that trapped light may be released by introducing various asymmetries such as bubbles in the crystal volume or sloped crystal faces[75]. A simpler modification shown to reduce light trapping is sanding the crystal face opposite to the PMT[74]. In the case of the PEM block, no intentional asymmetries were introduced. Although the etching process is effective in terms of increasing light output, it was observed that *i)* the roughness caused by cutting was somewhat nonuniform over the face of a crystal element, and *ii)* the surface finish produced by acid etching was not always uniform. Both of these artefacts of the manufacturing process should serve to reduce internal light trapping.

As described in the literature, the surface preparation which produces the optimal light output seems to depend on a number of factors, including the scintillator geometry. Ishibashi et al[73]. have described a useful empirical study of the light output as a function of the "shape parameter" ℓ/w, (crystal length over width, as defined in Figure 3.9) of BGO rectangular parallelepiped crystals coated with a $BaSO_4$ reflector. As (ℓ/w) increases, the light output decreases very rapidly for (ℓ/w) < 2. For (ℓ/w) > 2 the light output declines further for rough and coated crystals, but for polished and coated crystals, further decreases in light output occur *very gradually* with increased (ℓ/w). Moreover, while for lower shape parameters the light output is best for rough crystals, for (ℓ/w)>6 more light is collected when polished crystals were used. These findings are consistent with the results obtained for the PEM detector blocks for which the total length of an element is 20 mm (from one face to the other), and thus (ℓ/w) > 6. As illustrated later in this chapter, crystal polishing was found to improve the light output from the block significantly.

Optical coupling of the scintillator to the PMT

The possibility for a further degradation of light collection exists at both the crystal/optical coupling interface and at the optical coupling / PMT window interface. While the indices of refraction of several optical coupling materials and many PMT windows are comparable (on the order of n=1.5), the index of refraction BGO is considerably higher. Thus, while a certain proportion of light will be reflected at the coupling/PMT window interface as predicted by the Fresnel equations, it is the crystal/coupling interface that presents the more serious problem, with a potentially low critical angle for TIR. Derenzo and Riles[75] have used a Monte Carlo simulation to illustrate that the light collection from a polished BGO crystal can be improved by a factor of 2.7 by increasing the coupling index of refraction from n=1.52 to n=2.0. Similarly, Klein and Schölermann[78] have found through simulation that the insertion of acrylic or glass light pipes between the scintillator and the PMT reduces light output. An additional problem resulting from a refractive index mismatch at this interface is the refraction of the light from its crystal element of origin, through the optical coupling material, to an "incorrect" region of the photocathode.

In selecting material for coupling the PEM crystals to the PS-PMT, we were concerned with a number of criteria described earlier in this chapter. The silicone elastomer used has an index of refraction[80] of $n_{elastomer}$=1.43. This will result in a critical angle θ_c for the BGO/elastomer interface of 41.7°. Therefore, scintillation light incident on the side walls at angles greater than (90° - 41.7°) = 48.3° will undergo TIR at the crystal/coupling interface. This undoubtedly degrades the energy characteristics of the PEM detector, but both the scarcity of other materials with higher n and the attractive physical properties of the elastomer make it an acceptable candidate as an optical coupling compound. Because $n_{elastomer}$ is slightly less than the index of refraction of the PS-PMT window (n_{window}=1.49) total internal reflection will not occur at this second interface.

Figure 3.11 illustrates the energy spectra for one of the PEM blocks at various stages of manufacture. At each stage, the block was wrapped in several layers of Teflon tape and

positioned at the centre of the PMT. The greatest light output was achieved using the polished, uncut BGO block, as indicated for this block by the photopeak located at ADC channel 109. Cutting reduces the light output dramatically, and the photopeak at channel 37 is barely discernable from lower-energy events. This light loss is likely caused by the very course finish of the crystal elements at this stage, reducing the reflectance of the surface. Without the presence of an effective reflector surrounding the elements, most of the light transmitted at the sides of the crystal elements is not collected. Fortunately, acid etching serves to recover much of this lost light, increasing the photopeak location to channel 102, almost to that of the uncut block. Evidently, the acid etching is very effective in increasing the reflectance of the crystal element faces. As shown, however, the final step of adding the potting material reduces the light collection dramatically, and results in a photopeak at channel 57.

This drastic loss of light output following the final potting stage of production merits some comment, especially in light of the fact that other investigators have observed a dramatic *increase* in light output after coating BGO scintillators[81]. The base of the potting material, an Epo-Tek epoxy, has been designed specifically for coupling optical components. Although for our purposes a white pigment has been added, this material is likely coupling to the surface of the crystal elements. As compared to a reflector which does *not* couple to the crystal, this will *increase* the critical angle for TIR since $n_{epoxy} > n_{air}$. While clearly ineffective as a reflecting material, this material succeeds in optically isolating adjacent elements and greatly improves the durability of the fragile etched crystal. From the point of maximizing light output, however, the crystal potting remains the step of the manufacturing process leaving the most room for improvement. It is conceivable that by replacing the potting material previously used with an effective reflector, the light output could exceed that of the uncut block, since the cutting and etching undoubtedly leave asymmetric "defects" that may serve to release trapped light. Similar energy spectra were acquired for each of the PEM blocks manufactured. Table 3.2 gives the average energy resolution, calculated according to equation 3.1, for each stage of production.

Table 3.2. The effect of cutting, etching and potting the PEM detector block on energy resolution.

stage of manufacture	energy resolution (%)
Uncut	23
Cut	50
Cut and Etched	38
Cut, Etched and Potted	53

While the spectra in Figure 3.11 are representative in illustrating the trend in light output at various stages of production for all of the PEM blocks completed to date, a marked variability in photopeak location was observed between blocks. Figure 3.12 shows the energy spectra for three different completed PEM blocks. This variability in light output became evident following the crystal cutting stage, and therefore may arise from differences between blocks in the surface finish of the cut elements, which in turn may depend on the amount of wear of the blades used. Regardless of its origin, this difference in light output between detector blocks emphasizes the necessity of using energy Look-Up-Tables (LUTs); if energy discrimination is to be performed during acquisition by specifying thresholds in keV, the energy/channel conversion must be known and stored in advance for each crystal block, and in fact, for each individual crystal element.

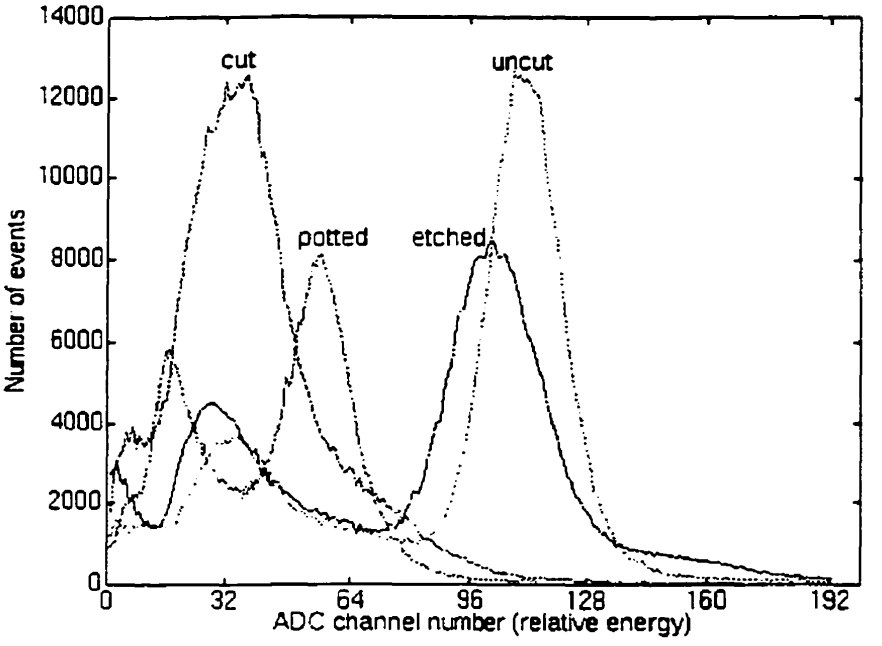

Figure 3.11. The energy spectra for the same PEM crystal block at various stages of manufacture.

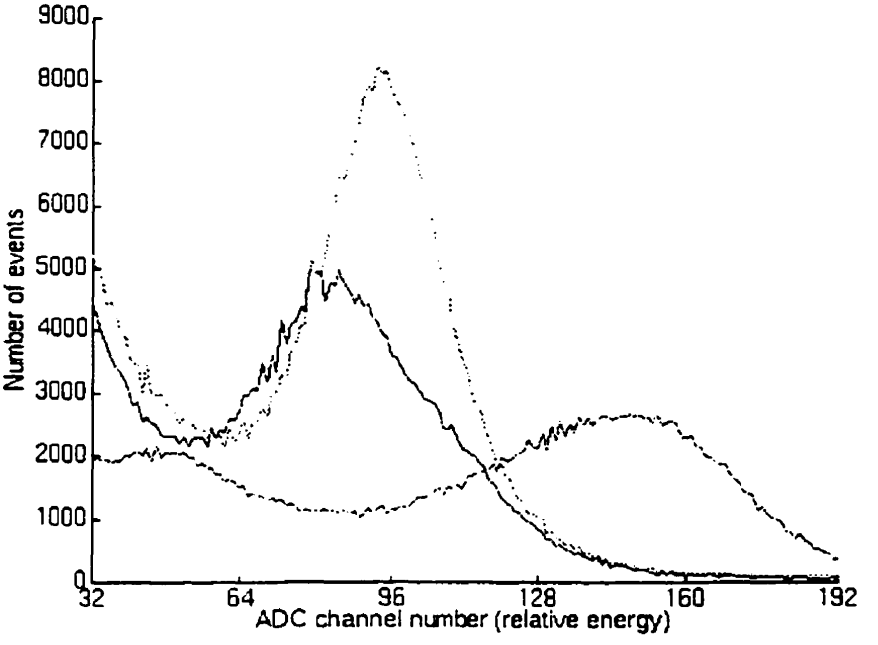

Figure 3.12. A significant variability in light output between detector blocks was observed.

Spatial Resolution Characteristics

In order to examine the variation of the detector block spatial resolution capabilities with its stage of manufacture, a detector block was optically coupled to each of the two PS-PMTs. Each block was wrapped in several layers of Teflon tape and positioned at the centre of the PS-PMT window using optical grease. These detectors were oriented 180° apart so that they faced each other, with the distal crystal faces separated by 10 cm. Two very small point sources, consisting of 1μCi ^{68}Ge deposited on nickel disks, were separated by 10 mm and placed at the midpoint of the detectors. Coincidence data were acquired using an energy window of approximately 300 to 700 keV, and an image was formed using simple backprojection.

Figure 3.13 shows profiles through the images of the point sources for each stage of crystal manufacture. As expected, the spread of the scintillation light through the uncut crystal volume precludes resolving the two point sources. After cutting the crystals, the FWHM of the profile is 3.22 mm. After polishing the crystal, this FWHM is reduced to 2.61 mm, most likely due to a further reduction in the spreading of light from the element in which it originated by increasing the reflectance of the crystal surface. The FWHM of the potted block is 2.05 mm.

Note that these data were acquired prior to developing distortion LUTs. This introduces two consequences which prevent the spatial resolution of the PEM detector from reaching its optimal value : i) detector spatial nonlinearities are inherent in the (x,y) positions used to calculate the lines of response and ii) without using crystal element identification, no determination of whether the event occurred in the proximal or distal matrix of crystal elements was made, so that the DOI-resolving capacity of the detector block is not used.

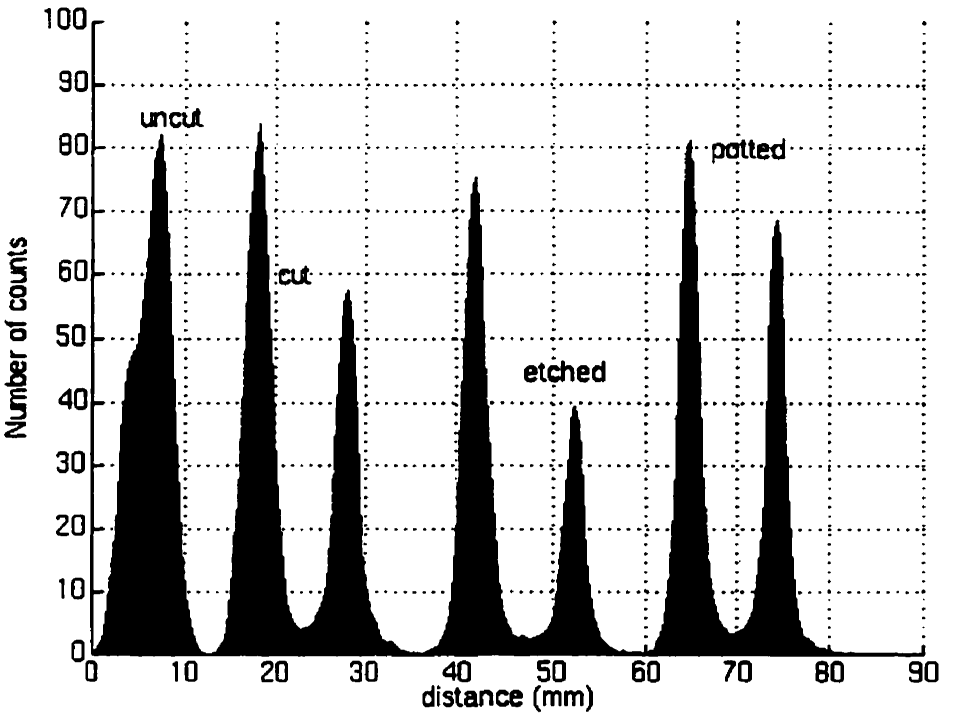

Figure 3.13. Profiles of two point sources placed 10 mm apart, imaged by blocks at each of the stages of manufacture.

4. Methods for generating Look-Up-Tables

4.1. The use of Look-Up-Tables in PET and PEM

Although the detectors constructed for PEM facilitate the required high spatial-resolution and efficiency, their response to incident gamma radiation deviates from "ideal behaviour" in several respects. As is the case for most PET detectors, positioning and energy signals cannot be used directly to perform energy discrimination and image formation. Instead these signals first must be corrected for several particular types of nonlinearities inherent in the detectors. In particular, corrections must be applied to account for the following three main detector characteristics:

i) a marked spatial distortion, particularly near the detector periphery;
ii) a spatial variation in energy response; and
iii) spatial variations in detector efficiency.

Because these aspects of the detector performance arise from properties of the PS-PMTs and the crystal block detectors used, they are considered permanent in that they cannot be eliminated through simple adjustment of the detector hardware or the associated data acquisition electronics. It is possible, however, to detect and to quantify these spatial variations and to subsequently apply an appropriate compensation at the time of data acquisition. This chapter addresses some of the known sources of these specific deviations from ideal detector performance in general, and then discusses the specific calibration methods developed for the PEM system for their correction.

Data describing the observed spatial nonlinearities, spatial variations of detector gain, and variations of detector efficiency are stored in Look-Up-Tables (LUTs). LUTs are used

commonly in conventional PET scanners, and are implemented either in hardware as a series of discriminator settings, or are stored in software as a matrix. They provide a method of applying corrections to the acquired data on an event-by-event basis, at run-time during the course of a scan. Recall that the positioning signal pairs for both detectors, (X_a, Y_a), and (X_b, Y_b), are calculated using the output signals from the PS-PMT Anger readouts (see Figure 25). For detector *a*, for example:

$$X_a = \frac{(x_a^+) - (x_a^-)}{\Sigma_a}$$
$$Y_a = \frac{(y_a^+) - (y_a^-)}{\Sigma_a} \qquad (4.1) \ ,$$

where the energy signal is

$$\Sigma_a = (x_a^+) + (x_a^-) + (y_a^+) + (y_a^-) \qquad (4.2) \ .$$

After the X, Y and Σ signals for each detector are first digitzed by the Aurora ADC, subsequent data processing and LUT access is handled in software, as illustrated in Figure 4.1.

The positioning signals are first normalized by the energy signals, and then are used as indices into (256x 256) distortion table matrices for each detector. The distortion LUT maps the digitized raw coordinates of the coincident events, in ADC channels, to the coordinates of the corresponding crystal elements, (Cx_a, Cy_a) and (Cx_b , Cy_b) in which the events were most likely to have occurred. This mapping to crystal coordinates also removes spatial distortion. The crystal coordinates subsequently facilitate the access of the appropriate energy and efficiency corrections, which are both made on a crystal element-by-element basis. Using the (72 x 72) energy LUT, the keV/ADC channel conversion factors corresponding to elements (Cx_a, Cy_a) and (Cx_b ,Cy_b) are determined, and the event energies, Σ_a , and Σ_b in ADC channels, are converted to keV.

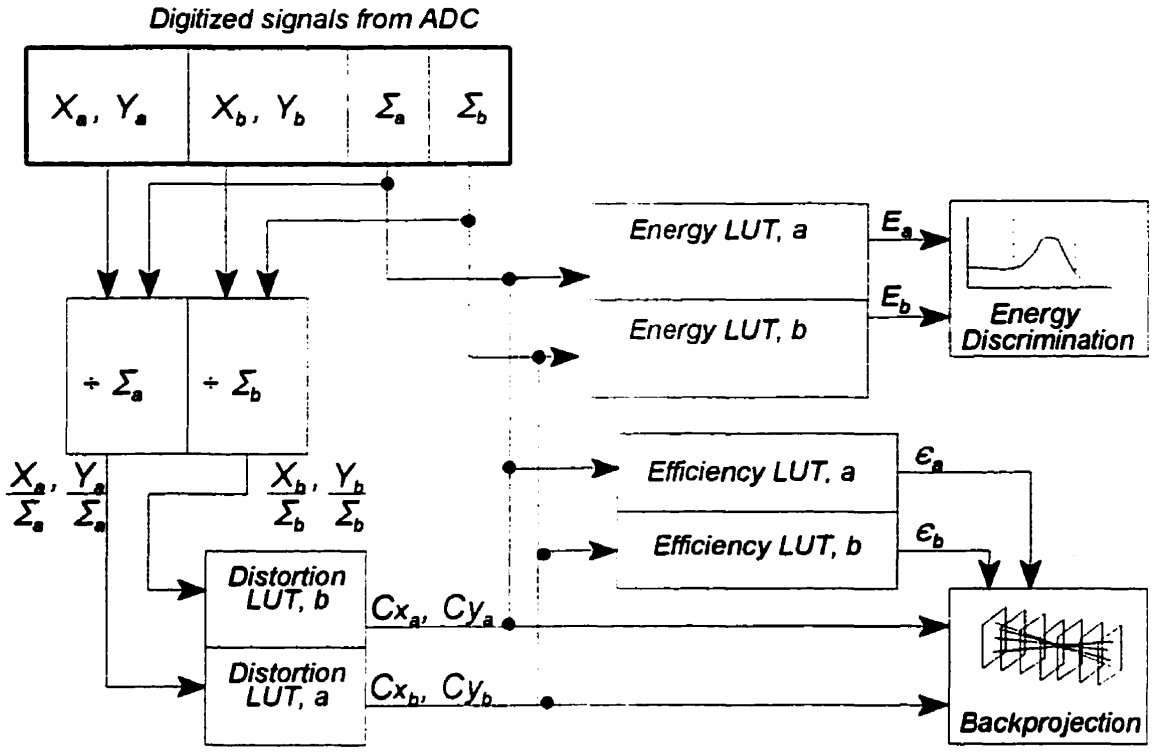

Figure 4.1. Three separate LUTs are accessed for each detector for the correction of spatial distortion, and spatial variation of gain and efficiency.

This then permits the windowing of acquired data using absolute units of energy, while compensating for the variation of gain between elements. If the energies of the coincident

events are within the specified window, the relative efficiencies (ϵ_a and ϵ_b) of the two crystal elements (Cx_a, Cy_a) and (Cx_b, Cy_b) are then returned using the (72 x 72) efficiency LUT. These efficiencies, along with the distortion-corrected crystal locations, are used to set the relative weight of the event during its backprojection, and the online display is updated.

In generating the distortion, efficiency and energy corrections for PEM, the challenge exists not in accessing the LUTs on-the-fly, but rather, in the accurate determination of their contents. It was also important to develop methods so that they are robust, stable and consistent when repeated. The calibration procedure must be sufficiently practical so that it may be repeated periodically as part of a routine quality assurance of the PEM system. In addition, the LUT-generation procedure must be repeated following any intentional modification to the system affecting the data acquired, such as a significant change in the PMT high-voltage supply, in the gain of the X, Y or energy amplification, or a replacement of detector blocks on the PMT face.

4.2. Detector spatial distortion and crystal identification

Detector spatial distortion and its correction in PET

The majority of commercial PET scanners employ detector block designs which involve coupling many discrete crystal elements, often in a modular detector block to one or more photomultiplier tubes. In order to decode the crystal element in which a gamma ray interacted, a decoding scheme is used, based on the premise that each crystal element gives rise to a different distribution of scintillation light over the PMTs. As an example, a current and commercially-used detector is the ECAT HR PLUS block, composed of a single 8 x 8 matrix of pseudo-discrete 4.39 x 4.05 mm crystal elements. The PMTs are arranged in a 2 x 2 matrix as shown in Figure 4.2, and the *x*- and *y*- positions are calculated from the four PMT signals by computing[82,83]

$$x = \frac{(A+C)-(B+D)}{A+B+C+D}$$
$$y = \frac{(A+B)-(C+D)}{A+B+C+D} \qquad (4.3)$$

where A, B, C and D are the amplitudes of signals from the corresponding PMTs following the absorption of a gamma ray in the vicinity of coordinates (x,y). A number of events occurring in a single crystal element give rise to a distribution of (x,y) signals that are characteristic of that element. Therefore, localizing an event to a single element involves specifying boundaries around each distribution in (x,y) signal-space, and then determining to which distribution an acquired (x,y) pair corresponds. If a scintillation occurs in an element and produces N_{AC} photons incident on PMTs A and C, and the mean total number of photons produced is N, then $(N-N_{AC})$ photons will be received by PMTs B and D. The probability distribution resulting from n photons incident on PMTs A and C can be described by the binomial distribution[84,85]:

$$\phi_x(n) = \frac{1}{\sigma\sqrt{2\pi}}\, e^{\frac{-(n-\mu)^2}{2\sigma^2}}$$
where
$$p=\frac{N_{AC}}{N} \qquad (4.4)$$
$$q=1-p$$
$$\mu = N_{AC}$$
$$\sigma = \sqrt{Npq}$$

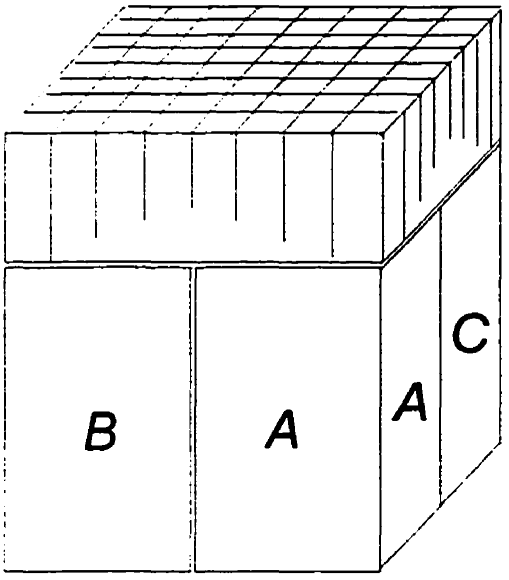

Figure 4.2. A schematic drawing of the HR PLUS detector block, coupled to four PMTs.

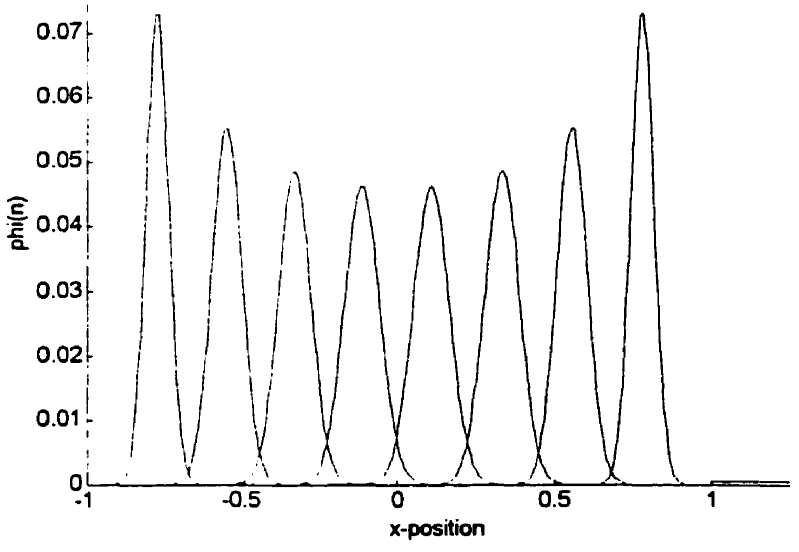

Figure 4.3. The distribution of the x-positions resulting from using a binomial distribution to model the spread of the scintillation photons over four PMTs.

An example of these distributions, calculated for N=200, is shown in Figure 4.3. This model

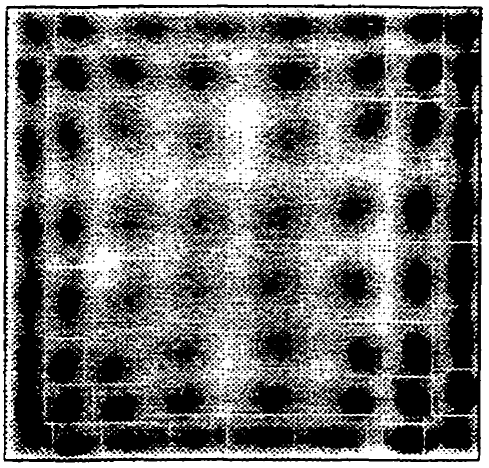

Figure 4.4. The acquired image resulting from flood-irradiating one detector block of the CTI ECAT scanner. The white lines define the regions allocated to separate crystal elements.

suggests that the centres of the distributions from each element in the array will be separated in regular intervals. Several critical features of the block/PMT combination are not accounted for in this model, however, including the variation in light output between elements, variation in photocathode sensitivity, and the presence of intercrystal scatter of the incident gamma ray.

A more realistic position map (shown for both dimensions) is shown in Figure 4.4. This image was produced by flood-irradiating one of the detectors of the CTI ECAT scanner (at the Montreal Neurological Institute) and illustrates the presence of detector spatial nonlinearity, particularly evident in the decrease in the detected intercrystal-spacing near the periphery. While the source of this distortion is inherent in the hardware, the computed locations of the elements are easily distinguished, and the physical locations of the crystal elements are known. By delineating boundaries around each of the visible crystal elements as shown, each raw (x,y) event may be mapped to one of the crystals of the detector block. This process, termed *crystal identification*, is repeated for all of the crystal blocks during the

scanner's calibration routine.

Several methods of crystal identification have been investigated[85, 86, 87, 88] and are schematically illustrated below. Figure 4.5a) illustrates a method whereby x- and y- thresholds are set at the valley positions for each vertical column and horizontal row of crystal elements, respectively. The method shown in b) involves setting a y-threshold for each of the row valleys and using x-thresholds specific to the y-location of the event. In c), "island" regions of interest (ROIs) are drawn around each of the crystal elements in the image. Dahlbom and Hoffman[85] have reported that for a 4x8 BGO array coupled to four 2.5 cm x 2.5 cm PMTs,

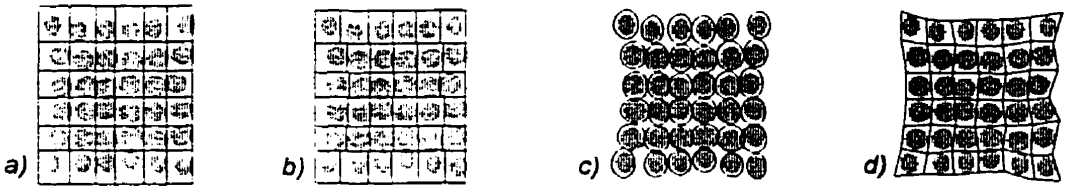

Figure 4.5. Several techniques of crystal identification have been examined previously, including specifying common row/column borders, row-dependent column borders, drawing islands, and using 4-sided polygons.

the ROI scheme results in an improvement in resolution of about 5% compared to that for methods a) and b). Because all events falling outside of the ROIs are discarded, however, 15% of the counts are lost. This reduction of efficiency is avoided with method d), whereby a 4-sided polygon defines each crystal element region. It should be noted that while methods a) and b) events can be mapped to crystal elements using hardware x- and y-signal discriminator settings, methods c) and d) requires the use of a LUT stored either in firmware or in random access memory to be referenced on an event-by-event basis.

4.3. Spatial distortion and crystal identification for the PEM detectors

While several methods of generating distortion LUTs for PET have been established, the task of generating a distortion LUT for the PEM system differs in several respects. First, while the number of crystal elements to be identified for a PET detector is on the order of 8 x 8, one PEM detector requires the identification of, optimally, 72 x 72 regions. Second, the design

of the BGO block differs significantly, with two layers of crystal elements joined by a 2 mm uncut thickness of crystal. This is a geometry which may decrease the Peak-to-Valley-Ratio (PVR) because of increased intercrystal scattering of annihilation photons and spreading of light through the uncut region from the point of the interaction to neighbouring crystal elements. Third, while most detectors developed for PET applications have used standard single or dual PMTs, PEM employs position-sensitive PMTs. PS-PMTs are far better suited to a crystal block with a high packing fraction of crystal elements, but several characteristics of these devices give rise to spatial nonlinearity, resulting in image distortion. The most critical source of spatial nonlinearity is also that which is best understood, and produces a pronounced compression of events occurring at the periphery of the PMT photocathode. In this region, for a given spatial shift in the position of the incident scintillation light, the corresponding change in the positioning (x or y)-signal amplitude is markedly decreased, as

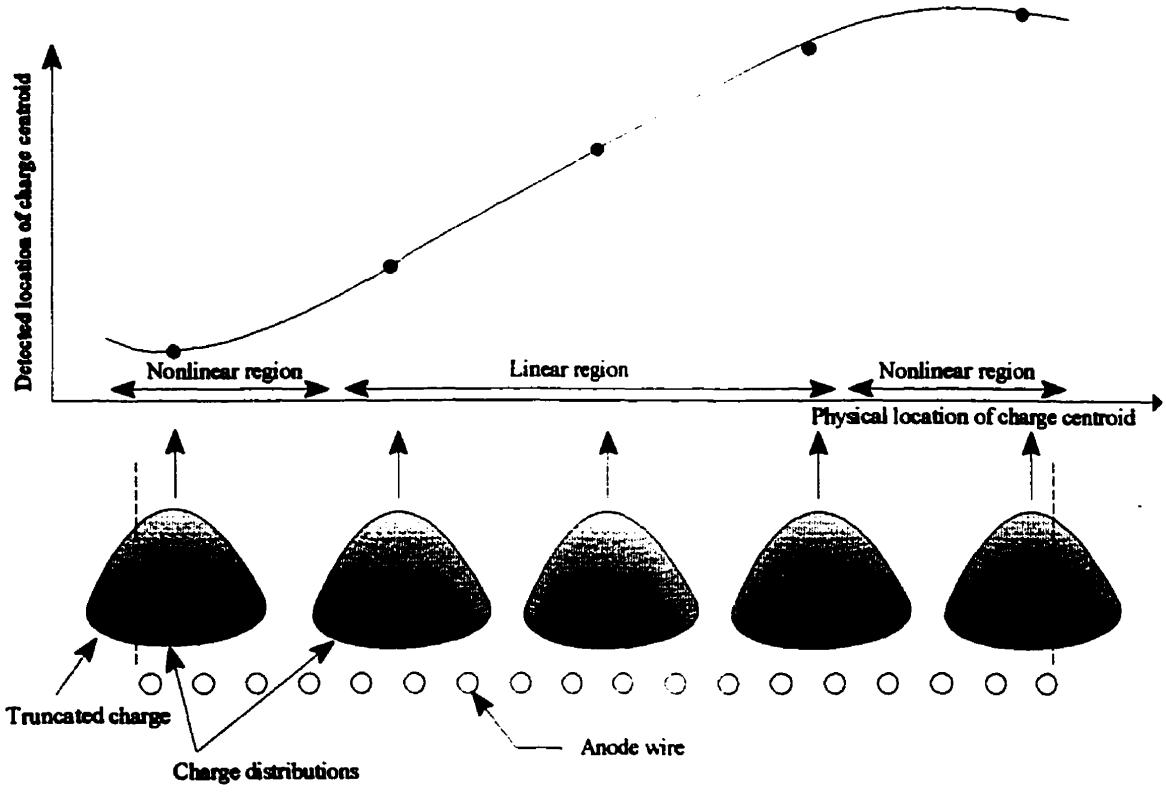

Figure 4.6. Spatial nonlinearities are caused by the truncation of the electron charge distribution at the edges of the multiwire anode of the PS-PMT. When the charge extends beyond the last wire of the anode, the centroid of the actual (physical) distribution is detected to be too close to the centre of the PMT.

compared to that for the central region. The data provided by the manufacturer[89] indicate that the positioning signals become multi-valued in the extreme periphery. This suggests that without employing a sophisticated technique involving, for example, multiple-energy-window discrimination or reading out individual wire signals, the Useful-Field-Of-View (UFOV) will be smaller than the physical area of the photocathode.

Figure 4.6 illustrates the source of this spatial nonlinearity at the periphery. If an event occurs at a location sufficiently close to the PS-PMT edge (in either the x- or y-dimension), the resultant charge distribution is truncated beyond the edge of the mesh of anode wires. The Anger-type readout then returns the centroid of an asymmetric charge distribution. Consequently, the physical centroid of the charge is located further towards the PS-PMT periphery than is suggested by the erroneous positioning signal. The effect of this nonlinearity may be observed in an image indicating the locations of the PEM crystal elements themselves, analogous to that shown in Figure 4.4. The result is a distortion whereby the separation of events detected from two adjacent crystal elements decreases towards the periphery of the PMT until separate elements are not distinguished. The dimensions of the identifiable region of the detector dictate the size of the scanner's UFOV. Events occurring at the very edge of the PS-PMT result in positioning signals which, in a spatial sense, simply "pile-up".

In addition to this spatial distortion at the periphery, there are less drastic, yet readily apparent and irregular nonlinearities *throughout* the UFOV of the device, even close to the PS-PMT centre. By examining crystal-identification images obtained by using four separate R3941 PS-PMTs and the same detector blocks, it appears that the location and nature of these distortions vary according to the particular PS-PMT used. This variability between devices is confirmed by the manufacturer's specifications of linearity in the central region of the PMT. Considering that each PS-PMT has been built by hand, it is possible that these distortions result simply from manufacturing irregularities. Both the nonlinearities close to the centre and at the periphery necessitate the use of a distortion LUT.

Technique for generating the spatial distortion Look-Up-Table for PEM

To correct for the inherent spatial distortions described above, it is necessary to determine an accurate and complete mapping between the detected (x,y) locations of gamma-ray interactions (in ADC channels) and their corresponding true physical locations (in crystal coordinates).

Conceivably, this map could be determined by using a two-dimensional translation stage to scan a narrowly-collimated gamma-ray source across the field of view of the detector. In this manner, the detected positions of the events recorded for each position of the source would be used to generate a distortion LUT. Such a method, however, suffers from several drawbacks. First, if 511 keV gamma rays are to be used, it would be a challenge to collimate the source to allow the irradiation of a single ~2mm^2 crystal region. Second, the narrow collimation of the source would produce a low count rate, increasing the amount of time required for the procedure. Finally, the translation stage required would increase both the cost and overall complexity of the system. To avoid these complications, a technique of crystal identification has been developed, based on the methods used for the smaller crystal arrays in PET detectors. The method, however, differs in that it has been developed to cope with the identification of a very *large number* of closely-spaced crystal element regions. The technique involves two main steps:

i) acquiring the data required to form an image in which the individual crystal elements are visible, and

ii) running the LUT-generation software to perform crystal identification.

Acquisition of data for the crystal identification image

In order to generate the crystal identification image, data is acquired in singles mode while irradiating the crystal block using a 5μCi ^{68}Ge-^{68}Ga ($t_{1/2}$=278 d) PET transmission rod source. Typically, 2x10^6 events are collected in list-mode, so that energy-windowing of events may be performed subsequently during the analysis of the image. Initially a flood irradiation was

used to generate this image (similar to that used for PET). However, the crystal elements visible in the flood-image were not easily separated in many regions of the field-of-view (this was not surprising, since the FWHM of the distribution of counts from a single element would have to be ~1.4mm in order to separate elements that are diagonally-adjacent). To improve the accuracy of locating the apparent positions of crystal elements, the PEM detector blocks are irradiated from the side as shown in Figure 4.7 . This setup is arranged easily by removing the detectors from the magnification table and by aligning the lead shielding with fiducial marks located on the side of the detector housing. The fiducial marks correspond to 4mm-wide gaps cut in the lead shielding surrounding the detector blocks. In this arrangement, the incident gamma-rays are confined to the proximal crystal elements (those coupled directly to the PS-PMT) by the lead blocks positioned outside of the detector, and by the lead shielding mounted within the housing next to the detector blocks. Thus, except for those resulting

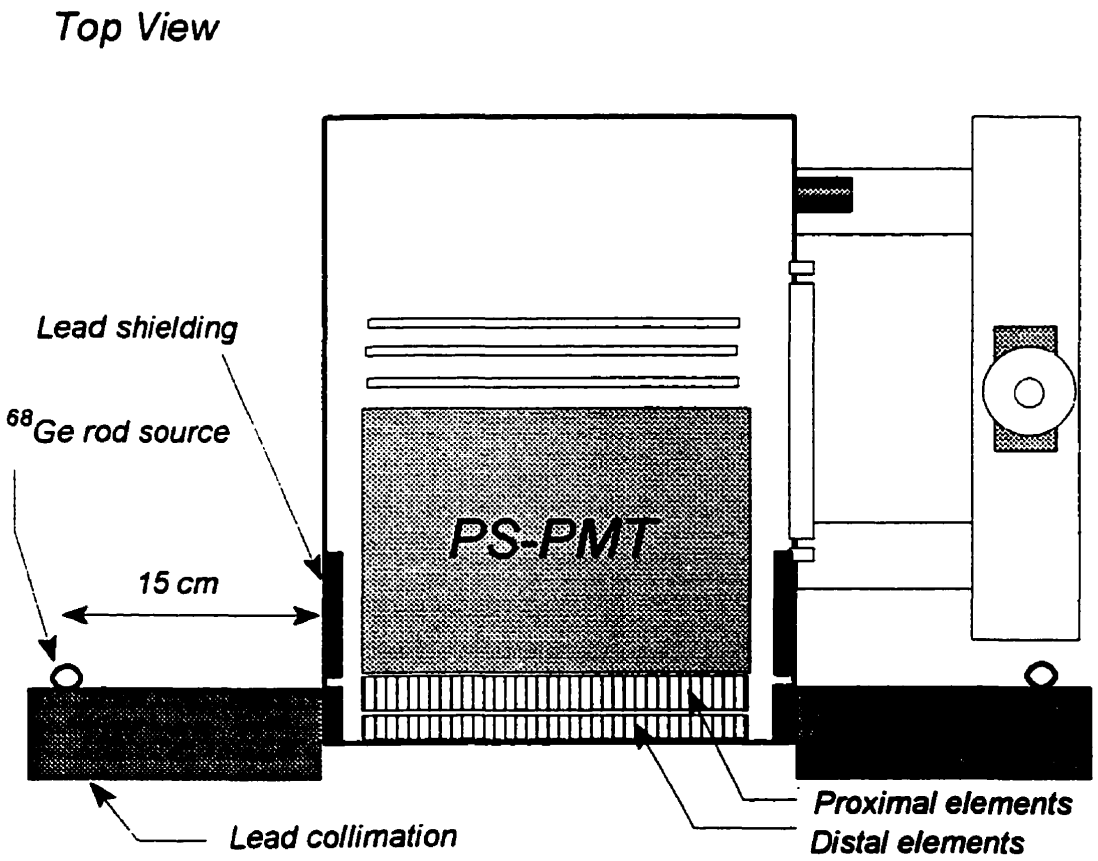

Figure 4.7. Two ^{68}Ge rod sources are aligned to irradiate the proximal elements of the crystal block.

from gamma rays scattered into the uncut crystal region and into the distal crystal elements, the majority of interactions will occur in the proximal crystal elements. This method produces an image in which the proximal crystal elements are readily distinguishable. Although maxima corresponding to the distal elements are not apparent in the image, the location of these elements can be determined relative to the identified proximal elements. Within a tolerance of approximately ±0.1mm in both the x- and y-directions, it is known that a distal element is located in the centre of every 2-by-2 group of proximal elements.

Image preprocessing and performing the crystal identification

After the side-irradiation data has been acquired for both detectors, the distortion LUT generation proceeds in four steps:

i) a suitable crystal identification image is generated after imposing multiple-energy-window criteria;
ii) the image is filtered;
ii) the crystal identification software is run; and
iii) a binary distortion LUT, to be accessed at run-time, is written.

The software written for image processing and for performing the crystal identification has been integrated into a single menu-driven, graphical application. The graphical interface, and image display routines have been written in MATLAB (The Mathworks, Natick, MA, USA) while computationally- and loop-intensive routines have been coded in ANSI C for efficiency.

In order to produce a crystal-identification image in which elements are clearly separated, it was important to eliminate as many events as possible resulting from gamma rays scattered into the crystal from the lead collimation, and those absorbed in the uncut region of the crystal. In addition, induced Pb and Bi x-rays may be detected during singles-counting[90], reducing the separation of the crystal elements. Using a coincidence collimation technique[91] would dramatically reduce the proportion of scattered gamma-rays and x-rays detected, but

it was necessary to develop a calibration technique without necessitating a third PMT. Nevertheless, the number of scatter-events contributing to an image can be reduced by processing a list-file while imposing an energy-window to determine which events are accepted. The crystal light output and the photocathode quantum efficiency both exhibit a marked spatial dependence, however, causing the gain to fluctuate significantly between crystal elements. Consequently, if a single energy window is used in order to eliminate scattered events, while it may improve the separation of some crystal elements in the image, the energy of events occurring in other elements (with higher or lower gain) may fall outside

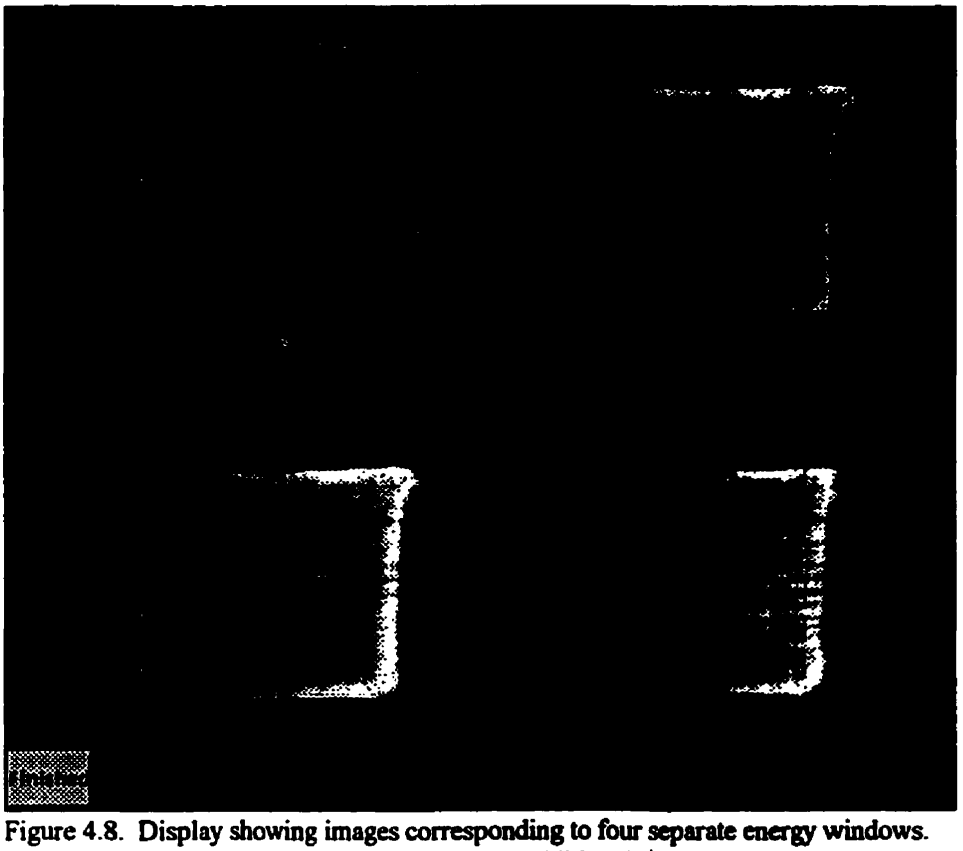

Figure 4.8. Display showing images corresponding to four separate energy windows. From this window (and a second in which three additional images are displayed), the user selects images in which separate crystal elements are well-separated. An summation of the selected images is computed and used subsequently for crystal identification.

of the window, and these events may be inadvertently discarded.

Thus, in order to generate an image in which all elements are clearly distinguished while eliminating much of the effects of scattered radiation, the list file is first processed using seven different energy windows, and an image is generated for each. The user is then presented with a graphical display of the results and chooses a number of images in which well-separated crystal elements are apparent. Figure 4.8 shows the display of four of the energy-windowed images and also illustrates the dependence of the location of visible crystal elements on the energy window chosen. After the user selects all of the useful images, the sum of the selected images is computed and is used for crystal identification.

Although the method of side-irradiating of the crystal block is useful for improving the separation of the elements visible in the image, the effect of the attenuation of the gamma rays from the side of the block towards the centre is apparent in the image. The modulation due to individual crystal elements is visible with respect to an average offset of pixel value that decreases exponentially from the edge of the block towards the centre. In order to simultaneously remove this low-spatial-frequency offset, and to remove high-frequency noise from the image, a suitable two-dimensional FIR bandpass filter (Figure 4.9) is used. This filter was designed using Blackman-window profile[92], with the peak centred on the average spatial frequency of the modulation crystal elements in the image. The lower and upper cut-off frequencies used were 0.10 and 0.55 mm^{-1}. Key features of the filter are a real frequency response:

$$H(\omega_x, \omega_y) = H^*(\omega_x, \omega_y) \qquad (4.5)$$

and an impulse response that is symmetric about the origin:

$$h(x, y) = h^*(x, y) \qquad (4.6).$$

These characteristics ensure a zero-phase response[93], preventing the introduction of frequency-dependent phase distortions into the filtered image.

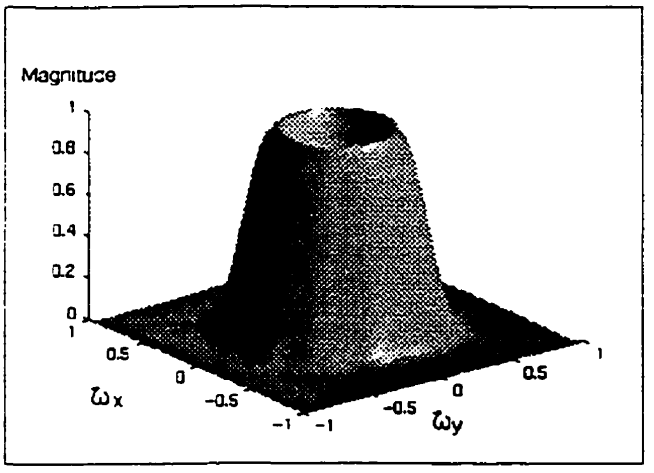

Figure 4.9. The FIR filter designed to remove both the low-frequency offset resulting from side-irradiation and high-frequency noise.

Following these preprocessing steps, the image is available as input to the crystal identification software. The crystal identification proceeds in two steps:

i) using a graphical user interface, the user locates several points along the "valley" regions between adjacent rows or columns of crystal elements, and

ii) these initial guesses are then used as input in order to find minima between adjacent elements.

Figure 4.10 shows an example of the interface used to locate valley positions, after the task of initially locating the valleys between adjacent elements has been completed. By using the mouse, two or more points are located between adjacent crystal elements rows or columns.

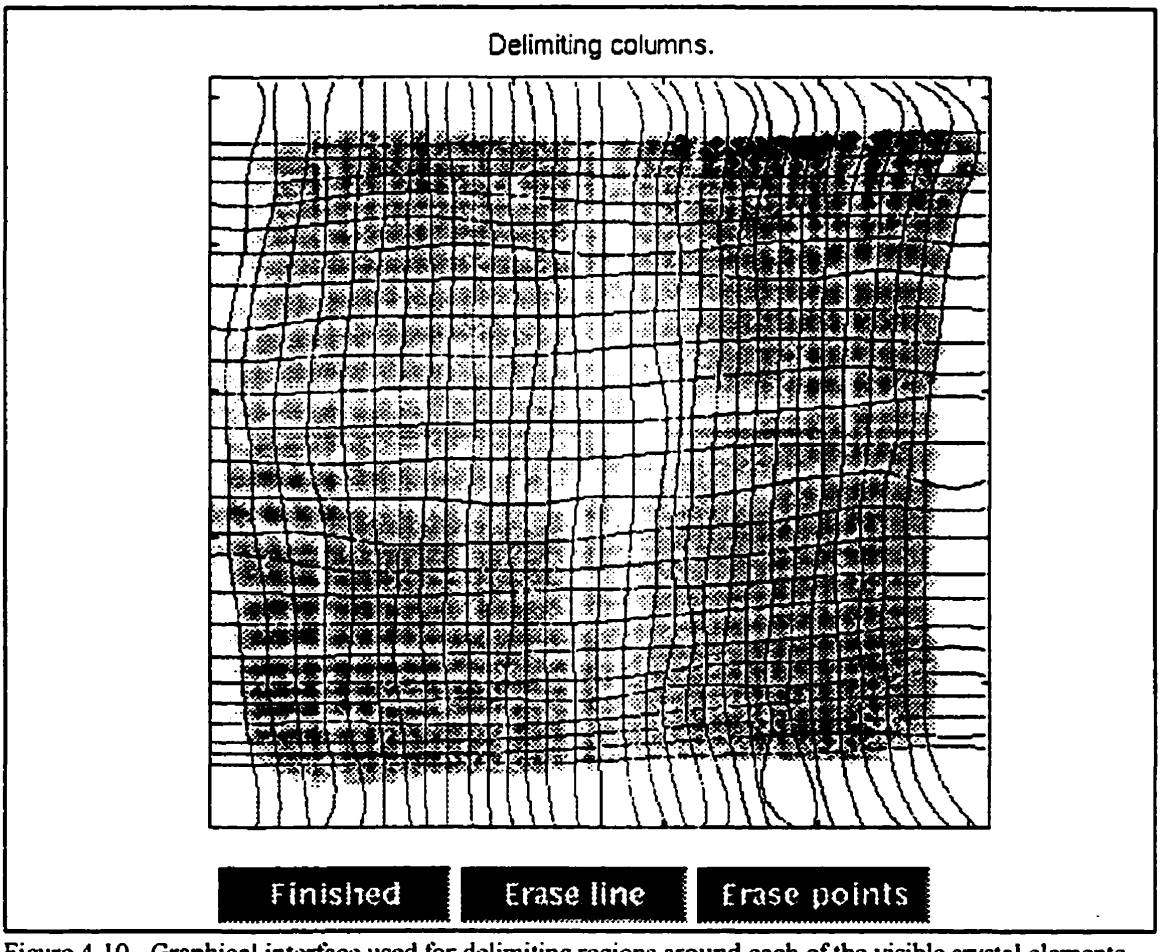

Figure 4.10. Graphical interface used for delimiting regions around each of the visible crystal elements.

A cubic-spline interpolated line consisting of piecewise polynomials[94] is then computed to follow the valley very closely (a complete set of these lines is shown in the figure). While locating points, the user may also produce an x- or y-profile for visualizing variations in pixel value not apparent from changes in image intensity. The placement of several points in each of the visible horizontal and vertical valleys requires approximately ten minutes for each of

the two detectors. While this step involves a considerable amount of interaction by the user, the remainder of the process is automated.

A small section of a crystal identification image is shown in Figure 4.11 to illustrate the algorithm used to relocate these initial guesses of the crystal element positions. After the horizontal and vertical spline-interpolated lines (a) have been drawn, their intersection points are located (b). Each point is then allowed to "wander" within a circular region of radius equal to half of the average crystal separation in pixels, using a 3 x 3 smoothing kernel to reposition itself in a local minimum (c). The midpoints between adjacent local minima positions are then located, and used as vertices in order to draw 4-sided polygons. As shown, this process specifies boundaries around each of the proximal elements, and also specifies regions between each 2 x 2 group for the distal crystal elements on the opposite face of the block. Once all of the regions have been located, the user then selects one region corresponding to a known crystal element (an element at the corner of a block, or a missing element is often used), and enters its absolute coordinates. This final step of the procedure serves to link every (x,y) pair contained within identified regions to the absolute crystal coordinates. Any (x,y) pairs outside of the identified regions are assigned coordinates of (0,0) indicating that events in these areas should be ignored. For each detector, two (256x256) integer matrices containing the x- and y- crystal coordinates are written to binary LUT files.

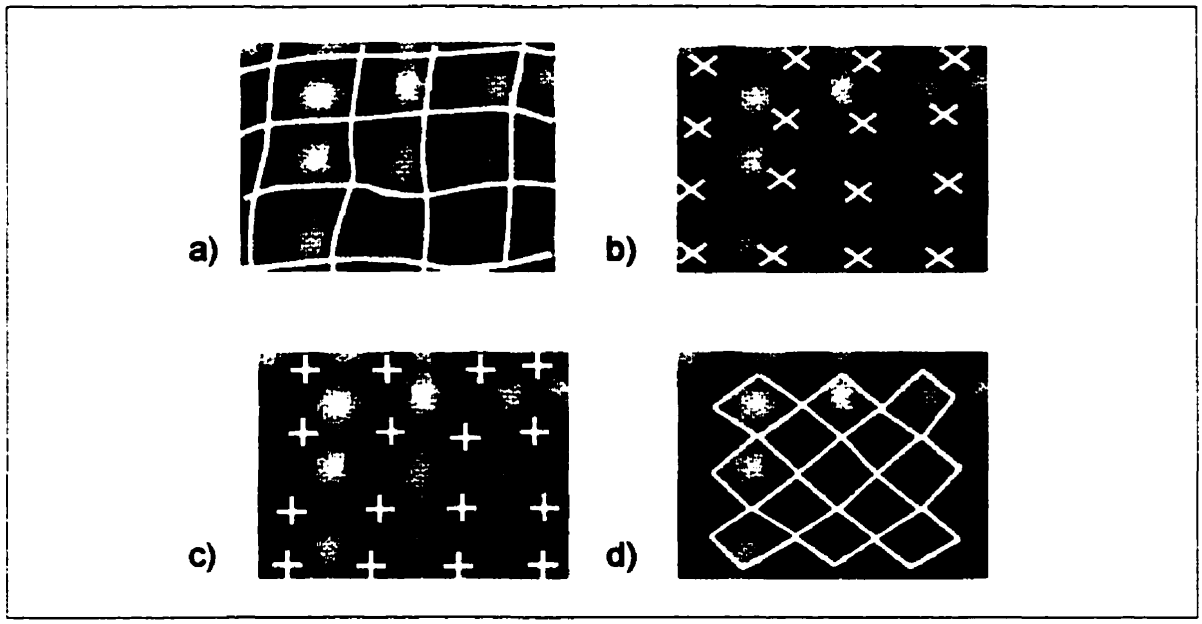

Figure 4.11. After spline-interpolated lines have been computed (a), the intersection points are located (b), and allowed to wander to local minima (c). The midpoint between the adjacent minima are located and used as vertices to draw 4-sided polygons (d).

4.4. Spatial variation of detector efficiency

Detector efficiency and its spatial variation in the PEM system

The *efficiency* of a detector refers to the fraction of the incident gamma rays that are detected and which produce useful signals for image formation. There are several factors contributing the overall system efficiency, including[95]

- The detector's *geometric efficiency*, $\epsilon_{geometric}$, which is a measure of the fraction of emitted photons that are incident upon the detector. This is determined by the detector surface area, a, presented to the incident gamma rays, and the distance between the source and the detector, r;
- The *intrinsic efficiency* of the detector, $\epsilon_{intrinsic}$, which refers to the fraction of incident

photons that are subsequently absorbed. This is determined by the depth d, of the crystal elements and the linear attenuation coefficient, μ, of the crystal for 511 keV gamma rays;

- $\epsilon_{self\text{-}absorb}$, which is the scatter and absorption of gamma rays by the material between the source and the detector (i.e. the FDG in the breast and tumour tissue); and
- $\epsilon_{accepted}$, the fraction of detected events that are accepted and recorded by the imaging system. In particular, if energy discrimination is to be performed during acquisition in order to reject events resulting from Compton-scattering or pulse-pileup, this contribution to the total efficiency would be < 1.

The total efficiency, then, is equal to the product of these terms, where each is in the range of [0,1]:

$$\epsilon = \epsilon_{geometric}\, \epsilon_{intrinsic}\, \epsilon_{self\text{-}absorb}\, \epsilon_{accepted},$$

where

$$\epsilon_{geometric} = \frac{a}{4\pi r^2} \qquad \text{and}$$

$$\epsilon_{intrinsic} = 1 - e^{-\mu_1 d} \quad .$$

In quantifying variations of efficiency of the PEM detectors on a crystal element-by-element basis, $\epsilon_{self\text{-}absorb}$ is kept quite uniform by using a very uniform flood-source. Similarly, $\epsilon_{accepted}$ is removed from the possible sources of variability accepting all incident events. The geometric efficiency may vary slightly between elements, however, due to a some discrepancy in the area of the nominally 1.9 mm x 1.9 mm crystal elements. Since the saw used to cut the crystal blocks provides a tolerance of ±0.1mm, the maximal variation of the crystal area and thus the geometric efficiency is approximately 10%. Another factor leading to variations in efficiency is the presence of defects in the crystal caused either during cutting or during etching. During these stages of manufacture, for some of the blocks produced, several elements were broken and became separated from the block entirely, reducing the efficiency

of those elements to zero. It is also possible that hairline cracks may have been introduced in a few elements resulting from the stresses involved during cutting or from the vibration used during the acid etching. This may prevent the transmission of scintillation photons from the point of interaction to the photocathode.

Method for generating the efficiency Look-Up-Table

Because the effect of the exponential attenuation of gamma rays from the side of the crystal block is predominant in the side-irradiation data, this data is not suitable for the assessment of the relative efficiencies of detector elements. The ^{68}Ge-^{68}Ga rod source is therefore positioned at a distance of 1 m from the detector face, in order to approximate a flood-source. $5x10^6$ singles events are acquired with this arrangement and are stored in a list file.

In order to generate the efficiency LUT, the flood list file is processed with reference to the previously-generated distortion LUTs. For each event contained in the list file, the raw (X, Y) coordinates (in ADC channels) are used as indices into the distortion LUT, and the corresponding crystal coordinates, (Cx, Cy) are returned. The element of a 72 x 72 efficiency matrix with indices (Cx, Cy) is then incremented. After repeating this procedure for the entire list file, the efficiency table is normalized to its maximum.

4.5. Spatial variation of detector energy response

Variation of energy response in the PEM detectors

The energy of an event is the amplitude of the signal determined by summing the X-, X+, Y- and Y+ signals using an analog summing amplifier. Once digitized, this information is used both for the correct positioning of the event and, if selected in the PEM software, for energy discrimination in order to reject scattered coincident events. Between the absorption of the gamma ray by the crystal and the ultimate detection of the corresponding electronic signal produced, several stages will affect the amplitude of the energy signal. Moreover, this

amplitude varies spatially, ultimately resulting in a crystal-element dependent variation of the detected amplitude of the energy signal per keV of gamma ray energy absorbed. For this discussion, the energy signal produced (in volts) per keV of gamma ray energy deposited will be referred to as the *gain*.

As described previously, while the number of scintillation photons produced per unit energy absorbed is a characteristic of the crystal (for BGO it is approximately[96] 8 photons/keV), the light output from the crystal depends strongly upon the geometry and surface preparation. As indicated by the energy spectra illustrated earlier, and as reported by other investigators[97,98], the light output depends greatly on the crystal surface finish and the reflector surrounding the crystal faces. For the PEM detector blocks, it is the nonuniformity in surface finish between crystal elements that is the most significant cause of the spatial variation in light output. Although the surfaces of all crystal elements were rough after cutting, the coarseness of the surface varied from element to element. Subsequently, during the etching process, while an effort was made to produce a continuous flow of acid through the saw cuts, it was observed (by comparing lost fragments) that the quality of the polish produced varied somewhat.

The result of this nonuniformity in surface finish is a situation in which the location of the photopeak (in ADC channels) will depend on the crystal in which the scintillation light was produced. The Energy LUT contains the photopeak locations for each of the identified elements, allowing energy windows to be specified in keV.

Method for generating the energy Look-Up-Table

The energy and efficiency tables are generated during a single reading of the flood-irradiation list file. As for the efficiency LUT, the crystal coordinates (C_x, C_y) corresponding to a given raw positioning signal (x,y) pair are determined using the distortion LUT generated previously. The energy E of this event is also read from the list file, and the element of a 72 x 72 x 256 matrix specified by the indices $[C_y][C_y][E]$ is incremented. By repeating this

procedure for each of the events in the file, an energy spectrum for each of the identified crystal elements is compiled. Because the fraction of the total number of counts in the flood list file contributing to the energy histogram of a single element is quite small, it was necessary to smooth each of the histograms using a moving-window averaging method[99] before locating the photopeak maximum. Specifically, the smoothed energy spectrum, E' was computed using an averaging window of width W, using

$$E_i' = \frac{1}{W} \sum_{n=-W/2}^{n=W/2} E_n \qquad (4.9)$$

This smoothing facilitates the correct location of the centre of the photopeak, without incorrectly assigning the peak ADC channel to that of a local maximum resulting from noise. The photopeak of a smoothed spectrum is identified by stepping through the spectrum from channel 256 to channel 20, and computing the slope for 10-channel wide segments. The centre of the photopeak corresponds to the channel at which the slope crosses zero. This channel is stored as a byte in element $[C_y][C_y]$ of the binary Energy LUT.

5. Results

5.1. The Distortion Look-Up-Tables

Figure 5.1 and Figure 5.2 illustrate the results of the crystal identification for the two detectors (referred to as detectors "A" and "B") used in the system. The crystal identification images result from side-irradiation of the detector blocks used for the final PEM system. The eight blocks selected were those which had lost only a few elements during manufacture, most commonly at the block edges. The blocks were oriented, when possible, to position any missing elements at the periphery of the PS-PMT window. As shown in these figures, the side-irradiation technique produces an image in which adjacent proximal crystal elements are well separated. Using the algorithm described in Chapter 4, the 256 x 256 x- and y- ADC channel space has been partitioned into regions for all of the identifiable crystal elements. The overlaid lines in the figures define the boundaries of both the proximal and distal element regions. At most, 59 (in the x-dimension) x 49 (in the y-dimension) crystal element regions have been defined. The aspect ratio of this identifiable region is consistent with the smaller width covered by the 16 anode wires across the y-dimension compared to the 18 wires across the x-dimension.

The reasonable separation of adjacent crystal elements is illustrated in the x- and y-profiles shown in Figure 5.3 and Figure 5.4 respectively. The mean peak-to-valley ratio was 3.8, but a considerable range was encountered, from 1.2 to 18.1.

The crystal identification images reveal the presence of spatial distortions throughout the

fields-of-view of the detectors. Similar images produced using four different PS-PMTs indicate that there are very few similarities in the nature of these distortions between

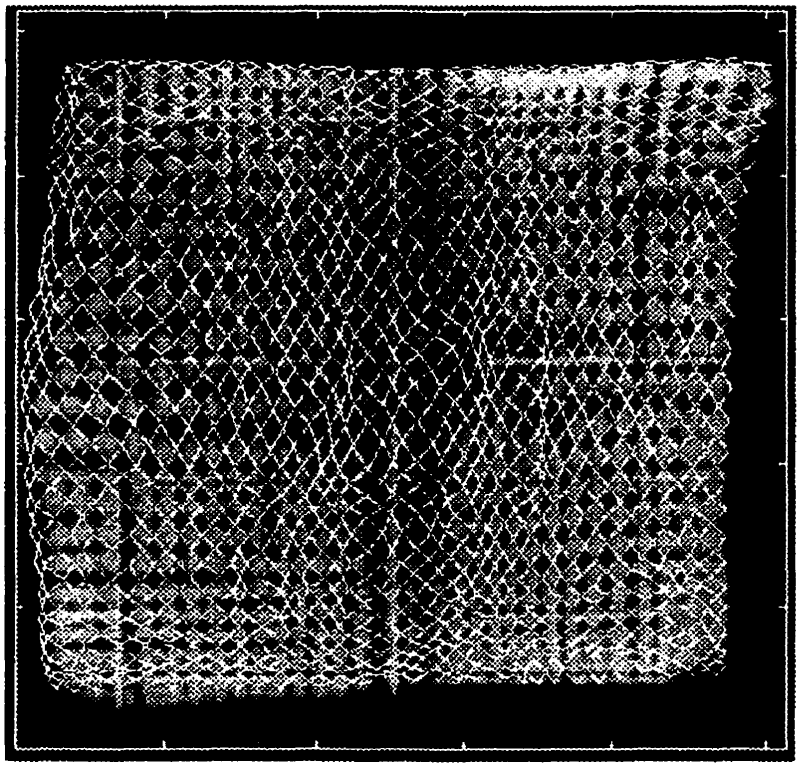

Figure 5.1. The crystal identification region for detector A, with the crystal identification boundaries overlaid.

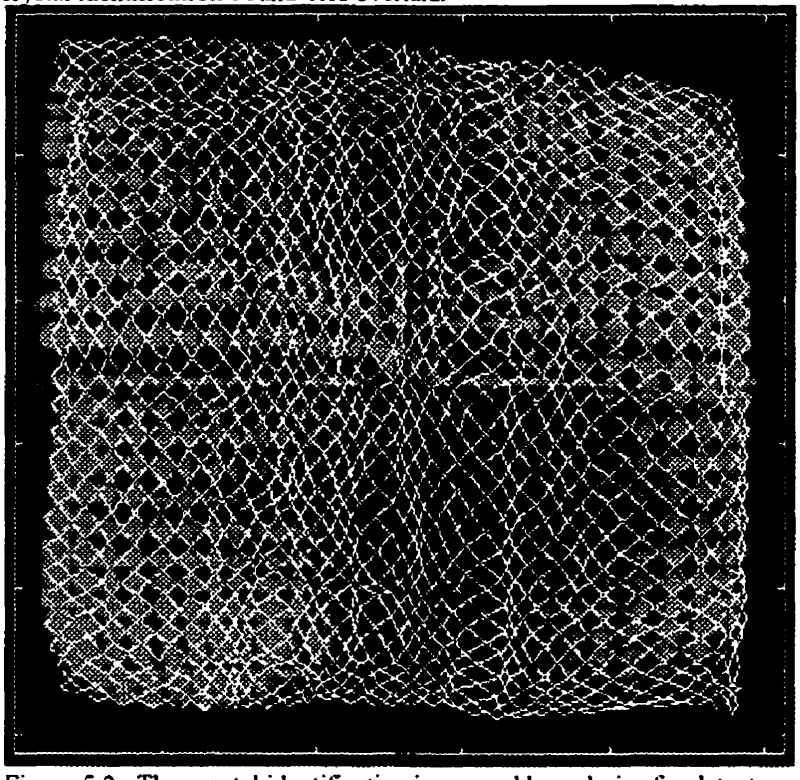

Figure 5.2. The crystal identification image and boundaries for detector B.

detectors. All detectors, however, exhibit charge-truncation nonlinearity at the periphery (described in Chapter 4). The effect of this distortion, which causes the spatial pile-up of events around the detector edge, is visible in the crystal identification images. The crystal identification was extended as close to this peripheral nonlinear region as possible. For this reason, several of the crystal element regions in the rows closest to the edges, while still

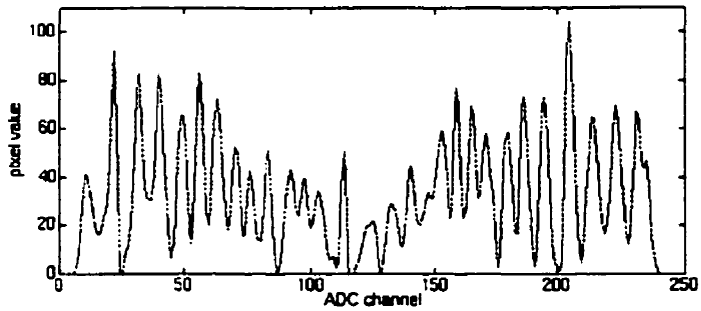

Figure 5.3. A profile through horizontal row of crystal elements in the crystal identification image.

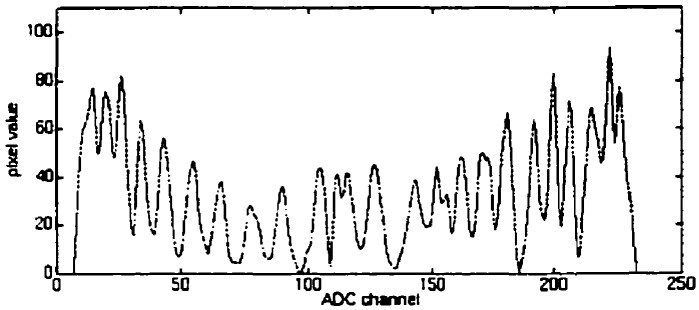

Figure 5.4. A profile through the image of a vertical column of crystal elements.

distinguished, likely receive events from more peripheral regions of the crystal. In addition, the corners of the detector circumference appear rounded, corresponding to an overlap of the nonlinearities at both the x- and y-edges of the anode. Consequently, several rows and columns extend into the corners, beyond the identifiable region. This has little effect in terms of distortion, since these corner regions will receive a comparatively very low number of events.

The identification was complicated somewhat by the presence of ADC differential nonlinearities[100], visible in the images as solid lines across the middle of the x- and y-dimensions. This nuisance causes the events from one ADC channel to be misplaced into the adjacent channel. This did not, however, prevent the determination of the distortion LUT boundaries around the affected regions.

Stability of the distortion Look-Up-Tables

Although the crystal elements are well separated and quite easily identified, it was necessary to address several concerns related to the reproducibility and accuracy of the distortion LUT. Two requirements were tested in particular: i) the stationarity of the crystal identification when generated repeatedly without changing any system parameters; and ii) longer-term stationarity of the distortion LUT during the normal operation of the scanner.

The first requirement was tested by repeating this side-irradiation of the same detector blocks six times, and regenerating the crystal identification for each image produced. The distortion LUTs generated were then compared to detect any relative shifts of crystal element regions. Such a spatial shift could arise from two causes in particular: i) variability in the local-minima finding algorithm; or ii) a drift in the x- and y-positioning signals in the process of turning off the PS-PMT high voltage and preamplifier supplies, then reapplying power. The first of these two possibilities was the major concern, since the starting point of the minima-locating routing is a spline-interpolated line drawn using two or more manually-placed points which will likely vary in location between successive crystal identifications.

In comparing the six distortion LUTs, the standard deviation of the locations of corresponding crystal region corners were computed. The frequency histograms of these standard deviations, for displacement in the x- and y- dimensions, are shown in Figure 5.5. The distance over which the corners of element regions was found to shift is very small in comparison to the size of the regions themselves. Using the crystal element centre-to-centre distance to determine the mm/pixel conversion, the mean standard deviation is 0.1 mm for

both the x- and y-dimensions.

The second criterion, of longer-term stationarity of the crystal identification, was examined just prior to the writing of this chapter. In order to check for any shift of the crystal element regions over the two months that the same distortion LUT has been used, new side-irradiation images were regenerated. The crystal identification was performed using these images, and compared to that generated for the original LUT. On average, the standard deviation of the position of corresponding region corners was less than 0.1 mm, confirming the stability of this LUT.

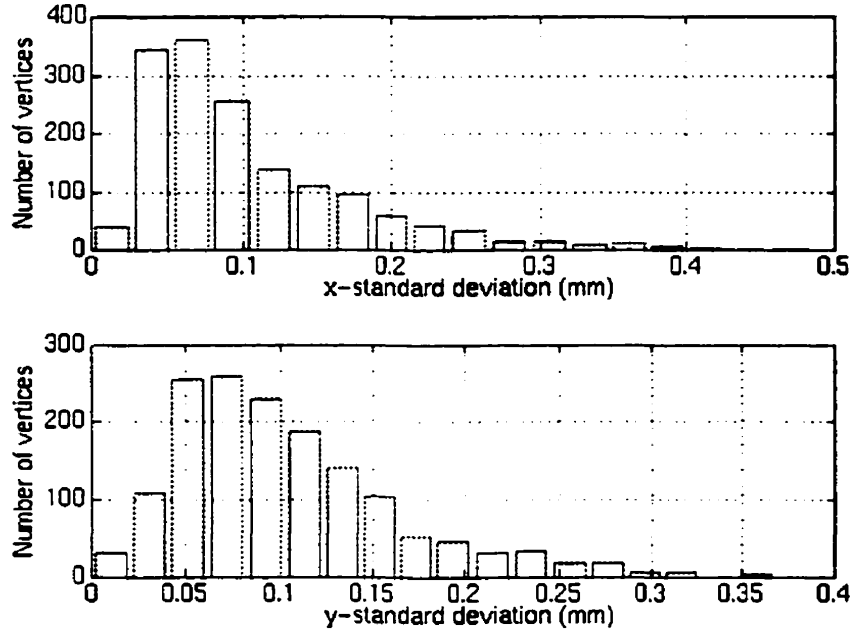

Figure 5.5. The frequency distribution of the standard deviations of corresponding crystal element region vertices.

The effect of drifts of signal gain

For conventional PET detectors, it has been suggested that poor stability of signal gain may have significant consequences in terms of event mis-positioning[101,102]. For the PEM system, if signal gain fluctuations occur, it is anticipated that they would arise from two main sources:

i) drifts in HV PS-PMT supply, or ii) temperature-related drifts in the amplification of the positioning signals. This latter cause is particularly conceivable, since the preamplifiers for the X+, X-, Y+ and Y- signals are housed within the detector boxes, and several operational amplifiers used are quite warm during normal operation. In order to test the dependence of event positioning on signal gain, six 3 mm x 10 mm x 30 mm BGO crystals were wrapped individually with Teflon reflecting tape and coupled to six locations on the PMT faces. Crystals were positioned near each of the PS-PMT corners, 2 cm from the nearest vertical edge of the window, and 1 cm from the nearest horizontal edge. The remaining two crystals were positioned near the centre of the window, 2 cm apart. A thin layer of optical grease was used as the coupling material. The crystal arrangement was irradiated using a ^{68}Ge rod source, placed 1.5 m from the PS-PMT face. 1×10^6 singles events were collected for each of 20 PS-PMT high voltage settings, ranging from 1180 V to 1280 V, in 5 V increments. Note that this variation greatly exceeds the magnitude of high voltage drift that would be seen during normal operation of the scanner. However, it was of interest to span this large range of settings in order to examine the effect on detected positions of events.

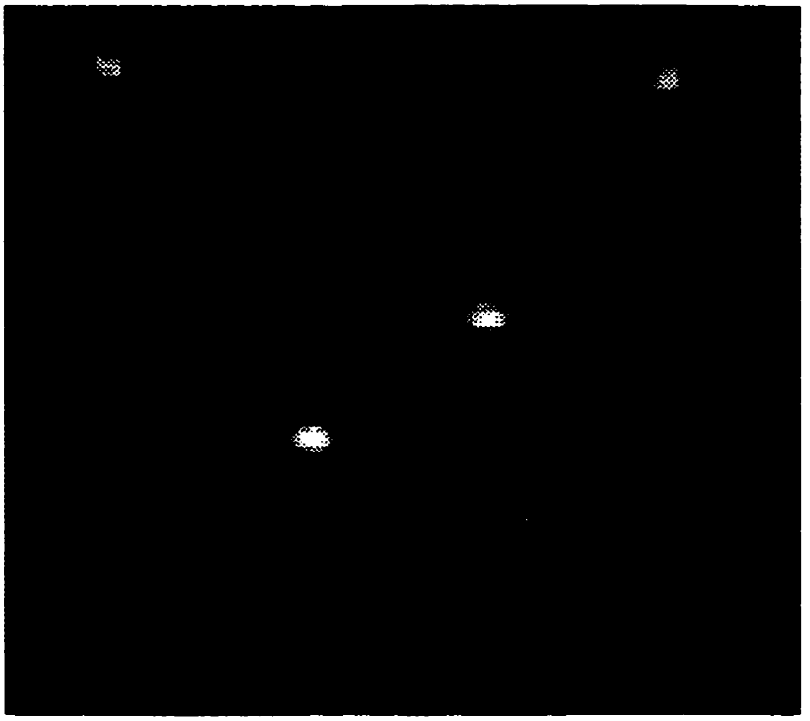

Figure 5.6. The image of six 3 mm x 10 mm x 30 mm crystals coupled to the PS-PMT.

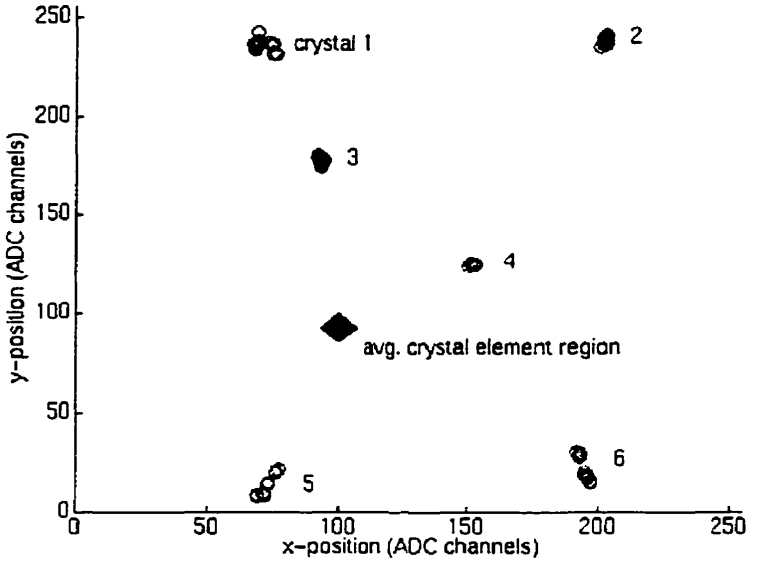

Figure 5.7. The shift in crystal locations resulting from the variation of the PS-PMT high voltage supply between 1180 V and 1280 V.

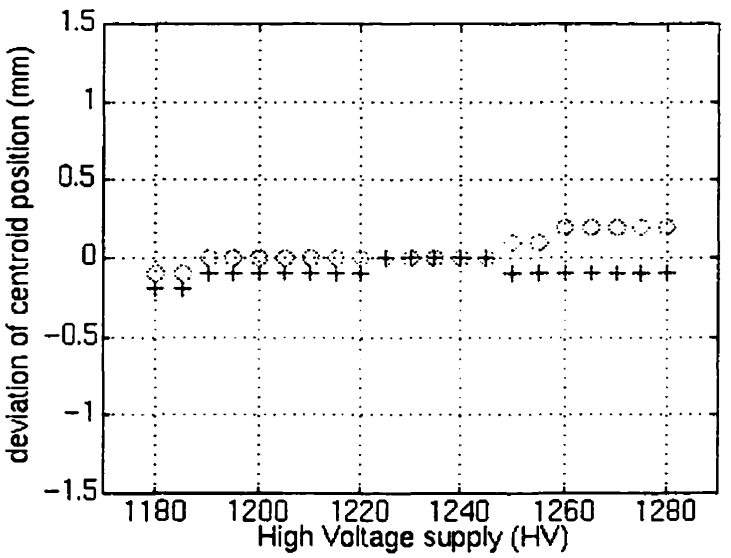

Figure 5.8. The spatial shift of the centroid of counts from one of the central crystals (crystal 3) (+) indicate the shift in the x-dimension and (o) indicate the shift in the y-dimension.

Figure 5.6 shows the image of the six crystals (for this image the operating voltage of 1240 V was used). In each of twenty images similar to this one, the centroids of the six crystals

were computed. As seen in Figure 5.7 in which the centroid locations are plotted, the variation of the HV over 100V causes detected locations of the crystal elements to shift slightly. This shift is most pronounced for the crystals near the corners of the PS-PMT. For comparison, an average-sized crystal element region is also illustrated in this plot.

Figure 5.8 and Figure 5.9 illustrate the deviation, in millimetres, from the locations obtained when using the operating voltage of 1240V. Figure 5.8 shows the deviation of the crystal that was least affected (crystal 3), positioned near the centre of the PS-PMT window. The magnitude of the deviation did not exceed 0.2 mm. For the bottom-left crystal however (crystal 5), the magnitude of the shift resulting from an increase of 40V above the operating value is 0.85mm. This shift corresponds to 60% of the average distance between opposite corners of a crystal element region.

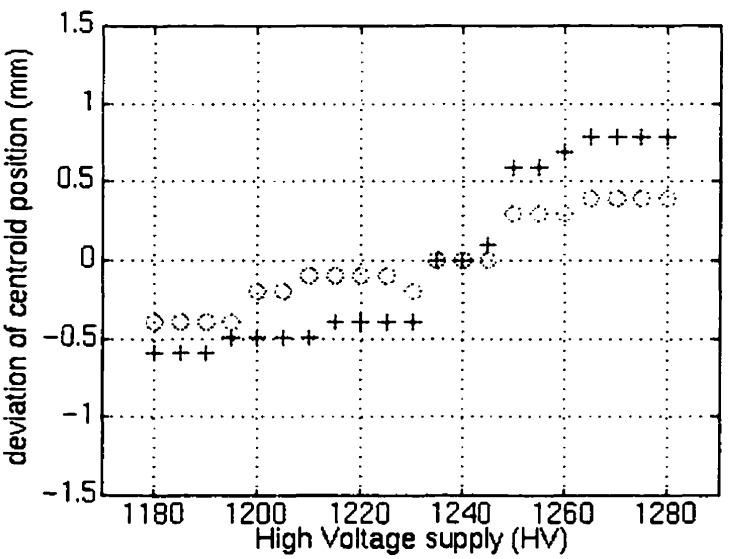

Figure 5.9. The spatial shift of the centroid of counts from one of the edge crystals (crystal 5) produced by the variation of PS-PMT high voltage. (+) indicate the shift in the x-dimension and (o) indicate the shift in the y-dimension.

While the range of 100V is only 8% of the nominal operating voltage, the corresponding variation of the location of the energy spectrum photopeak is significant. Figure 5.10 illustrates that varying the HV from 1180V to 1280V increases the location of the photopeak by a factor of 2.3. This may be compared to the fluctuations of photopeak location seen in

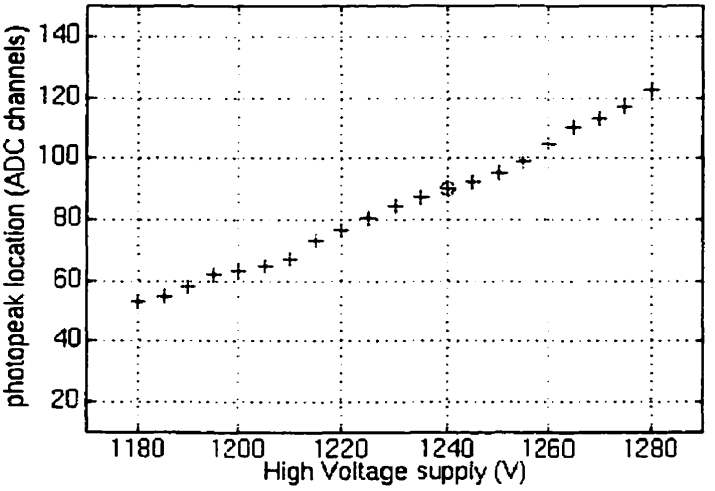

Figure 5.10. The variation of photopeak location with HV.

practice. After using the detectors for several minutes, the locations of the energy photopeaks have been found to be quite stable, varying over just a few channels. Furthermore, using a digital voltmeter, the fluctuations of the PS-PMT HV supply about the operating voltage were measured to be ±1V.

5.2. The Efficiency Look-Up-Tables

Two-dimensional representations of the efficiency tables for detectors A and B are shown in Figure 5.11 and Figure 5.12, respectively. Each shaded square represents an identified crystal element, and the intensity indicates the efficiency value, in the range [0, 255]. Odd rows and columns, starting from the top and left, correspond to proximal crystal elements. Even rows and columns indicate the efficiency values of the distal elements.

The effect of applying these efficiency values was assessed by generating coincident-event images while flood-irradiating the detectors using a 2μCi / ml source in a 80mm x 80mm x 40 mm container. $5x10^6$ events were collected in list-mode. Images were generated by backprojecting the same data with, and then without the application of the efficiency values. Figure 5.13 shows the improvement in uniformity achieved by using the efficiency LUT. Both images result from the same number of events, and both are shown with the same window width and level settings.

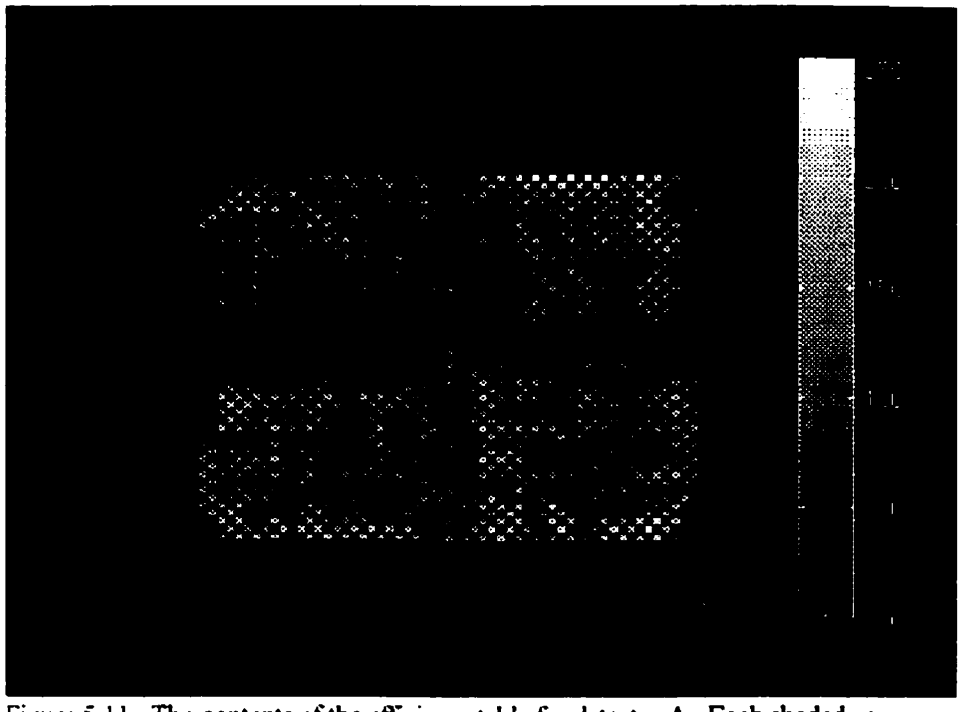

Figure 5.11. The contents of the efficiency table for detector A. Each shaded square represents an identified element, and the intensity indicates the crystal efficiency which is assigned a value between 0 (for missing or unidentified elements) and 255.

The image was generated from the list file data, while continually recalculating a measure of uniformity defined by the National Electrical Manufacturers Association (NEMA)[103]:

$$U(\%) = \frac{P_{max} - P_{min}}{P_{max} + P_{min}} \times 100\% \qquad (5.1)$$

where P_{max} and P_{min} are the maximum and minimum pixel values in the image.

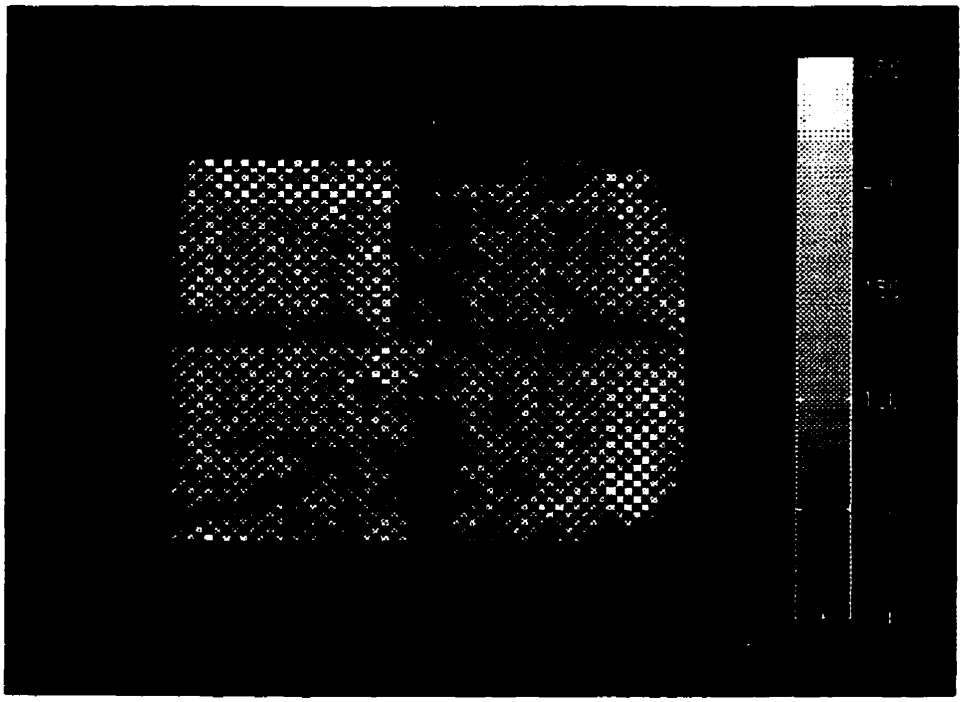

Figure 5.12. The efficiency LUT for detector B.

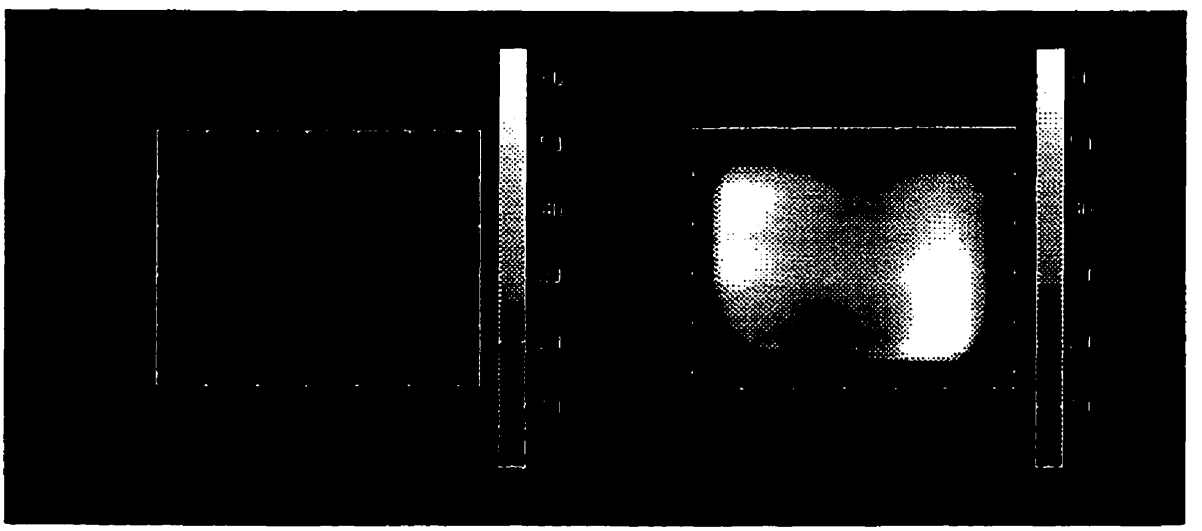

Figure 5.13. The image on the right shows the coincident image of a 2 μCi / ml flood 80 mm x 80 mm x 40 mm FDG phantom, before making corrections using the efficiency LUT. On the left is the image formed when the same list file is replayed with application of efficiency corrections. Both images result from the same number of coincident events and are shown here with the same colour window width and level.

This value stabilized following approximately $2x10^6$ events, indicating that the remaining nonuniformities were systematic and not simply caused by limited statistics. Figure 5.14 shows the x-profiles through the middle of the flood-irradiation images of Figure 5.13. Similar profiles, in the y-direction, are given in Figure 5.15. Without applying the efficiency corrections, the uniformity was very poor. Using the definition 5.1, the uniformity was found

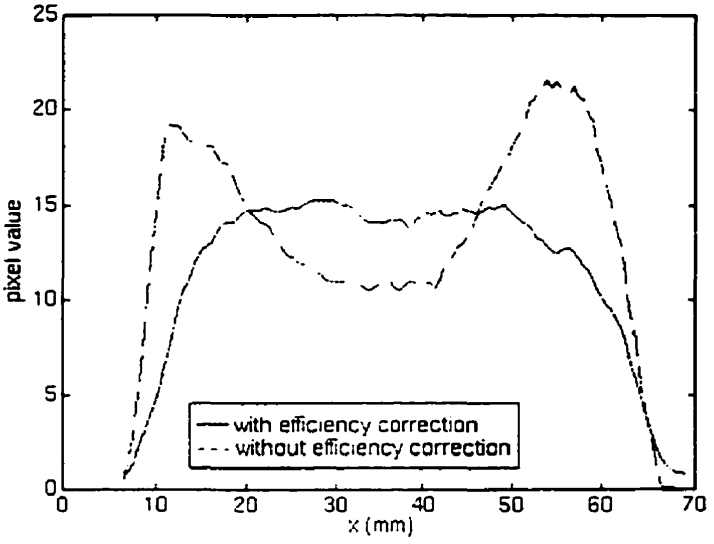

Figure 5.14. Horizontal (x) profiles through the coincident flood image in Figure 5.13 with (solid line) and without (dashed line) the application of efficiency corrections.

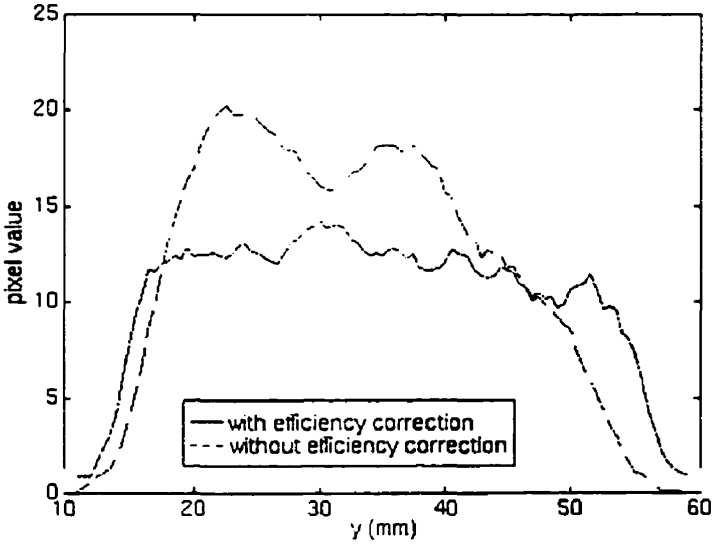

Figure 5.15. Vertical (y) profiles through the coincident flood image.

to be 33% over the central 50 mm of the x-profile, and 60% over the central 40 mm of the y-profile. Applying the corrections in the efficiency LUTs reduced these values to 6% and 15%, respectively.

5.3. The Energy Look-Up-Tables

The contents of the energy LUTs are represented in Figure 5.16 and Figure 5.18 for detectors A and B, respectively. As for the efficiency LUT, each identified crystal element is represented by a shaded square. The intensity of each square in this case indicates the ADC channel in the energy spectrum at which the photopeak was located.

Regions corresponding to each of the four blocks coupled to the PS-PMT can be discerned in these figures, but there is also a clear variation of gain within each of the blocks. The values in these LUTs reflect both the variation of light output between crystal elements and the spatial variation of the photocathode quantum efficiency. Figure 5.17 shows specifications for PS-PMT A provided by the manufacturer which describe the uniformity of quantum efficiency of the photocathode. This data was generated by coupling a blue-filtered tungsten light source to a 1.0 mm-diameter plastic optical fibre, and scanning the fibre to 21x19 locations over the central 55 mm x 55 mm of the PS-PMT window. For the PS-PMTs we have purchased to date, the nonuniformities measured in this manner range from 13% to 44%. This data thus isolates the effects of PS-PMT on the spatial variation of gain, and does not include any gain variations caused by crystal block. Comparison of Figure 5.16 to Figure 5.17 reveals similarities, confirming that a significant proportion of the spatial variation of gain recorded in the energy LUT is indeed caused by photocathode nonuniformity.

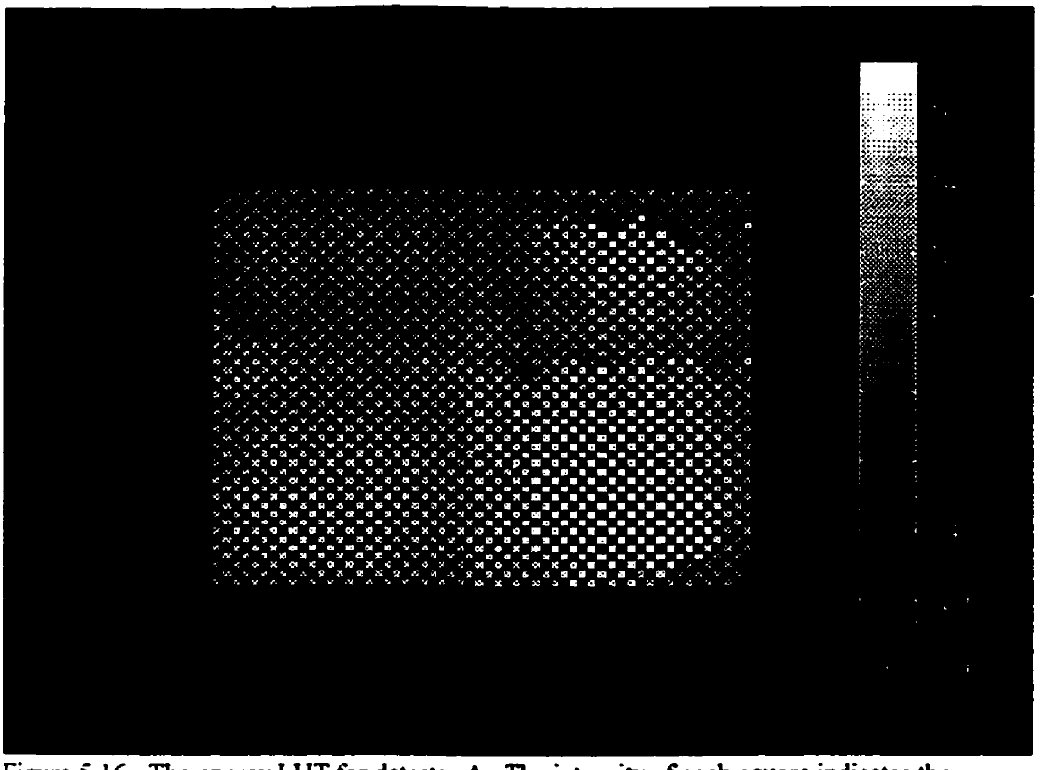

Figure 5.16. The energy LUT for detector A. The intensity of each square indicates the location of the energy spectrum photopeak for individual elements.

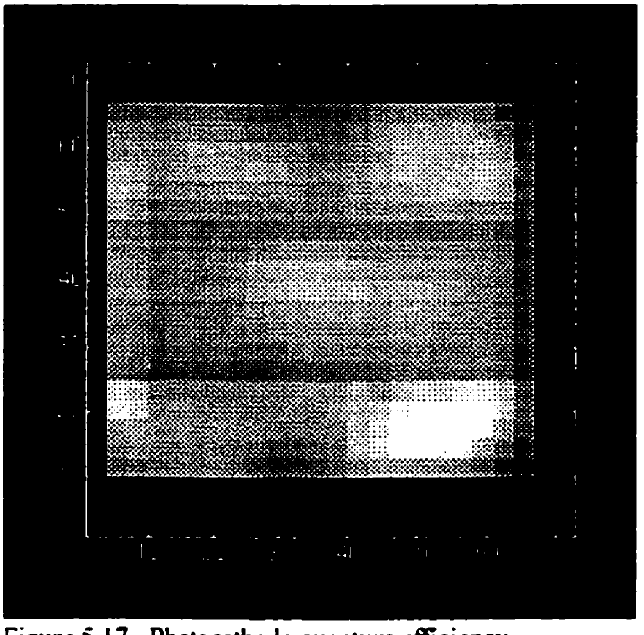

Figure 5.17. Photocathode quantum efficiency nonuniformities for PS-PMT A. This data was obtained by illuminating the central 55 mm x 55 mm of the photocathode at regular intervals using an optical fibre and a tungsten light source.

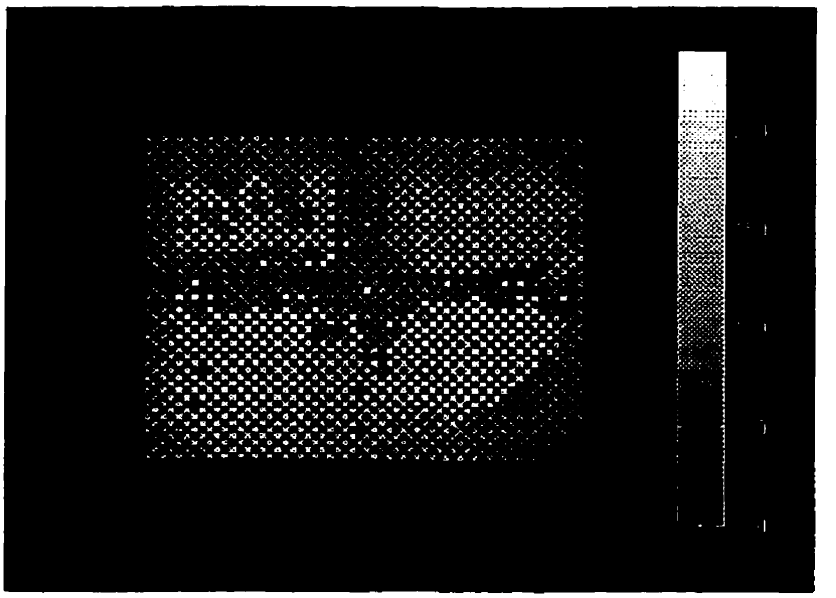

Figure 5.18. The crystal energy LUT for detector B.

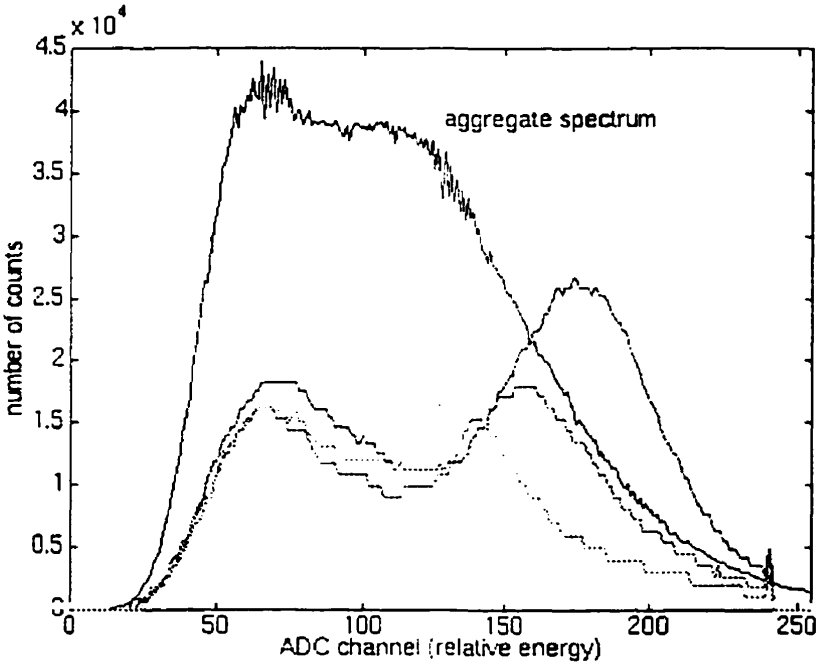

Figure 5.19. The aggregate singles energy spectrum for four detector blocks, and the spectra for three identified crystal elements (element spectra have been scaled for plotting on the aggregate spectrum scale)

The main advantage of using the energy LUT is illustrated in Figure 5.19. This figure compares the aggregate energy spectrum produced by flood-irradiating the four detector blocks with the spectra obtained for individual identified crystal elements. The single-element spectra have been scaled in order to display them on the same scale as the aggregate. Unlike the aggregate spectra given in Chapter 3 for a *single* potted block coupled to the PS-PMT window, no photopeak is seen in the spectrum produced by four blocks. This poor aggregate spectrum results from the superposition of spectra from a large number of crystal elements, each exhibiting different gains. As shown, when only the counts falling inside one crystal element region are considered, the photopeak can be distinguished clearly. The best, typical and worst element spectra of detector A are shown here, with energy resolutions of 30%, 34% and 38%, respectively

5.4. Discussion

The four crystal blocks coupled to a PS-PMT cover a 72 mm x 72 mm area, approximately corresponding to the dimensions of the borosilicate window. The anode wires, however, span only 63.6 mm in the x-direction and 55.5 mm in the y-direction. This loss of sensitive detector area arises from the fact that some space is required for the dynode supports near the inner surface of the PS-PMT housing. After developing the technique for crystal identification, it is now clear that achieving a 72 mm x 72 mm FOV is a very optimistic goal, but that it is possible to identify crystal elements over an area of 59 mm x 49 mm.

The dimensions of this identified region are consistent with those found by other researchers who have used similar PS-PMTs for imaging. Ordonez et al[104] have used a single 73 mm x 73 mm x 8 mm NaI(Tl) crystal coupled to a R2487-02 PS-PMT (which differs from the R3941 only in the number of dynodes) for the construction of a miniature gamma camera. Distortions around the periphery of this camera limited the UFOV to about fifty percent of the crystal area. A group at Hamamatsu Photonics has used the R3941 PS-PMT in

constructing high-resolution imaging systems, and has quantified[105] the "useful area" (using a small spot light source) to be 60 mm x 55 mm. However, when an array of 2 mm x 2 mm BGO pillars was used, the mismatch of refractive indices caused the light to spread through the optical coupling and the window, and the useful area was reduced further. An initial prototype constructed by this group employed a matrix of BGO elements covering the central 59.2 mm x 50.4 mm of the PS-PMT window. This area was subsequently reduced for second and third prototypes to 50.4 mm x 48.2 mm.

We have extended the crystal area to 72 mm x 72 mm in anticipation of increasing the UFOV by using a targeted sparse readout technique currently in development by Clancy[106] et al. This approach involves determining a binary address corresponding to the anode wire receiving the greatest signal using a winner-take-all circuit, and then digitizing the signal from each of the six wires closest to the centroid of the charge. In addition to increasing the signal-to-noise ratio, this method facilitates the determination of the distribution of the charge across the wires of the anode. Distributions truncated at the edge of the anode may be extrapolated in order to estimate the true centroid.

Figure 5.1 and Figure 5.2 illustrate the very irregular spatial distortion throughout the identified region of the detector. These images emphasize the necessity of correcting for spatial distortion by using crystal identification as opposed to applying an analyical function to the acquired position data, for example. The nature of these distortions have been observed to depend on the PS-PMT used, so that it would be impossible to apply a common position remapping to all detectors. Without using the crystal identification, it would be impossible to perform energy discrimination, as suggested by the absence of photopeak in the aggregate spectrum of Figure 5.19. This unsatisfactory overall energy resolution confirms the findings of Yasillo et al[107], who have reported that the pulse-height resolution was relatively good for local areas of their R2487-02 PS-PMT / NaI(Tl) crystal detector, but became quite poor when the total crystal face was irradiated. This characteristic likely results from the spatial variation of PS-PMT photocathode quantum efficiency. For the PEM

system, by segmenting the total positioning-channel space into crystal element regions, it is possible to recover the photopeak in the spectrum, achieve a reasonable energy resolution, and perform energy discrimination as the data is acquired.

Before employing the semi-automated technique for crystal identification described in Chapter 4, several fully-automated approaches were investigated. In particular, methods involving neighbourhood-thresholding, locating local-maxima and template-matching were all tested and achieved limited degrees of success. These techniques were often ineffective when presented with low peak-to-valley ratios, noise, or artefacts (such as the ADC differential nonlinearity) in the image. Although a number of crystal elements could be isolated using these methods, a considerable amount of retrospective checking for incorrectly located or omitted crystal elements was required. The identification of 59 x 49 crystal element regions was achieved only after employing the method requiring the initial placement of a few points along each row and column. Although this step requires about ten minutes for each detector, no further adjustments of the crystal identification are required.

To summarize, we have found that the spatial distortion, the crystal spatial variation of efficiency and the spatial variation of the energy signal are the three main characteristics of the PEM detectors requiring correction before acquired data is used for image formation. Because these are largely characteristics of the PS-PMT, it is likely that any high-resolution PET detector using a similar device would necessitate these corrections. The application of the LUTs described above results in a significant improvement in the image quality. In order to clearly visualize this improvement, a phantom of regularly-spaced capillary tubes was constructed as illustrated in Figure 5.20. In order to achieve a reasonable count rate from the very small volume of radioisotope in the tubes, a solution of ^{18}F in water (a byproduct of FDG production at the Montreal Neurological Institute cyclotron) with a high activity concentration (2.5 mCi/ml) was used. The phantom was placed at the centre of the FOV of the PEM scanner, with a detector separation (between the distal crystal faces) of 65 mm.

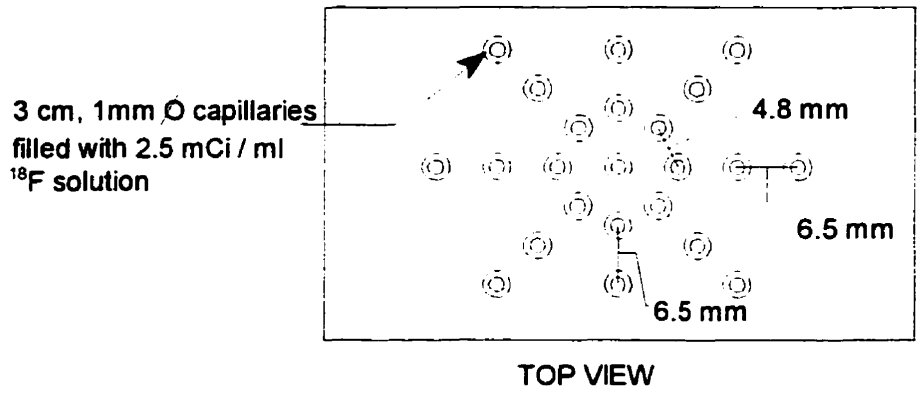

Figure 5.20. Top view of the capillary-tube phantom.

With this arrangement, data was acquired for 30 minutes. Figure 5.22 shows the image resulting from replaying the list file *without* applying distortion, efficiency or energy corrections (if the distortion correction is not made, the remaining two LUTs cannot be accessed, since the crystal coordinates are required as indices). While seven images are produced in the backprojection, this was the best-focused. The window width and level were adjusted in order to make all of the tubes visible, but due to the nonuniform efficiency, the majority of the colour scale is occupied by the images of the most peripheral tubes. The higher pixel values at the edges likely results from the charge-truncation whereby events occurring over a region of the periphery are detected as occurring at the same location. While individual distributions for each of the tubes are distinguished, the spatial distortion is evident in this image, affecting both the shape and the relative locations of the images of capillary tubes. For comparison, Figure 5.21 illustrates the image resulting from the same list file when all three LUTs are used. An energy window of 300 to 700 keV was imposed on the data for both images. Note that it was somewhat difficult to fill the capillary tubes to the same level with the FDG solution, and therefore the relative quantity of the isotope may vary between tubes by approximately ±25%. Thus, while this comparison clearly illustrates the

improvement obtained by employing distortion LUTs, a quantitative measurement of the effect of the efficiency table was more acurrately determined by using a flood source as described previously.

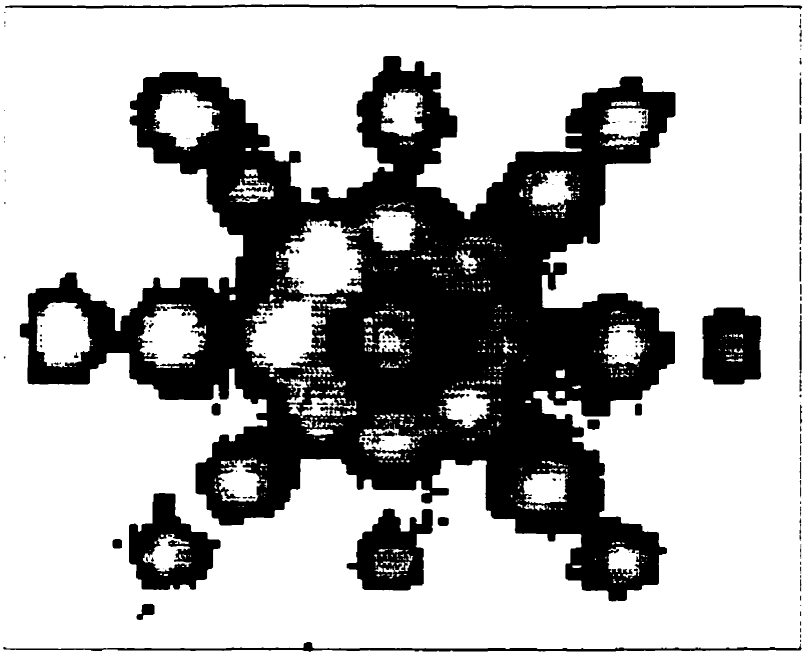

Figure 5.21. The image resulting from replaying the same list file after applying distortion, efficiency and energy corrections. An energy window of 300 keV to 700 keV was used.

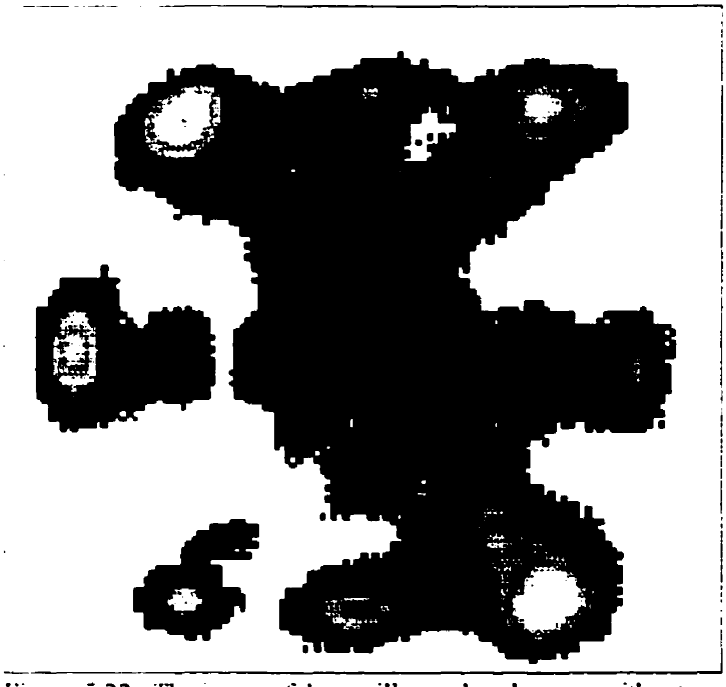

Figure 5.22. The image of the capillary-tube phantom without distortion, efficiency or energy corrections.

6. Conclusions

This thesis has described the initial stages in the development of system for the high-resolution metabolic imaging of breast cancer. Both the construction of the detectors and the development of the required calibration techniques are steps that necessarily preceded the commencement of phantom studies and clinical investigations. Because the amount of accessible literature describing the details of high-resolution PET detector block manufacture and calibration is somewhat limited, the methods described here result from a very educational period of experimentation. Since the completing of the work described here, the PEM system has been used continuously for breast phantom studies conducted by Alanah Bergman (these and other facets of the project will be discussed in her thesis which will be published in the near future.) A 5mm-diameter glass bulb filled with FDG placed inside a plastic container was used to simulate a breast tumour, and was clearly visible when a 6:1 tumour : background ratio was used (this is less contrast than would be expected clinically, as discussed in Chapter 2). With these promising results, we are very much anticipating clinical trials within the coming few weeks at the Cedar Breast Clinic of the Royal Victoria Hospital in Montreal.

The detector block used in the PEM system is novel in terms of its high packing fraction of very small crystal elements on two layers. While other investigators (mentioned in Chapters 3 and 5) have used various crystal/PS-PMT combinations, they have employed either uncut or discrete crystals. While the former offers ease of construction, the spatial resolution is limited by light-spread in the unsegmented crystal. While the latter offers both ease of construction and reduced cross-talk between elements, it is limited in terms of the associated cost. For these reasons, we have invested a considerable amount of time in developing a modular block, cut from a solid piece of BGO, and will continue to use this approach in the future. Although the "learning curve" encountered while producing of PEM detector blocks was considerable, this initial phase has now been completed. It is the hope of the author that this thesis may serve as a guide in the construction of detectors for future scanners.

After solving several technical problems, the method for machining detector blocks was reproducible and resulted in a high yield. Using the set-up described in Chapter 3, the blocks required for a complete system can be machined during eight days. With the use of six blades and the possibility of cutting more than one block in a single pass, this duration will be reduced in the future. Several hours are required to etch all eight blocks. Approximately two weeks are required for the potting of the blocks (to allow the epoxy to cure for each), but this duration may be shortened also, with the provision of several additional potting moulds. This reasonably short time scale is particularly important in that it ensures that the device will remain widely affordable and accessible.

In cutting the detector blocks, there was a limited amount of control achieved over the surface finish of the crystal elements produced. The effect of the roughened crystal surface was reflected by the decrease of light output (the photopeak location is decreased from ADC channel 109 to channel 37). The acid etching technique used in the future will not be modified, since it recovers almost all of this lost light output. While the mechanical strength added to the block by the epoxy-based potting compound used was crucial, we look forward to examining other possible materials which may be more effective as reflective coatings. As expected, however, the spatial resolution of the block improved progressively from one stage of manufacture to the next.

It should be noted that the PEM detector block is not specific to the Hamamatsu R3941 PS-PMT. As PS-PMT technology improves, particularly in terms of the resolving capability and the detector cross-talk, the PEM block, or similarly-constructed blocks of different dimensions can be coupled to other devices.

Because a description of the specific calibrations required when using a crystal/PS-PMT detector has not been published, the LUTs implemented in the PEM system were based on those used for conventional PET detectors. In light of the results given in Chapter 5, it is clear that all of the LUTs implemented are indeed required in order to generate useful images.

Spatial distortion, variation of detector gain and efficiency nonuniformity all have different and pronounced effects on image quality.

Use of the distortion LUTs, which contain the crystal identification results, clearly reduce the effects of the harsh nonlinearities inherent in the PS-PMTs. Although a capillary-tube phantom was used to emphasize this point, we observed similar improvements in the image quality of our breast tumour phantoms. The FOV of the scanner is determined by the number crystal elements that are distinguished during crystal identification. The most predictable criticism of the scanner is the current size of this FOV (59mm x 49mm). In light of information provided by the PS-PMT manufacturer and by previous investigators (discussed in Chapter 5), it seems that this may be the largest FOV that will be achieved while using a resistor-chain readout. Although it is sufficient to begin clinical trials, we anticipate that the FOV will increase within the next few months with the implementation of a sparse targeted readout currently under development by Ray Clancy. The crystal identification techniques will remain unchanged after making this modification.

The spatial variation of detector gain is an effect which results from properties of both the crystal block and the PS-PMT photocathode. With this in mind, it may be possible to match the "best" crystal block (in terms of light output) to the "worst" area of the photocathode (in terms of quantum efficiency). Crystal identification facilitates energy discrimination on an element-by-element basis. As expected, there is a great improvement in the energy resolution between the aggregate spectrum (in which a single photopeak is not apparent) and a single-element spectrum (which has a energy resolution of ~35%). This is also a marked improvement over the energy resolution of a *single* potted block positioned at the centre of the PS-PMT (which has an energy resolution of, on average, 53%).

The range of efficiencies of separate crystal elements was larger than would be predicted simply by slight discrepancies between element dimensions. Three factors likely account for this: i) the presence of event pile-up at the periphery of the identification; ii) crystal defects

(such as several missing elements); and iii) imperfections in the optical coupling between the block and the PS-PMT window. Regardless of the origin of the efficiency variations, they are clearly required, as indicated by the improved uniformity of the flood-source images in Chapter 5.

The possibility of producing additional detectors has been mentioned at several points in this thesis. We have recently received generous funding from the Medical Research Council of Canada for the construction a small-animal PET scanner[108], which will provide high-resolution scanning of rodents and primates. The detector design will be identical to that described in this thesis, with the possibility of replacing the BGO with LSO crystal because of the increased light output of the latter. The detectors will be mounted facing each other on a rotating gantry so that angular views may be acquired, with a rotation speed reaching 60°/s. Data acquired in this "rotational mode" will be reconstructed to form 3D images, with an anticipated spatial resolution of 2.5mm x 2.5mm. The scanner will also support a "longitudinal mode" in which the detectors will scan along the length of the animal. We are very much looking forward to applying the experience and results described in this thesis to this new project.

7. References

1. G. L. Brownell, W. H. Sweet, "Localization of brain tumours with positron emitters", Nucleonics, 1953, vol. 11, no. 40.

2. F. Enge, Introduction to nuclear physics, ©1966, Addison-Wesley Publishers, Reading, Mass., p. 304.

3. R. E. Lapp, H. L. Andrews, Nuclear Radiation Physics, Fourth Edition, ©1979, Prentice-Hall, Englewood Cliffs, NJ, chapter 8.

4. J. A. Sorensen, M. E. Phelps, Physics in Nuclear Medicine, Second Edition, ©1987, W. B. Saunders Company, Philadelphia, p. 31.

5. S. E. Derenzo, "Recent developments in positron emission tomography instrumentation", 1986, SPIE, vol. 671, pp 232-243.

6. M. Deutch, "Annihilation of positrons", Progress in Nuclear Physics, 1953, vol. 3, pp 131-158.

7. S. de Benedetti, C. E. Cowan, W. R. Konneker et al., "On the angular distribution of two-photon annihilation radiation", 1950, Phys. Rev., vol. 77, pp 205-212.

8. H. E. Johns, J. R. Cunningham, The Physics of Radiology, ©1983, Charles C. Thomas, Publisher, Springfield, Illinois., chapter 5.

9. H. E. Johns, J. R. Cunningham, The Physics of Radiology, ©1983, Charles C. Thomas, Publisher, Springfield, Illinois., Table 5-5, p 163.

10. B. Ahluwalia, "Positron emission imaging", in Nuclear Medical Physics, Volume III, ©1987, CRC Press, Boca Raton, Florida, Chapter 2, pp 49-59.

11. S. E. Dorenzo, "Precision measurement of the annihilation point spread distributions for medically important positron emitters", 1979, Proceedings of the 5th International Conference on Positron Annihilation, pp 819-823.

12. J. A. Sorensen, M. E. Phelps, Physics in Nuclear Medicine, Second Edition, ©1987, W. B. Saunders Company, Philadelphia.

13. H. Iida, I. Kanno, S. Miura, M. Mrakami, K. Takahashi, K. Uemura, "A simulation study of a method to reduce positron annihilation spread distributions using a strong magnetic field in positron emission tomography", 1986, IEEE Trans. Nucl. Sci., vol. 33, no. 1, pp 597-600.

14. W. W. Moses, S. E. Derenzo, "Empirical observation of resolution degradation in positron emission tomographs utilizing block detectors", 1993, J. Nucl. Med., vol. 33, no. 5, p 101 (abstract)

15. Burle Industries, Photomultiplier Handbook, ©1980, Published by Burle Technologies, Inc., p 94.

16. R. E. Simon and B.F. Williams, "Secondary electron emission", 1968, IEEE Trans. Nucl. Sci., vol. NS-15, pp. 166-170.

17. H. Kume, S. Suzuki, J. Takeuchi, et al., "Newly developed photomultiplier tubes with position sensitive capability", 1985, IEEE Trans. Nucl. Sci., vol. 32, pp. 448-452.

18. H. Uchida, T. Yamashita, M. Iida et al., "Design of a mosaic BGO detector system for positron CT", 1986, IEEE Trans. Nucl. Sci., vol. 33, pp 464-467.

19. L. P. Adler, J. P. Crowe, N. K. Al-Kaisi, J. L. Sunshine, "Evaluation of breast masses and axillary lymph nodes with F-18 2-deoxy-fluoro-D-glucose PET", 1993, Radiology, vol. 187, pp 743-750.

20. J. R. Harris, S. Hellman, G. P. Canellos, B. Fisher, "Cancer of the breast", in: V. T. DeVita Jr, S. Hellman, S. A. Rosenberg, eds., Cancer: principles and practice of oncology, 2nd Edition, ©1985, Lippencott, Philadelphia.

21. D. D. Adler, R. L. Wahl, "New methods for imaging the breast: techniques, findings and potential", 1995, American Journal of Radiology, vol. 164, pp 19-30.

22. C. J. Thompson, K. Murthy, I. N. Weinberg, F. Mako, "Feasibility study for positron emssion mammography", 1994, Med. Phys., vol. 21, no. 4, pp 529-538.

23. C. J. Thompson, K. Murthy, Y. Picard, I. N. Weinberg, R. Mako, "Positron Emission Mammography (PEM): A Promising Technique for Detecting Breast Cancer", 1995, IEEE Trans. Nucl. Sci., vol. 42, no. 4, pp 1012-1017.

24. C. J. Thompson, K. Murthy, R. L. Clancy, J. L. Robar, A. Bergman, R. Lisbona, A. Loutfi, J. H. Gagnon, I. N. Weinberg, R. Mako, "Imaging Performance of PEM-I: A High Resolution System for Positron Emission Mammography", 1995 IEEE Nuclear Science Symposium and Medical Imaging Conference Record, vol. 2, pp 1074-1078.

25. D.E. Henson, L.A. Ries, "Progress in early breast cancer detection", 1990, Cancer, vol. 65, pp 2155-2158.

26. N. Lang, N. Talbert, K. Shewmake, "The current evaluation of non-palpable breast lesions", 1987, Arch Surg, vol. 122, pp 1389-1391.

27. M. Skinner, M. Swain, R. Simmons, "Non-palpable breast lesions at biopsy: a detailed analysis of radiographic features", 1988, Ann Surg, vol. 208, pp 203-208.

28. D. Franceschi, J. Crowe, R: Zollinger et al., "Breast biopsy for calcifications in non-palpable breast lesions", 1990, Arch Surg, vol. 125, pp 170-173.

29. J. Gisvold, "Imaging of the breast: techniques and results", 1990, Mayo. Clin. Proc., vol. 65, pp 56-66.

30. O. E. Niewig, E. E. Kim, W.H. Wong, W. F. Broussard, S. E. Singletary, G. N. Hortobagyi, R. S. Tilbury, "Positron Emission Tomography with fluorine-18-deoxyglucose in the detection and staging of breast cancer", 1993, Cancer, vol. 71, pp 3920-3925.

31. R. S. Brown, R. L. Wahl, "Over-expression of GLUT-1 glucose transporter in human breast cancer: an immunohistochemical study", 1993, Cancer, vol. 72, pp 2979-2985.

32. R. L. Wahl, R. L. Cody, G. D. Hutchins, E. E. Mudgett, "Primary and metastatic breast carcinoma: initial clinical evaluation with PET with the radiolabeled glucose analogue 2-[F-18]-fluoro-2-deoxy-glucose", 1991, Radiology, vol. 179, pp 765-770.

33. R. L. Wahl, K. R. Zasadny, G. D. Hutchins, M. Helvie, R. Cody, "Metabolic monitoring of breast cancer chemohormonotherapy using positron emission tomography (PET): initial evaluation", 1993, J. Clin. Oncol., vol. 11, pp 2101-2111.

34. C. J. Thompson, K. Murthy, Y. Picard, I. N. Weinberg, R. Mako, "Positron Emission Mammography (PEM): A promising technique for detecting breast cancer", 1995, IEEE Trans. Nucl. Sci. vol 42 no. 4, pp 1012-1017.

35. T. S. Curry, J. E. Dowdey, R. C. Murry, Christensen's Physics of Diagnostic Radiology: 4th Edition, ©1990, Lea and Febiger, Philadelphia, USA, p 236.

36. Hal Anger, "Scintillation camera", 1958, Rev. Sci. Inst, vol., no. 1, pp 27-33.

37. R. Clancy, C. J. Thompson, J. L. Robar, A. M. Bergman, "A simple technique to increase the linearity and field-of-view in position-sensitive photomultiplier tubes", accepted to the 1996 IEEE Conference Record of The Nuclear Science Symposium and Medical Imaging Conference.

38. T. Yamashita, personal communication, July 16, 1996.

39. W. W. Moses, S. E. Derenzo, C. L. Melcher, R. A. Manente, "A room temperature LSO / PIN photodiode PET detector module that measures depth of interaction", 1995, IEEE Trans. Nucl. Sci., vol. 41, no. 4, pp 1085-1089.

40. W. W. Moses and S. E. Derenzo, "Design studies for a PET detector module using a PIN photodiode to measure depth of interaction", 1994, IEEE Trans. Nucl. Sci., vol. NS-41, pp. 1441-1445.

41. W. W. Moses, S. E. Derenzo, R. Nutt, et al., "Performance of a PET detector module utilizing an array of silicon photodiodes to identify the crystal of interaction", 1993, IEEE Trans. Nucl. Sci., vol. NS-40, pp 1036-1040.

42. R. Lecomte, D. Schmitt, A.W. Lightstone, R.J. McIntyre, "Performance characteristics of BGO-silicon Avalance Photodiode Detectors for PET", 1995, IEEE Trans. Nucl. Sci., vol. NS-32, pp 529-532.

43. W. Worstell, O. Johnson, V. Zawarzin, "Development of a high-resolution PET detector using LSO and wavelength-shifting fibers", in the 1995 IEEE Nuclear Science Symposium and Medical Imaging Conference Record, vol. 3, 1756-1760.

44. Kavita Murthy, A study of the effects of detector width and depth on spatial resolution in Positron Emission Tomography, M.Sc. Thesis, McGill University, Montreal, ©1993, p. 15.

45. "Designing a stratified detection system for PET cameras", 1986, IEEE Trans. Nucl. Sci., vol. 33, no.1, pp 591-596.

46. M. Casey, M. Andreaco, R. Nutt, Investigation Of LSO Crystals For High Spatial Resolution Positron Emission Tomography, in the program of the 1996 IEEE Medical Imaging Conference, Anaheim, CA.

47. J. S. Karp, M. E. Daube-Witherspoon, "Depth of interaction determination in Na(Tl) and BGO scintillation crystals using a temperature gradient", 1987, Nucl. Inst. Meth. Phys. Res., A260, pp 509-517.

48. S. E. Derenzo, W. W. Moses, H. G. Jackson et al., "Initial characterization of a position-sensitive photodiode/BGO detector for PET", IEEE Trans. Nucl. Sci., vol. NS-36, pp. 1084-1089.

49. C. J. Thompson, "Scintillation crystals for Positron Emission Tomography having a non-reflective band", Canadian Patent #1303256, issued June 9, 1992.

50. C. J. Thompson, "Means for measuring the depth of interaction of gamma rays in scintillation crystals in order to improve the spatial resolution of positron imaging systems", US Patent #5122667, issued on June 16, 1992.

51. P. Bartzakos, C. J. Thompson, "A PET detector with depth of interaction determination", 1991, Phys. Med. Biol., vol. 36, no. 6, pp 735-748.

52. P. Bartzakos, C. J. Thompson, "A depth encoded PET detector", 1991, IEEE Trans. Nucl. Sci., vol. 38, no. 2, pp 732-738.

53. C. J. Thompson, K. Murthy, R. L. Clancy, J. L. Robar, A. Bergman, R. Lisbona, A. Loutfi, J. H. Gagnon, I. N. Weinberg, R. Mako, "Imaging performance of PEM-I: a high-resolution system for positron emission mammography", in the 1995 IEEE Nuclear Science Symposium and Medical Imaging Conference Record, vol. 2, pp 1074-1075.

54. Y. Shao, S. R. Cherry, S. Siegel, R. Silverman, "Evaluation of Multi-Channel PMTs for Readout of Scintillator Arrays", 1995 IEEE Nuclear Science and Medical Imaging Conference Record, San Francisco, CA .

55. Simon R. Cherry, Martin P. Tornai, Craig S. Levin Stefan Siegel, Edward J. Hoffman, "A Comparison of PET Detector Modules Employing Rectangular and Round Photomultiplier Tubes", 1995, IEEE Trans Nucl Sci, vol. 42, no. 4, pp 1064-1068.

56. Joel G. Rogers, "Testing 144- and 256-Crystal BGO Block Detectors", 1994, IEEE Trans Nucl Sci, vol. 41, no. 4, pp 1423-1428.

57. M. P. Tornai, G. Germano, E. J. Hoffman, "Positioning and Energy Response of PET Block Detectors with Different Light Sharing Schemes", 1994, IEEE Trans Nucl Sci, vol. 41., no. 4, pp 1458-1463.

58. M. Watanabe, H. Uchida, H. Okada, K. Shimizu, N. Satoh, E. Yoshikawa, T. Ohmura, T. Yamashita, E. Tanaka, 1992, "A High Resolution PET for Animal Studies", IEEE Trans Med Imaging, vol. 11, no. 4, pp 577-580.

59. T. Yamashita, M. Watanabe, K. Shimizu, H. Uchida, "High Resolution Block Detectors for PET", 1990, IEEE Trans Nucl Sci, vol. 37, no. 2, pp 589-593.

60. T. Yamashita, H. Uchida, H. Okada, T. Kurono, T. Takemori, M. Watanabe, K. Shimizu, E. Yoshikawa, T. Ohmura, N. Satoh, E. Tanaka, 1990, "Development of a High Resolution PET", IEEE Trans Nucl Sci, vol. 38, no. 2, pp 594-599.

61. W.M. Digby, M. Dahlbom, E.J. Hoffman, "Detector, Shielding and Geometric Design Factors for a High-Resolution PET System", 1990, IEEE Trans Nucl Sci, vol. 37, no. 2, pp 664-670.

62. M. Dahlbom, E.J. Hoffman, "An Evaluation of a Two-Dimensional Array Detector for High Resolution PET", 1988, IEEE Trans Med Imaging, vol 7, no. 4, pp 264-272.

63. H.B. Min, J .B Ra, K. J. Jung, S. K. Hilal, Z. H. Cho, "Detector Identification in a 4x4 Crystal Array Coupled to Two Dual PMTs for High Resolution Positron Emission Tomography", 1987, IEEE Trans Nucl Sci, vol. 34, no. 1, pp 332-336.

64. L. Eriksson, C. Bohm, M. Kesselberg, S. Holte, M. Bergstrom, J. Litton, "Design Studies of two Possible Detector Blocks for High Resolution Positron Emission Tomography of the Brain", 1987, Trans Nucl Sci, vol 34, no. 4, pp 344-348.

65. H. Uchida, T. Yamashita, M. Iida, S. Muramatsu, "Design of a Mosaic BGO Detector System for Positron CT", 1986, IEEE Trans Nucl Sci, vol. 33, no. 1, pp 464-467.

66. M.E. Casey and R. Nutt, "A Multicrystal Two Dimensional BGO Detector System for Positron Emission Tomography", 1986, IEEE Trans Nucl Sci., vol 33, no. 1., pp 460-463.

67. Price quotation, Rexon Components, Inc., 1993.

68. Yani Picard, McGill University, personal communication, 1995.

69. Carrier, Christian. Memoire de maitrise: Etude de la collecte de lumière, Université de Sherbrooke, 1988, p 96.

70. Alanah Bergman, personal communication, June 1995.

71. Xiaoguang, Yao, "A study of light collection efficiency in scintillation detectors", 1984, Nucl. Inst. Meth. In Phys Res., vol. 228, pp 101-104.

72. M. Cocci and A. Rota, "Light collection on a photocathode from a cylindrical scintillator", 1967, Nucl. Inst. Meth., vol. 46, pp 136-140.

73. H. Ishibashi, S. Akiyama, M. Ishii, "Effect of surface roughness and crystal shape on performance of bismuth germanate scintillators", 1986, Japanese Journal of Applied Physics, vol. 25, pp 1435-1438.

74. C. M. Ankebrandt, E. M. Lent, "Increasing the light collection efficiency of scintillation counters", 1963, Rev. Sci. Instr. vol. 34, pp 647-651.

75. S. E. Derenzo, J. K. Riles, "Monte Carlo calculations of the optical coupling between bismuth germanate crystals and photomultiplier tubes", 1982, IEEE Trans. Nucl. Sci. NS-29, pp 191-195.

76. Frank Wilkinson, Alpha Spectra, Inc., CO, USA, personal communication, April 1996.

77. Dow Corning, Information about High Technology Materials: SYLGARD 186 Encapsulating resin, 1993.

78. H. Klein and H. Schölermann, "Improvement of the light collection in scintillation detectors", 1979, IEEE Trans. Nucl. Sci., vol. NS-26, no. 1, pp 373-377.

79. C. Carrier, R. Lecomte, "Trapping of fluorescent light in cylindrical scintillators", Nucl. Inst. Meth. A278, 1989, pp 622-624.

80. Dow Corning Sales Office, Midland MI., personal communication, June, 1996.

81. S. R. Cherry, Y. Shao, M. P. Tornai, S. Siegel, A. R. Ricci, M. E. Phelps, "Collection of scintillation light from small BGO scintillators", 1995, IEEE Trans.

Nucl. Sci., vol. 42, pp 1058-1063.

82. I.N. Weinberg, M. Dahlbom, A.R. Ricci, E.J. Hoffman, "Crystal Identification in Modular Detectors for High Resolution PET", 1986, SPIE Proc., vol. 671, pp. 420-424.

83.C. Bohm, S. Holte, M. Kesselberg, L. Eriksson, M. Bergstrom, J. Litton, "Detector Blocks for High Resolution Positron Emission Tomography", 1986, SPIE Proc., vol. 671, pp. 254-260.

84.M. E. Casey, R. Nutt, "A Multicrystal Two Dimensional BGO Detector System for Positron Emission Tomography", 1986, IEEE Trans Nucl Sci, vol. 33, no. 1, pp 460-463.

85.M. Dahlbom, E.J. Hoffman, "An Evaluation of a Two-Dimensional Array Detector for High Resolution PET", 1988, IEEE Trans. Med. Imaging, vol. 7, no. 4, pp 264-272.

86. J.G. Rogers, A.J. Taylor, M.F. Rahimi, R. Nutt, M. Andreaco, C.W. Williams, "An Improved Multicrystal 2-D BGO Detector for PET", IEEE Trans. Nucl. Sci, vol. 39, no. 4, 1992.

87.J. G. Rogers, "Testing 144- and 256-crystal BGO Block Detectors", IEEE Trans. Nucl. Sci, vol. 41, no. 4, 1994.

88.W.M. Digby, M. Dahlbom, E.J. Hoffman, "Detector, Shielding and Geometric Design Factors for a High-Resolution PET System", IEEE Trans. Nucl. Sci., vol. 37, no. 2, 1990.

89.Technical data for the R3921 Position-Sensitive Photomultiplier Tube, Hamamatsu Photonics, K.K.

90.P.D. Cutler, E.J. Hoffman, "Use of Digital Front-End Electronics for Optimization of a Modular PET Detector", 1994, IEEE Trans Med Imaging, vol. 13, no. 2, pp 408-418.

91.K. Murthy, C.J. Thompson , I.N. Weinberg, F.M. Mako, "Measurement of the Coincidence Response of Very Thin BGO Crystals", 1994, IEEE Trans Nucl Sci, vol. 41, no. 4, pp 1430-1435.

92.Paul M. Embree, Bruce Kimble, C Language Algorithms for Digital Signal Processing, ©1991, Prentice-Hall, Inc., pp 257-267.

93.Clay M. Thompson, Loren Shure, MATLAB Image Processing Toolbox, ©1995, The Mathworks, Inc., p 1-41.

94.Carl de Boor, Spline Toolbox, ©1995, The Mathworks, Inc., pp 1-10 - 1-13.

95. Sorenson, James. A. and Phelps, Michael E., Physics in Nuclear Medicine, 2nd Edition, ©1987, W. B. Saunders Company, pp 239-244.

96.A.W. Lightstone, R.J. McIntyre, R. Lecomte and D. Schmitt, "A Bismuth Germanate-Avalanche Photodiode Module Designed for Use in High Resolution Positron Emission Tomography", IEEE Trans Nucl. Sci., vol 33, no. 1 pp 456-459.

97.S.R. Cherry, Y. Shao, M. Tornai, S. Siegel, A.R. Ricci, M.E. Phelps, "Collection of Scintillation Light from Small BGO Crystals", 1995, IEEE Trans Nucl Sci, pp 1058-1063.

98.H. Uchida, T. Yamashita, M. Iida et al., "Design of a mosaic BGO detector for positron CT", 1986, IEEE Trans Nucl. Sci. vol. 33, pp 464-468.

99.H. Press, S. A. Teukolsky, W. T. Vetterling, B. P. Flannery, Numerical Recipes in C: The Art of Scientific Computing, Second Edition, © 1992, Cambridge University Press, p 650.

100. P. Horowitz, W. Hill, The Art of Electronics, ©1989, Cambridge University Press, p 615.

101. M. Dahlbom, E. Hoffman, "An evaluation of a two-dimensional array detector for high resolution PET", 1988, IEEE Trans. Med. Imaging, vol. 7, no. 4, pp 264-272.

102. C. Moisan, personal communication at the 1995 IEEE Medical Imaging Conference, San Francisco.

103. S. Webb, editor, The Physics of Medical Imaging, ©1988, Institute of Physics Publishing, p 246.

104. C.E. Ordonez, R. A. Mintzer, J. N. Aarsvold, N.J. Yasillo, K. L. Matthews, "Simulation of imaging with sodium iodide crystals and position-sensitive photomultipliers", 1994 IEEE Nuclear Science Symposium & Medical Imaging Conference Record, vol 2, pp 1358-1361.

105. T. Yamashita, personal communication, August 9, 1996.

106. R. L. Clancy, C. J. Thompson, J. L. Robar, K. Murthy, E. Beuville, W. W. Moses, "A targeted sparse readout for multi-anode photomultipliers and optically isolated crystals", 1995 IEEE Nuclear Science Symposium & Medical Imaging Conference, vol 1, pp 409 411.

107. N.J. Yasillo, R. N. Beck, M. Cooper, "Design considerations for a single-tube gamma camera", 1990, IEEE Trans. Nucl. Sci., vol. 37, pp 609-615.

108. C.J. Thompson, M. Diksic, P. Cumming, "Application to the Medical Research Council of Canada for the Construction and Initial Trials of a Small Animal PET Scanner at the Montreal Neurological Institute", February, 1996.

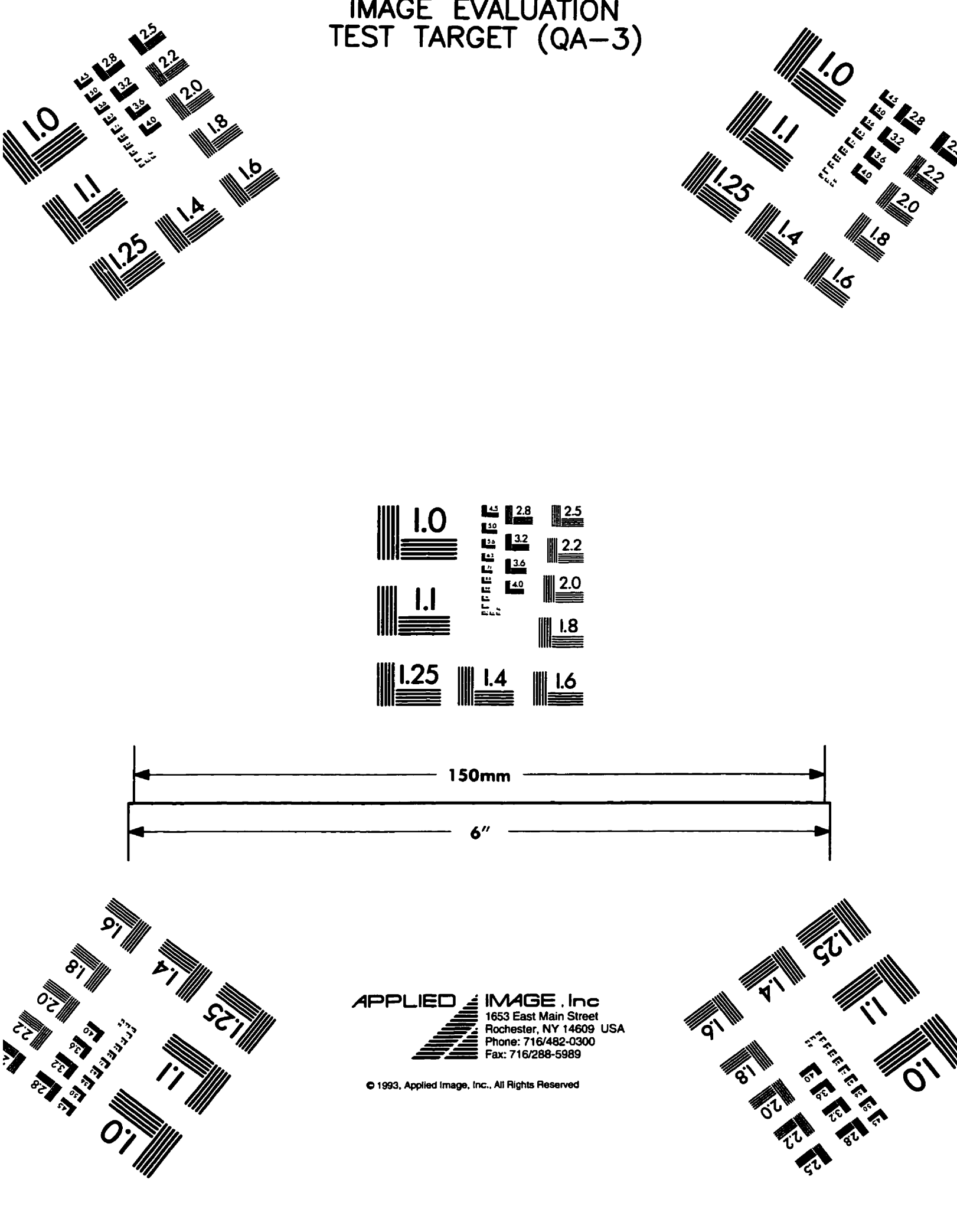
IMAGE EVALUATION
TEST TARGET (QA-3)
1.0
1.1
1.25
1.4
1.6
2.8
2.5
3.2
2.2
3.6
2.0
4.0
1.8
4.5
5.0
5.6
6.3
150mm
6"
APPLIED IMAGE, Inc
1653 East Main Street
Rochester, NY 14609 USA
Phone: 716/482-0300
Fax: 716/288-5989
© 1993, Applied Image, Inc., All Rights Reserved